Doctoral Dissertation
Doctoral Program in Aerospace Engineering (XXXI.th cycle)

MODEL BASED CORRELATION METHODS FOR FAULTS DETECTION AND IDENTIFICATION ALGORITHMS ON ELECTROMECHANICAL ACTUATORS USED IN PRIMARY FLIGHT CONTROL SYSTEMS

A new prognostic approach based on the spectral analysis in multi failures mode

Dario Belmonte
* * * * * *

Supervisors
Prof. Paolo Maggiore

Doctoral Examination Committee:
Prof. Francesco Tornabene, Referee, University of Salento
Prof. Constantin, Rotaru, University of Henri Coanda Air Force Academy
Prof. Prof. Elena Campagnoli, Polytechnic of Turin
Prof. Andrea Manuello Bertetto, Polytechnic of Turin
Doct. Andrea Casini, ESA-EAC Cologne

Politecnico di Torino
July 24, 2019

I hereby declare that, the contents and organisation of this dissertation constitute my own original work and does not compromise in any way the rights of third parties, including those relating to the security of personal data.

. . . .

Dario Belmonte
Turin, July 24, 2019

Summary

This research examines innovative prognostic “model-based” algorithms able to identify the precursors of aerospace subsystems incipient failures, developed for primary and secondary aircraft flight control systems driven by electromechanical actuators. The proposed simulation model represents a virtual experimental bench on which innovative prognostic techniques are designed, as result of multi-disciplinary engineering analysis based on spectral signal processing. Electromechanical actuators represent the main test article simulated by a high-fidelity dynamical model to approximate primary flight control system behaviour in different operating conditions during multi-failures mode. A detailed simulation framework is developed to compensate, for designing an efficient Prognostics and Health Management study, a poor available experimental data since the electromechanical actuator is limited in onboard aircraft applications to non-safe critical secondary systems. Since the electromechanical actuator and the entire physical behaviour of the transmission a numerical model, to improve accuracy it considers also several non-linear behaviours both mechanical (end runs, back lashes, friction phenomena) and electrical (electrical hysteresis on controller commutation logic and electrical white noise).

During simulated operating conditions, four failure types are integrated in the same time with different degradation paths acting in concurrent mode on the same prognostic precursors. Proposed harmonic analysis approach can produce a big amount of simulation data organized in several “failure maps” database, able to highlight how each degradation path influences the dynamic responses in integration to the others. The main target is developing methodologies, that could be easily integrated on board, able to give a system health state report by comparison with the real-time acquisition system on aircraft during the ground pre-flight test by automatic avionics’ system check process, which can be periodically performed.

The comparison between real-time operative experimental data with the off-line simulated failures maps, coming from virtual test bench, ensures with accuracy to establish the health state for electromechanical actuation system driving aerodynamic surfaces of the primary control system.

The outcome benefits to early identify symptoms of progressive degradations before the actual exhibition of anomalous behaviours by defining FDI (fault detection and Identification) numerical model, improve flight safety reducing maintenance costs for this innovative actuator type in future all electric avionics' aircraft philosophy. The conducted study supports the relevance of harmonic analysis performed on prognostic precursors as mean approach to detect, and diagnose sudden unpredictable fault occurrences, before arising anomalous behaviour as clearly supported by the current findings.

Acknowledgements

And I would like to acknowledge …The PhD. Matteo Lorenzo Dalla Vedova, for the supporting effort to reach the conclusion of the doctorate program.

I would like to dedicate this thesis to ...

This dedication involves Eng. Giovanni Oddone, Mr. Mario Plancher, and finally M.D. Pina Arlotta, for personal estimation and friendly presence to this journey.

Contents

List of Tables

List of Figures

Introduction

Electrical powered actuation, for mobile aerodynamic surfaces, are in expansion in modern control system architecture both for innovative operational solutions and new design components to use in different scenarios. The improving performances of civil and military aircraft, due to higher airspeed that increases the aerodynamic load on the control surfaces, inspiring control system evolution from a manual mechanical transmission architecture to the hydraulic power control system. This evolution has as side effects an increasing complexity of the entire control system with mechanical transmission of pilot command and force feedback, hydraulic system with power generation pumps, valves, hydraulic circuits. To reduce complexity and weights further evolution occurs, in flight control systems, introducing electrical transmission of pilot command with Fly By Wire (FBW) architecture and reducing number and complexity for hydraulic circuits as in Airbus A320 in 1987. These evolution steps follow the More Electric Aircraft (MEA) approach, introducing hybrid electro hydraulic control system like Electro Hydrostatic Actuators (EHAs) as backup actuators for primary and secondary flight controls in the Airbus A380/A400M/A350 and military solutions as reported in [37].

The hybrid evolution to a more electric solution was enabled by integration between hydraulic and electric motors, with different ways in case of hydraulic actuators driven by electric motors, as in EHA where electric power is converted in to hydraulic one inside a self-contained component separated by hydraulic distributed circuits, or electric actuator used as a backup in hydraulic system failure conditions.

The electric power actuation system and transmission signals (e.g. FBW system) allow similar performances requirements associated with a remarkable weight reduction and complexity improving reliability, maintainability, safety and costs management by more efficient fuel consumption.

An additional, but not less important, added value related to more electrical architecture system evolution, consists in a less environmental impacts since hydraulic systems use polluting and contaminants fluids, needing removal specific processes. Moreover, actuation fluids are flammable where fluid leakages, representing major warning events for flight safety propagating on near subsystem, with fires and explosions.

The abovementioned advantages to improve the more electrical solution to a fully reliable All Electric Aircraft (AEA) configuration, are the basis for the next technical evolution step for aircraft systems, especially for the applications of the electromechanical actuator.

The modern solution based only on the electric power supply with electric driving force motors, in AEA use case design, are limited in most cases on civil and military aircrafts within secondary systems as landing gear braking cargo bay opening, and high lift devices flaps and slats surfaces, e.g. using Electromechanical actuators EMAs as frontline actuators for several secondary flight controls and landing gear braking in the Boeing B787. Although the removal of central hydraulic power distribution in the more electric system is a commonly used solution by EHAs actuators use, the EMAs are not yet sufficiently mature to replace conventional Hydraulic Servo Actuators (HSA) in normal mode for safety-critical functions as primary flight control systems. The conventional actuators maintain some advantages of EMA as back driving, overload protection and dumping, and major response to failure as easy hydraulic declutch and low risk of jamming and free run, therefore EMA installation is based on overcoming some technical challenges open to investigate deeper.

Indeed, Electrical networks on which EMA and FBW system is based, are affected by voltage spikes current transients, integration issues, in additional EMA are affected by heat rejection for thermal balance, reduced reflected inertia for dynamic performance, and stall force low performances. In the end, integrating electromechanical systems in safety-critical application as primary flight control systems implies other challenges about fault detection in all cases which could lead to a safety critical condition in an early stage. The EMA solution is barely extended, so fault developing method and propagation to other subsystem are not yet totally well understood, due to small operative database available on which tuning high fidelity simulation models to improve results accuracy.

The Reliability Availability Maintainability Safety (RAMS) state of art for EMA operational deployment, on large scale for civil and military aircraft, needs a focalized research path referred to PHM prognostics and health management, following these waypoints:

1. Identifying root causes for EMA faults leading unwished working conditions for safety and costs management.

2. Defining and measuring relation among concurrent incoming faults in an early stage before the degradation and propagation path becomes critical.

The presented work, concerns PHM discipline, developing simplified high-fidelity models as support of innovative algorithms for FDI able to early identify concurrent incoming failures on use of EMA in primary control systems. The main goal of this research consists in defining a smart approach to identify quantitatively progressive incipient concurrent failures acting on EMA by comparison among real-time monitoring sensors and failures maps defined by EMA simulation model as a virtual test bench to simulate with acceptable accuracy the actuator health state avoiding Finite Element Analysis (FEA) or more heavy elaboration on aircraft onboard systems.

The deliverables are mainly developed in MATLAB environment with related tools and add-ons e.g. Simulink, following the hereafter chapters hereafter summarized:

Ch.1 Prognostic and Health Management: short description for engineering discipline about PHM prognostics and Health Management representing the established context and background for the proposed research work.

Ch.2 EMA Electro Mechanical Actuator: a physical overview for BLDC operating principles, used as electromechanical actuator correlated with a reference simulation model and failures integrations.

Ch.3 Harmonic Analysis: starting from simulation boundary conditions, the main basis of Fourier time-frequency transformation is discussed within the Short Time Fourier Transformation process applied on prognostic precursors.

Ch.4 FDI Methodology for Rotor Static and Dynamic Eccentricity: proposed FDI faults detection and identification methods based on harmonic analysis for quantifying the unbalance magnetic pull for both static and dynamic eccentricity.

Ch.5 FDI Methodology Engine Order Track: harmonic results for unbalance magnetic pull are integrated with engine orders approach introducing faults interaction with the mechanical wear correlated with friction coefficients changes.

Ch.6 FDI Methodology For Short Circuits Turn To Turn: harmonic analysis for short circuits failure affecting harmonic system responses because this failure acts in concurrent mode with other failures on the same variables.

Ch.7 Conclusions and Future Developments: summarizing findings and main research area covered, with particular attention to research contributions and limitations of the current study, speculating future developments on presented research.

Chapter 1

Prognostic and Health Management

Prognostics and Health Management PHM, as described in [64], is an engineering discipline, with a strong correlation with other engineering disciplines related to Condition Based Maintenance (CBM), focuses on identifying and predicting when a component or a system will not able to perform its design functions compliance with reference requirements specifications. The PHM discipline becomes, in the last years, the main set of engineering activities whose deliverables are fundamental inside the decision-making the process for contingency mitigation in aircraft flight safety [81]. The science of prognostics is applied in several science fields, but in this work, we focus on the discipline application regarding aircraft flight controls systems. The main target is predicting the future performance of a component by assessing the degradation path from its expected operating conditions until the fault becomes critical or begin a warning propagation among near subsystems.

The degradation path in electromechanical systems is due to wear and ageing causes, integrated with environment operating conditions. The environmental conditions or flights conditions, lead incoming failures in the system, affecting other subsystems, generally compromising flight mission, reliability availability and safety, increasing related maintenance, spares and repair costs. The main expected goal is catching potentially catastrophic failures before they occur detecting incipient failures, by monitoring system until just prior to failure through identifying the specific *degradation path*. The PHM discipline integrates understanding the electro-mechanical failures processes, delivering advanced and innovative multidisciplinary methods for accurately predicting incoming failures within different application fields. In particular evident added values are introduced in Aerospace flight fields where concurrent safety problems may happen and supporting decision-making mission process. The main phases of an entire PHM process philosophy could be organized in the following organized tasks:

Detecting: The component at the beginning of its operational life is in *healthy condition*, in *"safe life"* aeronautical design criteria considers the multi-body assembly without initial defects, due to manufacturing and assembling as described in [54] in comparison with other rational design criteria. The degradation initiation may occur, the early detection phase is based on data gathering analyzing in real time by acquisition sensors. The choice of the monitored prognostic variables is a focal task for the detection phase since using sensors on component improves system complexity and costs. In addition, sensors have their own fail rate introducing errors, missing detection or false positive reading. For the above-mentioned reasons, should be conservative to use the same sensors framework deployed for feedback loop controls avoiding useless additional system complexity. The detection logic must determine in early time the degradation initiation on the monitored system switching between the *warning path* or the *normal* operations.

Diagnostics: after the detection of anomalies this phase is concerning to define a system health assessment by post-processing acquisition data coming from monitoring real-time system. In other terms diagnostics defines, after an early fault detection, a fault classification trying to assess a correct assignment of the main root causes for the considered measured signals trends. Several methods are employable for diagnosis and diagnostics merged into FDI methods, as for an example the most known is the Fault Tree Analysis (FTA), which analyze how the system can fall identifying the best way to reduce risk effects. The proposed research gets a position within the FDI methodology for EMA electromechanical actuator affected by a concurrent different type of failures by comparison between sensors responses and model-based failure maps for specific prognostic variables.

Prognostics: when a degradation initiation is correctly detected and identified, prognostic is the engineering discipline to predict incipient failures estimating the Remaining Useful Life (RUL) as indicated in figure 1.1 on page 7. Several methods are available to predict RUL as statistic approach of failure times (e.g. *Monte Carlo* method [70]), a data-driven approach based on conventional numerical algorithms or data mining as in [69] and [63]. But it's important taking into account that the prognostic approach is limited to detect sudden failures which occur without progressive propagation not able to be identified before system damages become effective on system performances. In this case, the system or component affected by sudden failures mode must be safer by redundancy application.

1.1 Prognostics and Maintenance

The PHM discipline improves safety by monitoring, detecting and predict the incoming and incipient failures, but another advantage for PHM approach consists to define system health state reducing cost related to maintenance avoiding malfunctions determining a system damages evolution. In the case of unpredicted damages on critical system, repair or replacement activities are classified as unscheduled maintenance tasks, that may have major cost on system life-cycle management. Usually aerospace system deployment has associated a set of scheduled maintenance interventions performing inspections for possible repairs or calendar replacement within the maintenance category called "Planned -Maintenance Tasks". There are other two types of planned maintenance tasks which are directly involved by PHM approach like *condition-based* maintenance and *predictive* maintenance tasks. The *condition based* maintenance tasks are a function of system health monitoring supporting decision-making process about repair or replacement processes as a result of degradation level assessment and path evolution evaluation. The predictive tasks are based on an RUL accurate evaluation considering some variability of operational life-cycle load and conditions as reported in figure 1.2.

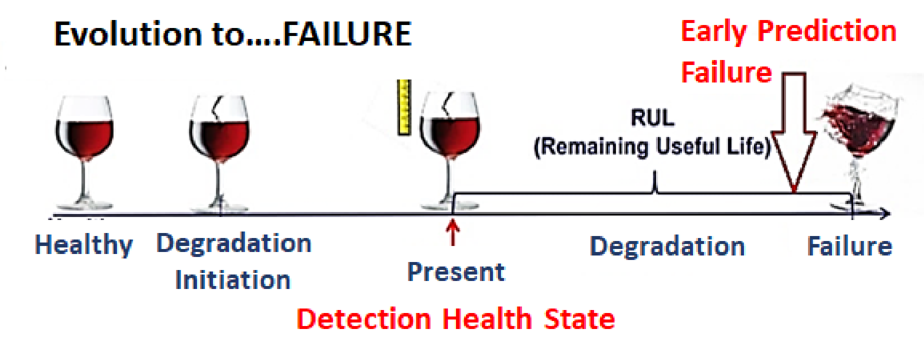

Figure 1.1: Logic Evolution for Detection, Diagnostics, Prognostics activities of PHM Prognostics and Health Management basic process

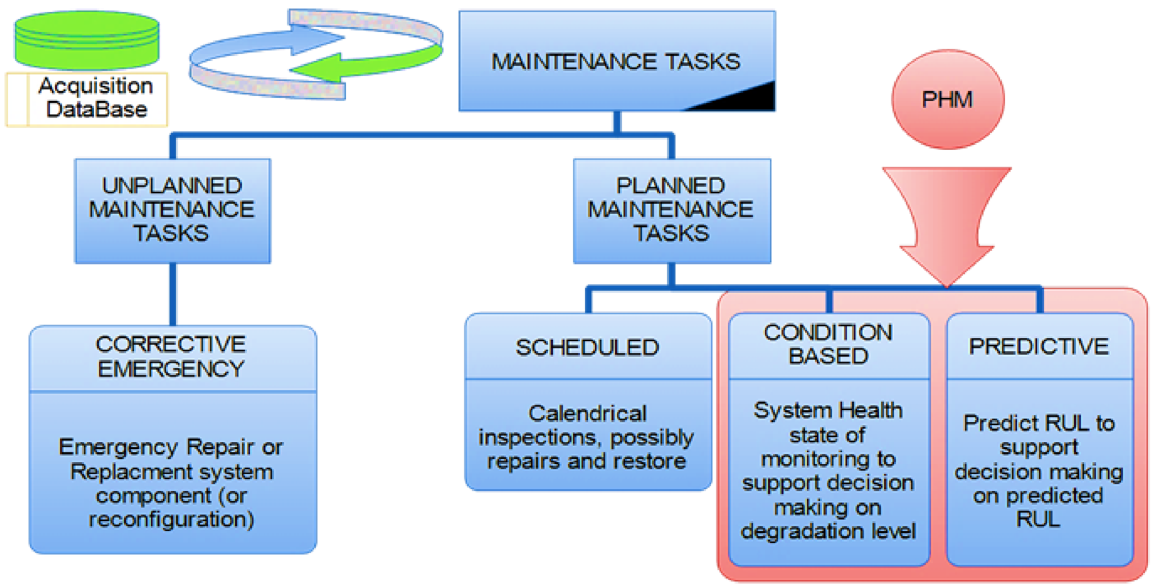

Figure 1.2: Impacts of PHM disciplines to improve effectiveness on safety and reducing cost referred to Maintenance organization tasks

If the RUL is defined as the time between the fault detection and when the failure incoming to degrade the component or system functionalities, an early prediction defines a predicted failure before it occurs. An early prediction defines a time interval between the time needed for elaborate the predicted failure and the time to realizing the corrective actions. Therefore, an accurate RUL estimation should be the best solution, but in many occasions imprecise or incomplete input information the robustness predictive framework couldn't ensure it without a confidence time interval in which the fault probability is greater than 95%.

1.2 Health Assessment Classification

Many methodologies are used to perform health assessment, composed by fault detection, diagnostics, prognostics processes, based on a wide range of data and information so they evolved in a wide range of different approaches. These methodologies can be classified on how data sources are managed by elaboration tasks in two main categories:

1. **Model-based approach**: based on mathematical simulation modelling derived from first principles (e.g. physics disciplines based) to simulate system behaviour;

2. **Data-Driven based approach**: referred to use acquisition historical data to learn system behaviour; this approach doesn't necessarily require a system model but could define models and methodologies learned by sensors acquisition data;

This canonical classification is becoming even more obsolete in modern applications because all approaches use prognostics models in different ways and all these models are driven by acquisition data to improve matching with healthy and degradation system states. The knowledge of mathematical model known physical law and behaviours should be used to develop a simulation model, and when experimental operational big databases are available, the model can be tuned learning from experimental data. There are a full model-based prognostics algorithms when deployed simulated results are used as input to other simulation models able to define by new boundaries conditions, different type of failures, different degradations path.

A further classification can be performed on prognostics methodologies based on when the prognostic evaluations are performed, based on response time respect of operational applications [77]:

1. Online or Real-time PHM

2. Off-Line PHM

The presence of an onboard monitoring system is the minimum requirement to develop a real time PHM process, based on acquisition data sensors to evaluate the health state, detecting the event of interest that could be:

1. System or component failures;
2. Deviations of functional or performance requirements specifications;
3. Anything of importance the PHM process need to predict to support decision-making the process to end safely the mission;

The real time PHM is often used in electronics by Built In Self-Test (BIST) used onboard of all modern avionics and safety critical system allowing performing on flight tests to verify all electronics based equipment. The off-line PHM processes are based on complex simulation models using acquisition data collections where computing performances are not compliance with onboard calculation system. Failure modes effects and critical analysis (FMECA) process, need to use a wide historical operational database to evaluate the probability of failure modes. The FEA models are employed to define the physics of failures, both FEA and FMECA are applicable only within off-line PHM.

1.2.1 Research Study Case in PHM

The proposed approach, in this research, is based on the innovative use of full model-based fault detection and identification framework, identifying the health state of actuator used in primary aircraft flight control system. An EMA simulation model is developed, able to describes physical behaviour under different boundary conditions a representative of some real operating conditions. The simulated operational variables are time-dependent signals used as prognostic precursors simulating EMA affected by progressive different failures types, acting in concurrent mode, as rotor static eccentricity and stator phase turn-to-turn short-circuit, rotor dynamic eccentricity and mechanical wear on transmission lines. The simulated results are employed as input for further numerical algorithm analyzing proper system operational parameters, able to put in evidence the corresponding degradation path, based on spectral harmonic analysis techniques described in chapter 3 on page 53.

The proposed FDI algorithm, whose a part is published in [14], showing adequate robustness and a suitable ability to early identify EMA malfunctions with low risk of false alarms or missed failure. The main concepts reported in this paper are related to the design a reliable and fast FDI routine focused on the diagnosis model-based approach and on the parametric estimation task alerting before anomalous behaviours take effects on system and flight safety. The obtained results prove that this full model-based FDI method is able to provide early and reliable identifications of the considered set of system malfunctions, reducing the risk of false alarms or undetected failures. Furthermore, it can operate comparing the simulation failure maps database with acquisition data collected by sensors that already equip the actuation system or derived from the post-processing of the real raw measurement. It must be noted that PHM approaches can be applied on EMAs in a more efficient way (if compared to the case of the most known electro-hydraulic actuators) because in EMAs additional sensors are not required to acquire the prognostics precursors indicated in 3.1 on page 53. The electrical nature of the chosen prognostic precursors are more easy to acquire and manage respect some other similar physical behaviour related to structural vibrations acquisition. In fact, as reported by several studies on electrical motor equipped with accelerometers, to better understand vibrational motor responses related to static and dynamic eccentricity.The use of accelerometer is useful in a test rig environment, but on an aircraft are affected by reliability issues related to their assembly on a test article. In addition, it must be noted that this integration between real and virtual sensors, combining and processing information from multiple sources, can increase the effectiveness and robustness of the FDI algorithm. From an operational point of view, this FDI approach can be easily integrated into a system control process periodically performed in a real time PHM process by maintenance during pre-flight checks.

1.3 Flight Control Systems and Electrical Power

Among aircraft on-board equipment, the flight control systems are essential to ensure Maneuverability, flight control forces acting on aircraft on safety conditions. The proposed FDI methodologies developed in the present work are applicable to a wide range of electromechanical actuators installed on the modern and future primary flight control system for civil and military aircraft. The main function of flight control systems is modifying the results of pressure forces distribution around lifting aerodynamic surfaces by moving mobile parts as indicated in figure 1.3. The actuation systems are classified between two main architecture types: direct flight controls and servo- actuated controls. The direct flight controls provide actuation power is given by pilot through a mechanical transmission system, but needed power is a function of aircraft, mobile surfaces dimension, deflection angles and especially flight velocity. Therefore, this control system architecture is not able to satisfy the minimum requirements of modern civil and military aircraft but using is limited on the glider and small aircraft categories. Therefore, for most used civil and military aircraft with high performances, and consequently with higher hinge torque amplitudes, servomechanism actuation systems are used as flight control systems. This system architecture is based on using actuation components to move mobile aerodynamic surfaces by hydraulic or electro-mechanic actuator through pilot commanded positions. The pilot commanded positions can be transmitted to the actuator in different solutions with different complexity and weight, even if flight control system growth with the size and performance of the aircraft. In traditional hydraulic power architecture, the pilot command is transmitted by mechanical transmission to servo valves closed by mechanical feedback linkage when controlled surface reaching the desired position. But the mechanical force feedback loop in traditional hydraulic configuration didn't ensure a very well direct force feedback to the pilot avoiding tactile feedback of airspeed on aerodynamic surfaces. To overcome this feedback problem, artificial feel systems were developed, until the incoming of new architecture called FBW the solution most used on modern aviation solutions able to integrate *CCV* (Control Configured Vehicle) as:

- *C.A.S.* Command Augmentation System;
- *S.A.S* Stability Augmentation System: system to improve flight stability, designed specifically for aircraft with intrinsic flight instability e.g. Eurofighter Typhoon; this system can reduce turbulence effects with correspondence fatigue load improving pilot and passengers comfort in all-weather conditions;
- *Autopilot System*;

The main features of the FBW control system replace mechanical transmission flight control with an electronic interface transmitting by wire and controlled by flight control computers able to drive actuators of each control surfaces providing expected static (or low variable) and dynamic responses. In other words, FBW allows integrating the full pilot authority on flight surfaces with several corrections given by control system elaborations, improving stability, aircraft management, flight quality and especially safety. In system flight control design, some project criteria must be considered:

- **Static Stability:** the surface position after a transient phase must correspond to position driven by pilot compliance with some specific *"correspondence rules"*.
- **Reliability requirements:** on FBW systems transmission channels and elaboration systems could be improved by redundancies with relatively low cost and

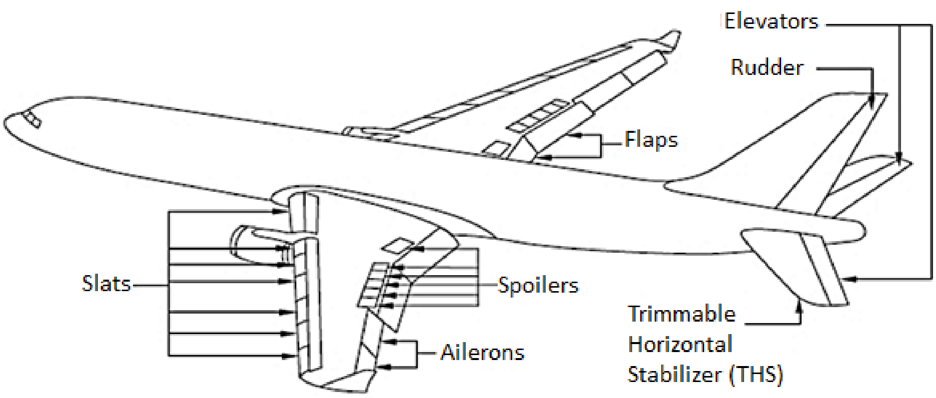

Figure 1.3: Typical Flight control surfaces on Civil Airliner for primary and secondary flight control system

weights. The allowable probability to lose aircraft control is fixed to $2 * 10^6$ per flight hour for civil aircraft and $2 * 10^9$ for civil aircraft.

- **Dynamic stability:** the dynamic behaviour of the mobile surfaces must be compliance to specific dynamic requirements avoiding divergent dynamic instability that could activate warning aeroelastic structural phenomena.

- **Fault requirements:** these requirements are applicable both on simple or multiple failure modes, the only allowed failures don't affect aircraft performances.

The main differences, among servo command architectures, are based on two types of flight command systems: primary and secondary control system. The primary control systems are proportional to pilot command allowing continuous activation among all flight phases. The main functionalities of primary surfaces are modifying aircraft trajectory generating, around body reference system axis (roll, pitch, yaw axis), aerodynamic torque due to angular surface deflections. The force feedback, for primary flight controls, is important to improve control giving to pilot to understand what aerodynamic forces acting on surfaces during flight. The secondary flight control systems (e.g. flaps, slats, stabilizers) are not proportional but assume fixed moving positions modifying wing aerodynamic coefficient (e.g. *Cd* drag coefficient, *Cl* lift coefficient). The fixed surfaces position must be continuously kept during takeoff and landing manoeuvring, the two-main flight operating phases for this type of flight control system. In traditional flight control architecture for aerodynamic surfaces, but also for all-electric architecture as in

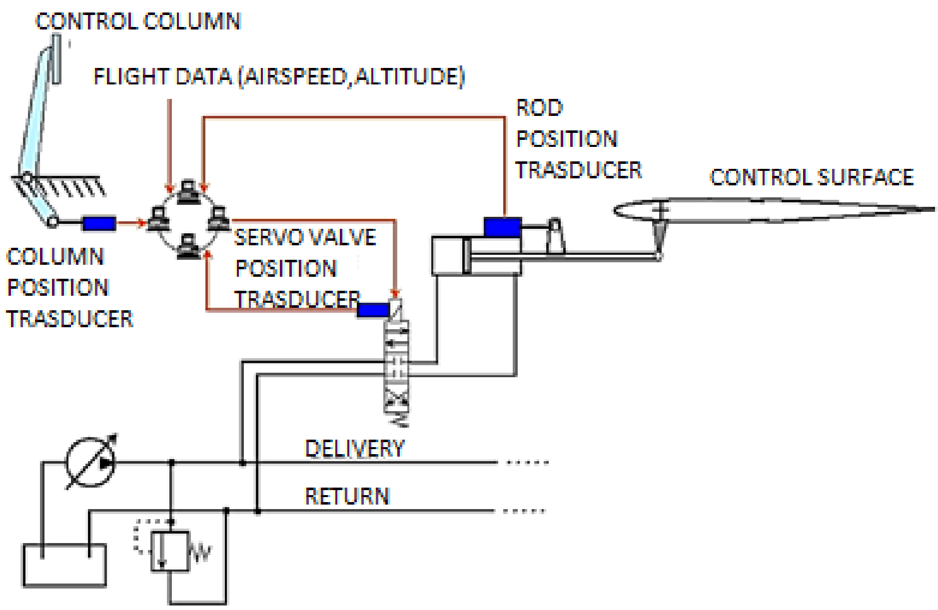

Figure 1.4: *FBW* simplified architecture for a slight hydraulic control system

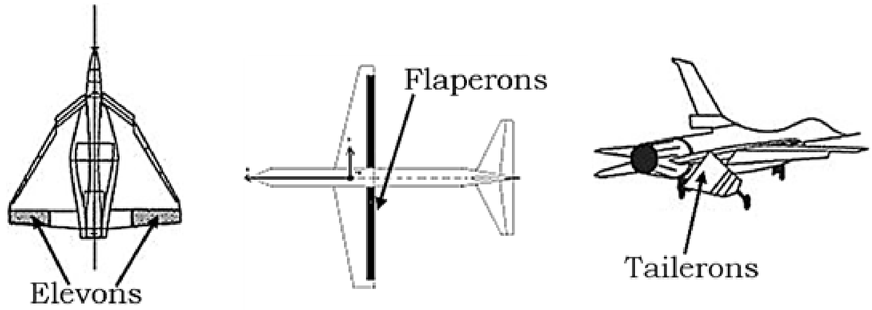

Figure 1.5: Flight Control System non-conventional aerodynamic surfaces solutions

[50], for each type of commands is corresponding to a specific type of surfaces, indeed for primary flight control system the surfaces as reported in fig. 1.3 on page 11 are:

- Ailerons: control surfaces installed on the wing trailing edges to generate rolling moments about body X-axis;
- Elevators: control surfaces located on the horizontal fletching trailing edges, to generate a pitching moment about body Y-Axis;
- Rudder: control surfaces mounted on the vertical fletching trailing edges, to produce a yawing moment about body Z-Axis;

The typical surfaces configuration architecture for a secondary flight control system, as reported in fig. 1.3 on page 11 are following classified as [2]:

- Flaps;
- Slats;
- Stabilizers and Aerobrakes;

On fighter aircraft, non-conventional aerodynamic surfaces solutions are available to generate control moments about more than only one body axis by single surface moving as following reported in fig. 1.5.

In this research, we focus on electromechanical actuator used for primary flight control systems that are safety critical than secondary control systems especially for the set of possible incoming failure analyzed by proposed FDI algorithm improving safety and remarkable reducing maintenance cost management. As mentioned in previous paragraphs, the aeronautical industry is oriented towards MEA and sequential evolution of AEA all-electric aircraft, to have a single electrical power generation for all avionics and aircraft system equipment. This trend is to replace the hydraulic and pneumatic generator system with power drive electrical, implies increasing electrical power with generators driven by engines. The increasing of electrical power demand onboard civil and military aircraft is due to increasing equipment number which needs a different mixed voltage systems as illustrated in [4]: *AC* alternate current with $405VAC$ at variable frequencies, $200VAC$ at fixed $40Hz$ frequency, and *DC* direct current $28VDC$ and $270VDC$ called High Voltage Direct Current (HVDC).

The engines by PDU power Drive unit generates *AC* electrical power, the *DC* power comes from Transformer Rectifier Units (TRUs), they introduce harmonic content into *AC* bus. The *AC* generation is performed by the Integrated Drive Generator (IDG) integrated system between an *AC* generator and Constant Speed Drive (CSD), a transmission type generates an output speed constant shaft with an input shaft with variable speed, in other words an hydro-mechanical system connected via main engine gearbox, with the output of three-phase currents at 115V with 400Hz constant. The Continuous evolution in power electronics leds electric aircraft architecture to Variable Speed Constant Frequency (VSCF) system as more efficiency and flexible solution since its main components can be distributed throughout the aircraft structure. This solution, is composed bay three-phase synchronous generator and solid-state converters, and it deployed on *B787* (power rating $1400KVA$) and *A380* (power rating $800kVA$) civil aircraft, generates from variable shaft speed a variable frequency *AC* from $360-800Hz$ with output $200VAC$ as reported in *ATU* autotransformer unit in a general architecture schema shown in fig. 1.6.

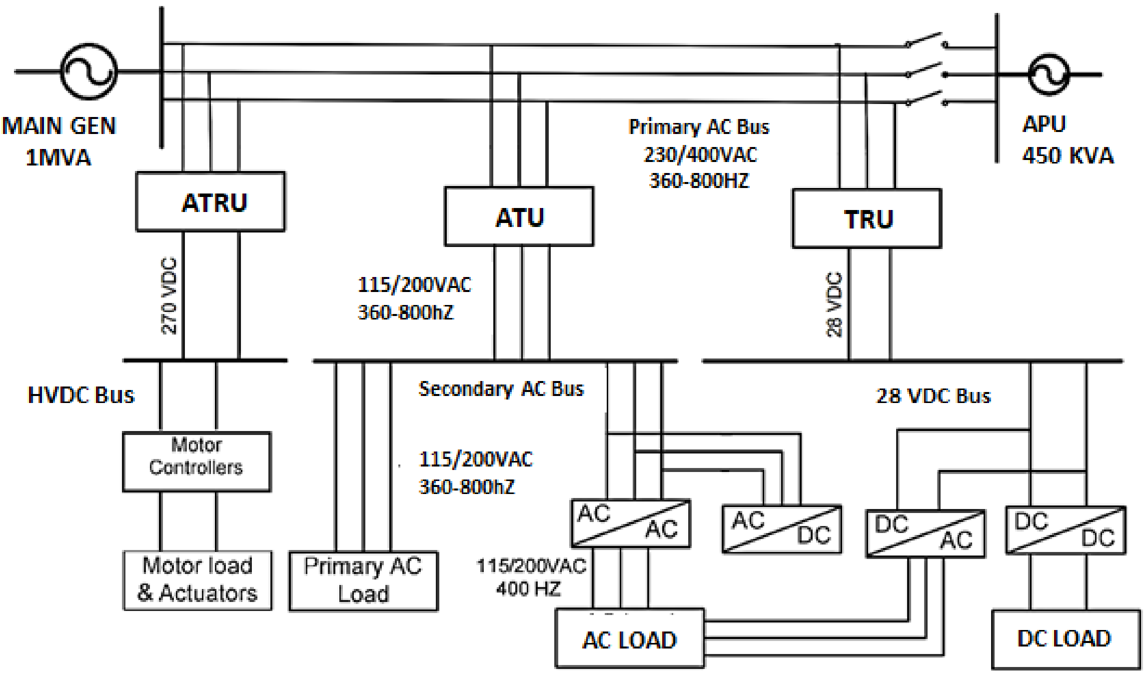

Figure 1.6: Power electronics architecture: *ATU* Autotransformer Unit, *ATRU* autotransformer Rectifier Unit, *APU* Auxiliary Power Unit, *TRU* Transformer Rectifier unit

The primary *AC* bus generated by VSCF, and on the ground by *APU* auxiliary power unit a pneumatic system and converted to HVDC bus by Auto-Transformer Rectifier

Unit (ATRU) managed by the motor controller to drive actuators and hydraulic pumps of primary and secondary flight control systems. The secondary AC bus at $200V\,AC$ and frequency of $380-800Hz$, power through ATU autotransformer unit the primary AC load. The other DC load are powered by a secondary DC bus transformed by TRU from primary AC bus with $28V\,DC$ and if needed in critical conditions it could be transformed to secondary AC bus using DC/AC power converters. Once electrical power is available in multi-voltages and frequencies the electrical services could be operated in a wide range of functions spread throughout all the aircraft structure. About half of total electrical load is powered by HVDC 270DC managed by different fuzzy logic controls as in [5] allowing a voltage ripple $\Delta V = \pm 5V$ compliance with aircraft international regulatory [1]. The main type of actuators driven by electrical power by wire is EHA largely used in civil aircraft and electromechanical actuator the future of aircraft actuation system.

1.3.1 EHA Electro-Hydrostatic Actuator

In MEA more electric aircraft electro-hydrostatic actuators are widely used for primary control system replacing traditional hydraulic actuator based on centralized hydraulic power units with three supply lines for each hydraulic actuator. The electro-hydrostatic actuator represented in fig 1.7 allows generating distributed hydraulic power to the hydraulic actuator, by using an integrated package with an electric pump powered by an electrical supply system. Inside the EHA component a variable speed brushless DC motor drives a fixed displacement axial pump that hydraulic fluid is pressurized to move a hydraulic cylinder connected to the mobile surface. Feedback Linear Variable Displacement Transducer (LVDT) sensors measure position piston, closing position feedback loop to the main control system, integrated with pressure relief and cavitation valves with a small embedded reservoir to allow thermal expansion effects and asymmetrical jack operations.

1.3.2 EMA Electro-Mechanical Actuator

A modern alternative to EHAin [38], among power by wire actuator architectures simpler increasing efficiency and weight reduction, is the electromechanical actuator EMA connected to a mobile surface by a gear reducer and/or ball or roller screw jack able to convert rotary motion into a linear one. As previously indicated in this work there are several issues to limit the use of EMA in modern flight control systems. One of the main issues is the full knowledge of EMA fault modes with the consequence of restricted reliability. The only EMA extensive use for primary flight control is employed on small UAVs with limited maximum torque required by minimal mission profiles. A typical electromechanical components schema is reported in fig. 1.9 The considered actuator architecture in this work, can be analyzed considering the main system composed of six principal subsystems illustrated by [53]:

- ACE: a control electronics unit that closes the position feedback loop- comparing the command input with the actual position, elaborating corrective actions (by means of a PID control logic [40] and [9]), and regulating the reference current I_{ref} to Power Drive Electronics;
- PDE: Power drive electronics regulating the three-phase electrical power coming from power by drive system considering also the feedback from BLDC motor;
- Electric Motor: is a three-phase BLDC with Pulse Width Modulation (PWM) sophisticated digital control system;
- Reduction Gear: is a gearbox that reduces rotor angular speed increasing the supplied mechanical torque;
- Nut screw jack: is a mechanism allows converting rotary output motion from gearbox into linear motion (this type of ball or roller screws are more efficient than traditional acme screw because they are based on rolling friction lower than coulomb friction;
- RVDT: indicates a sensor network able to close control feedback loop (e.g. control loop acting on phase currents, motor angular speed and output screw position;

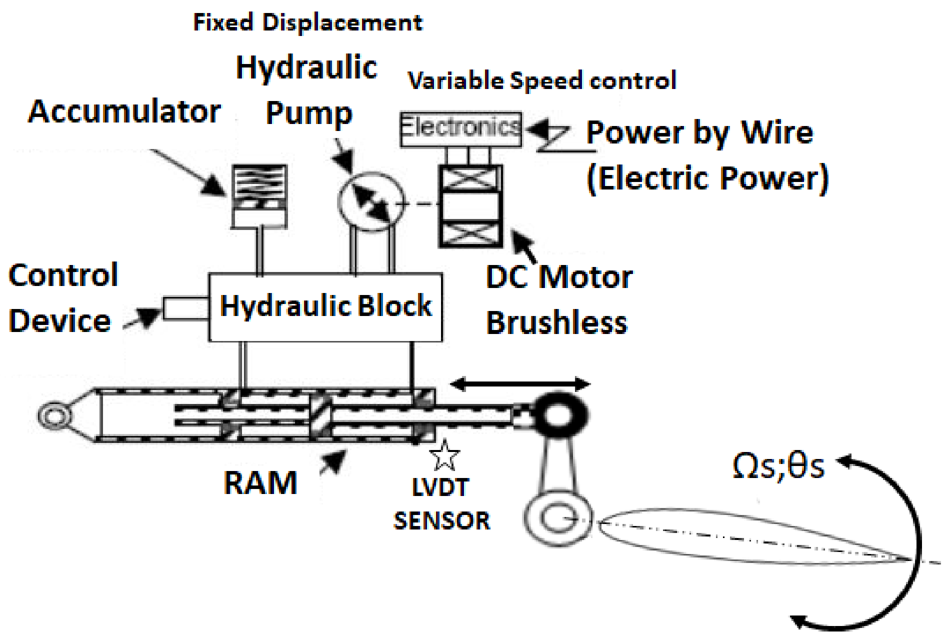

Figure 1.7: A qualitative schema for *EHA* Electro Hydrostatic Actuator main components

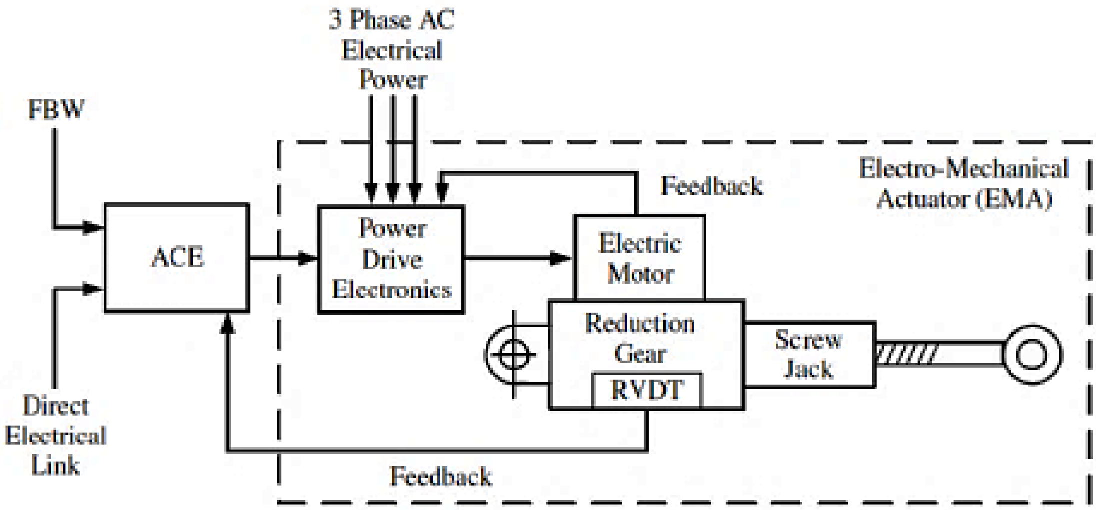

Figure 1.8: A qualitative schema for EMA Electro Mechanical Actuator main components

The gearbox is the mechanical interface between the BLDC three phase brushless motor and the nut screw jack mechanism and request a high transmission ratio since to have a good compromise on motor weight and volume delivering a low torque with high rotational speed. On the other site, the mobile surface requires a high torque to get commanded position on external aerodynamic load. The load framework, acting on a wing, is an estimate hinge torque at sea level with air density $\rho_{SL} = 1.225\ [Kg/m^3]$ as a function of maximum aircraft velocity, mobile surfaces geometry dimensions, deflection angle and safety factor that for primary control surfaces is fixed to 2 times of first hinge torque estimation. The requested transmission ratio τ is defined as:

$$\tau = \frac{\dot{\theta_m}}{\dot{\theta_u}} = \frac{1}{\eta_m}\frac{T_u}{T_m} \tag{1.1}$$

In the formula (1.1) $\dot{\theta}_m\dot{}$ motor speed and $\dot{\theta}_u\dot{}$ mobile surface speed, they are expressed in RPM, and η_m is the gearbox mechanical efficiency. The estimation of hinge torque action on the mobile surface is defined by the equations (1.3) and (1.2).

$$C_\mu = K_A \cdot \alpha + K_B \cdot \delta_I P \tag{1.2}$$

$$M_{Hinge} = \frac{1}{2} \cdot \rho_{SL} \cdot U^2 \cdot S_{IP} \cdot C_\mu \cdot Cmean \tag{1.3}$$

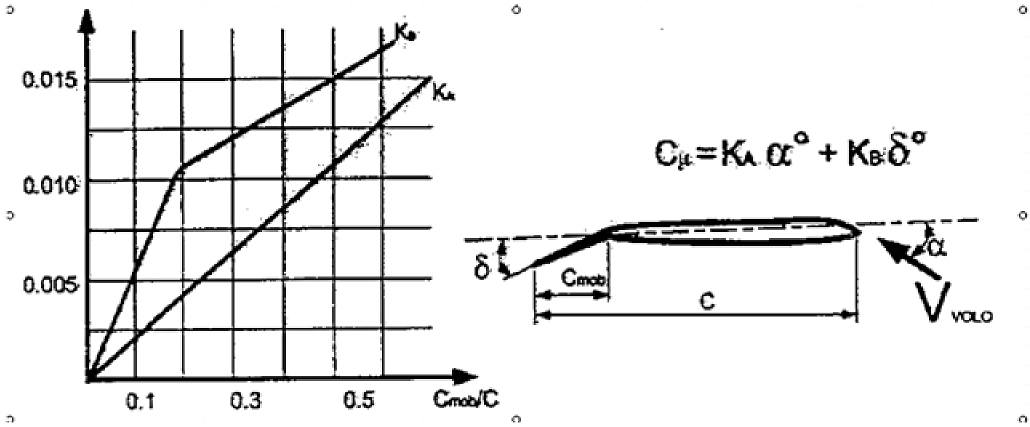

Figure 1.9: Hinge torque coefficient C_μ as a function of the geometrical profile cross section parameters and aerodynamic wind angle α to estimate by Diagram K_A and K_B

The formula in (1.2) calculates an estimation of hinge torque coefficient C_μ by estimating the coefficients K_A and K_B with reference diagram in fig.1.9 as a function of the following wind profile parameters:

1. α : incidence angle of air on the wing leading edge expressed in [Deg];
2. δ : deflection angle of primary mobile surface expressed in [Deg];
3. C : total wing section cord at maximum deflection angle;
4. C_{mob} : mobile surface cord at maximum deflection angle;

The estimation of hinge torque coefficient C_μ is preparatory to calculate hinge torque M_{Hinge} by (1.3) equation considering C_{mean} as the mean cord of mobile surface expressed in $[m]$ and S_{IP} surface area of wing mobile surface in $[m^2]$. The gearbox drives a ball or roller screw jack mechanism to convert rotary into linear motion connected with mobile surface with higher efficiency than the lead screw. This efficiency is based on rolling resistance among surface in relative motion instead of coulombian friction (static and dynamic) that have another advantage as supporting the greater maximum load and lower wear with the same operational conditions.

Chapter 2

EMA Electro Mechanical Actuator

-

2.1 BLDC Brush-less Electric Motor

The BLDC motors, also known as Electronically Commutated Motors (ECM) are synchronous motors, in which shaft rotation is synchronized with a rotation period of rotating magnetic field, generated by electronic commutation to drive each stator supply phases through closed loop controller.

The electronic controller provides to the driving of three phase supply phases, that generate voltage pulses to motor windings, controlling speed and torque on the permanent magnetic rotor. This brush-less solution is more efficient, with high power to weight ratio, than brushed DC motor that to create torque in a unique direction needs to commutate and reverse currents into windings every 180° degree of each rotor turn by a mechanical commuter. This mechanical commutator is designed on a rotating cylinder subdivided into contact segments connected to rotor windings.

The brushes are stationary contacts in graphite material in contact to these rotor segments providing currents to rotor windings. This mechanical commutation, based on brushes contacts, presents many issues to aerospace purpose related to friction due to sliding along rotating connection segments that cause significant power losses, material wear. The brush wear releases dust, therefore, this motor architecture is not suitable for low particulate or sealed applications, moreover sliding contacts are associated with voltage drop reducing energetic efficiency. In the aeronautical applications the current switching causes sparks in correspondence of contact discontinuities, increasing fire hazard probability in the presence of fuel or oil within the operative environment and inducing electromagnetic noise interference in the near electronics subsystems.

The solid-state electronics commutator is the main solution on which is based on the brush-less DC motor, replacing the brushed contacts avoiding all above-mentioned issues related to using a mechanical commutator. Electronics Hall effect sensors mounted on the BLDC determine the rotor position angle allowing the control system to switch windings currents generating a rotating magnetic field. The rotating magnetic field drags the fixed magnetic configuration of the rotor composed by permanent magnetic poles, by attracting the opposite magnetic polarization on the next winding phase in motion direction and repulsing the back-phase winding respect the rotor position as in fig. 2.1. There are also BLDC motor in a sensorless configuration that is able to measure rotor

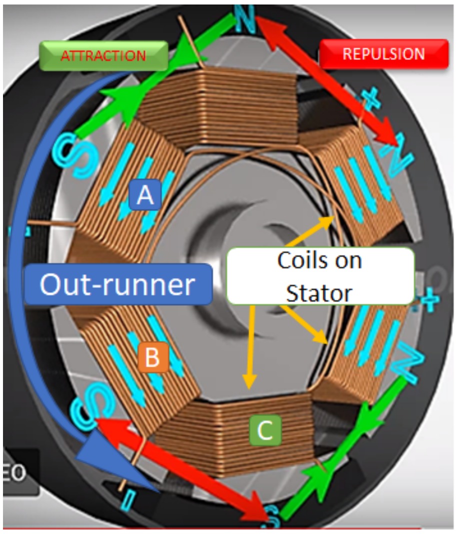

Figure 2.1: Magnetic excitation three-phase BLDC *"out-runner"* configuration where one phase is polarized attracting opposite polarity pole and repulsing the same polarity poles

angular position by a counter electromotive force acting on the not driven coils , but this cheap solution are based on open loop configuration and the Electro Motive Force (EMF) measurement loses accuracy at low angular velocity and an irregular torque is developed near null velocity, the main position in aircraft surfaces actuator to keep commanded pilot position. Indeed, the brush-less motor develops a maximum torque in stationary condition decreasing as velocity increases.

On the other side at the maximum torque at stationary condition is limited by *BLDC* thermal balance, indeed the maximum power can be applied for a limited time interval in which heat increase by joule effects on windings coils reducing magnetization intensity and inducing thermal fatigue on coils insulation that causes incoming failures related to short coils degradation.

2.1.1 BLDC Components

A large body of literature and technical books pay particular attention to BLDC construction configurations, where a magnetic permanent rotor component is driven by rotating magnetic field generating by stator windings coils commuted by solid-state electronic control system. Traditionally, the main BLDC configurations are two: a conventional *"in-runner"*, where the permanent magnets on the rotor are inside the stator, and *"out-runner"* configuration where the stator coils are placed into the core motor inside the rotor surrounding the core. In this study, only *"in-runner"* configuration will be considered because it's the best solution to have best spin velocity with the same electrical power supply coupled with a reduction gearbox increasing torque.

The BLDC stator is manufactured in laminated steel with vanes to carry phase windings, arranged in three phases power supply in two main configurations: a delta configuration in which each supply phase is connected in triangle circuit and star Y shape winding in which all the phase windings are connected to a central star point as parallel circuits and the power is applied to the end of each winding by switching control system as reported in fig. 2.2. In delta connection, each phase voltage is equal to the line

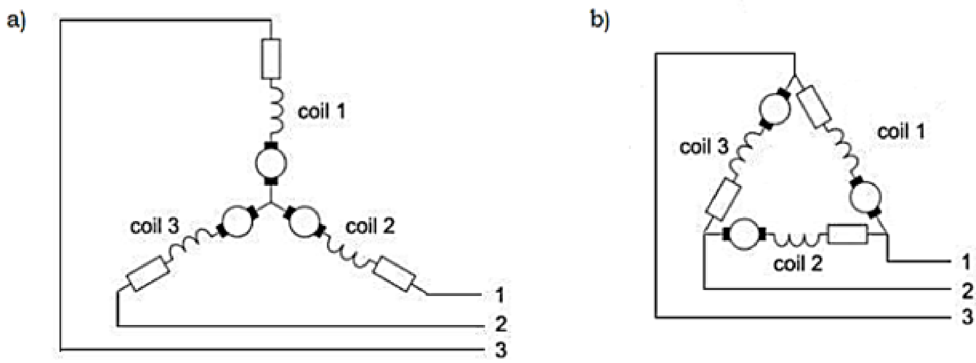

Figure 2.2: Three supply phases: **a)** Y star connection and **b)** Δ delta connection

voltage, while in star connection phase voltage is equal to $1/\sqrt{3}$-line voltage. Therefore considering the same line voltage applied to both supply configurations a higher line current flow circulates in the delta coils developing a higher torque compared to star connection configuration. But the previous condition is available at a high rotation speed, otherwise the star connection motor is able to develop higher torque at low-speed and generally is a more efficient wires configuration.

The stator steel lamination can be manufactured with slotted and slotless as shown in fig. 2.3, where the windings organized without vanes grouping develop lower inductance therefore at the same supply power and load this BLDC motor configuration run higher speed than slotted since phase commutation could be faster. The magnetic interaction, between rotor permanent poles and stator teeth, causes a variable reluctance during rotation generating an irregular motion at a low speed called "cogging torque".

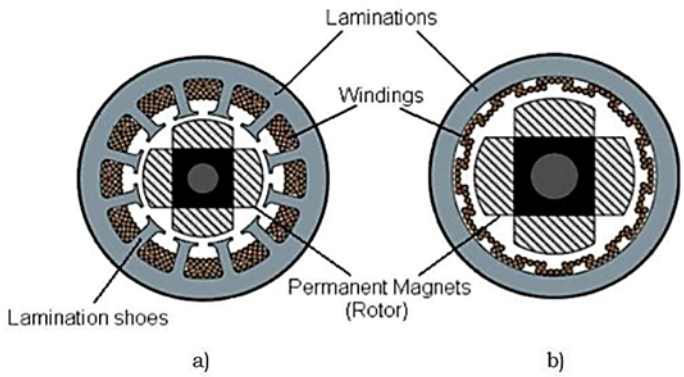

Figure 2.3: BLDC stator coils manufacturing architecture: **a)** slotted and **b)** slot-less configuration

This irregular torque phenomenon is less felt by slotless stator configuration where the absence of steel element among windings determines a more regular magnetic field distribution over all air gap.

2.1.2 BLDC Operating Principle

The synchronous DC motors are controlled by current and voltage phase waveforms, by dedicated control system using also as input back counter EMF due to magnetic flux density distribution over the air gap. These waveforms could be a square wave, for DC motor or sine wave for brush-less AC motor, but although AC supply delivers a more regular torque, in aeronautical application are most used BLDC configuration more simply to manufacture and control, therefore in the presented research the study focused on BLDC for primary flight control and actuation system.

The main operating principle is based on embedded control logic evaluating angular rotor position feedback loop to activate the properly phase commutation logic to satisfy the commanded position on aircraft surface. The rotor position is measured by different types of sensors as hall effect sensors, Rotary Variable Differential Transformer (RVDT), a rotary encoder. (RE). Although as in [15] sensorless control techniques for rotor position detection are deployed in some electrical drives architecture, in most applications the position control loop is based on hall effect sensors, as the best compromise between cost detection angular position accuracy, and reliability. The sensors with an accuracy of 6°, are positioned evenly spaced of 120° over revolution development as indicated in fig. 2.5 on page 24, reporting a single pair pole rotor to simplify control logic explanation.

The hall sensors identified by *H1 H2 H3*, detect the magnetic field intensity of rotor poles during rotational motion, sending a voltage signal to control system processing the phase supply following a specific commutation logic by power transistors on each supply phase configured with star centre connection as indicated in the electrical scheme shown in 2.4. The decoder circuit applies the commutation logic frequency by integrating the commanded pilot position on the aerodynamic surface with angular rotor position, controlling current and voltage phase applying the proper torque and velocity on the transmission shaft. The simplified description of commutation logic is reported in fig. 2.5, starting in the initial condition *I)*, where the north pole is positioned on *H2* sensor with maximum magnetic field density, while *H1* and *H3* are positioned over the south pole, the corresponding supply commutation logic is phase A unpowered, phase B connected to supply voltage and phase C is connected to ground of the circuit.

In the next rotor displacement of 60 degrees, in condition *II)*, the south pole passes under *H3* sensor with maximum magnetic field density while *H1* and *H2* are positioned over the north pole, as results on commutation logic, phase B is still connected to supply voltage, while phase C is unpowered and phase A is connected to ground.

The fig. 2.5 presents, in numerical order, the commutation logic over an entire rotor revolution with different orientations of permanent magnetic pair pole, and corresponding switching sequence as rotor position function. The six-power transistors, arranged in a bridge configuration, power two phases on three allowing in each time the cooling of unpowered phase reducing maximum torque available with all supplied three-phase conditions as a compromise between mechanical performance and thermal fatigue on coils. It is noticed that in running configuration with stator laminated with vanes for phase windings, allows a better cooling than other BLDC outrunner by placing cooling wings on the external hub and internal airflow.

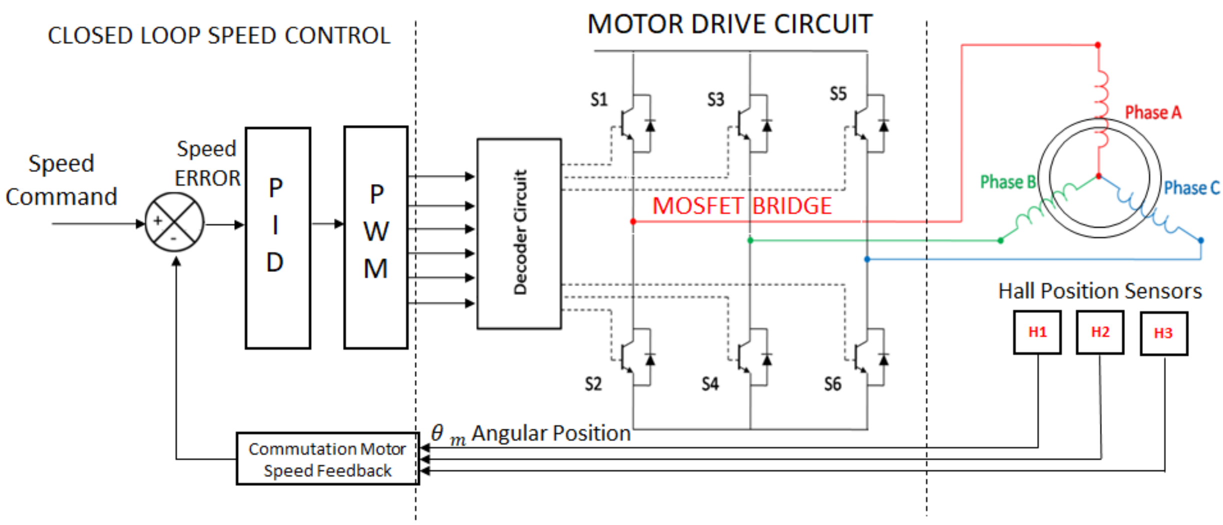

Figure 2.4: Electrical scheme of the BLDC Inverter control system of three-phase stator

A summary of commutation logic is available on table 2.1 on page 25 indicating also the *MOS* (Metal Oxide Semiconductor, transistor) activating conditions for all six power transistors in which appears the electrical rotational angle θ_e as convention coming

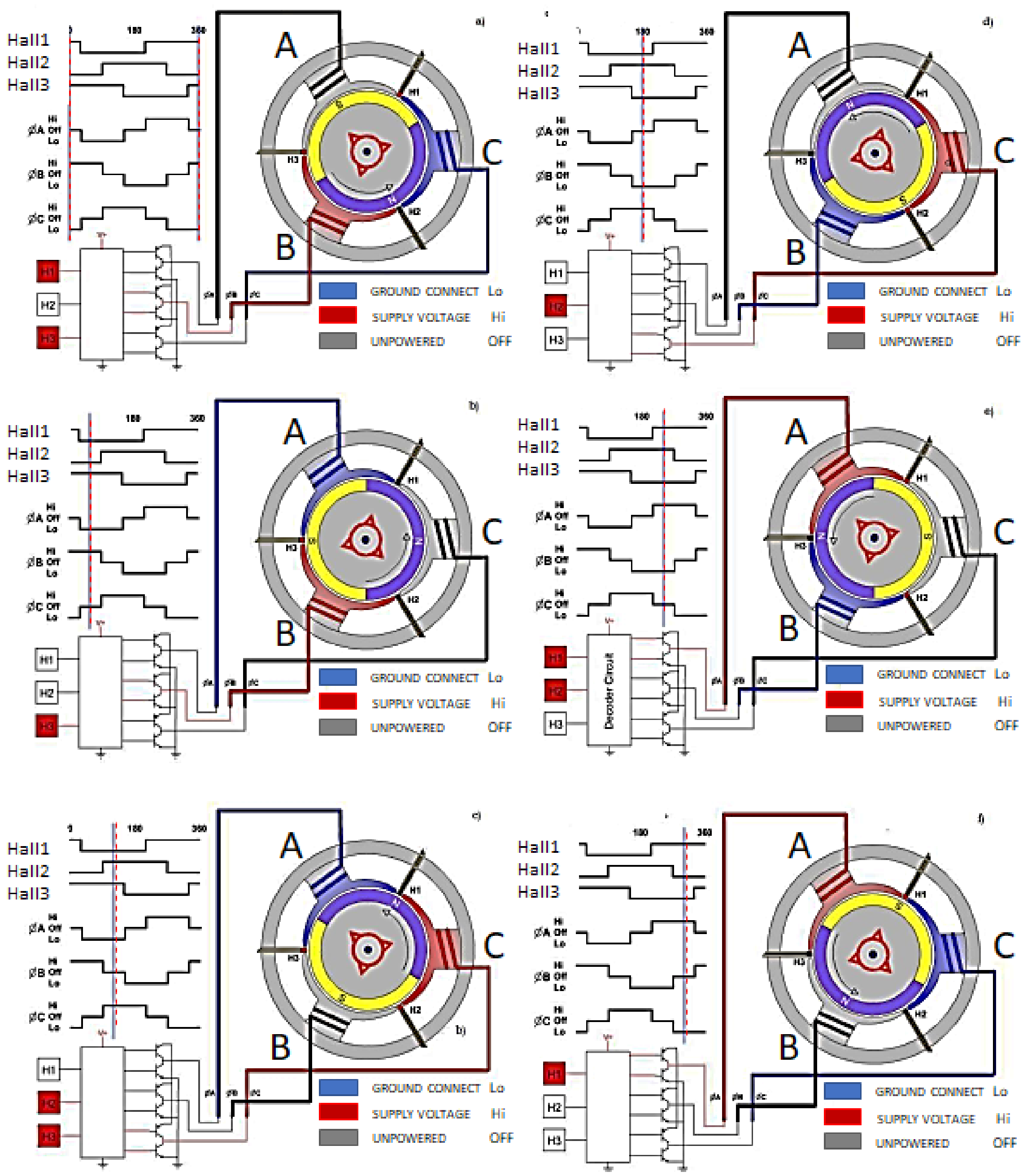

Figure 2.5: BLDC stator coils commutation logic on three phase supply coils

from the mechanical rotational angle θ_m as a function of P_p rotor pair poles in (2.1).

$$\theta_e = \theta_m \cdot P_p \tag{2.1}$$

Table 2.1: Boolean Hall Sensors *H1,H2,H3* and MOSFET BRIDGE six supply transistors as function of θ_e rotor rotational electrical angle

Hall	$0 < \theta_e < 60°$	$60° < \theta_e < 120°$	$120° < \theta_e < 180°$
H1	1	0	0
H2	0	0	1
H3	1	1	1
Hall	$180 < \theta_e < 240°$	$240° < \theta_e < 300°$	$300° < \theta_e < 360°$
H1	0	1	1
H2	1	1	0
H3	0	0	0

Mosfet	$0 < \theta_e < 60°$	$60° < \theta_e < 120°$	$120° < \theta_e < 180°$
S1	0	0	0
S2	0	1	1
S3	1	1	0
S4	0	0	0
S5	0	0	1
S6	1	0	0
Mosfet	$180 < \theta_e < 240°$	$240° < \theta_e < 300°$	$300° < \theta_e < 360°$
S1	0	1	1
S2	0	0	0
S3	0	0	0
S4	1	1	0
S5	1	0	0
S6	0	0	1

The decoder controller applies the switching sequence based on Hall sensor input by activating transistors supply grid. In general, in each time instant, only two winding phases are powered reducing to 2/3 the number of active coils while 1/3 are deactivated and available to reduce their temperature by the motor cooling thermal system. The BLDC motor mechanical torque is developed by the interaction between the rotating magnetic field generated by stator winding coils and the magnetic field generated by rotor permanent magnets. On the rotor is applied external aerodynamic hinge torque, considering gearbox contribute to the mechanical transmission for what concerning friction forces resultant on rotor motion. In general, Torque is a function of the vectorial resultant for induction magnetic field provided by all three phases on rotor poles, controlled by commutation logic activating the proper phase to keep stator fields as close to possible to rotor field. The intensity of the torque is proportional to supply currents circulating within the activated coils, the number coils and transversal area on the rotor surface for each stator phase, and the permanent magnetic flux density of the rotor.

The maximum allowed current for BLDC motor is limited by overheating conditions and level of external load that causes thermal fatigue on coils insulation due to Joule effects improving short coils failure probability. On the other point of view an increasing number of winding coils is associated with motor weight and volume, two main important parameters for an aircraft actuator design. The physical properties of materials as Boron Neodymium alloy, which presents the best performances, are associated with limited magnetic flux density generated by a known permanent magnet.

The currents circulating within stator coils, and the equivalent motor torque, are strongly influenced by interaction with the rotor magnetic field, which during rotation induces magnetic flux variation, according to Faraday's law, in stator coils generating a f_{cem} (counterelectromotive force) proportional to rotor speed. In a first approximation, torque is a linear function of rotor speed by imposing Kt proportional constant between T torque and I phase current, equal to K_T proportional constant between f_{cem} and rotor speed ω_r. The f_{cem} is a voltage contribution in the opposite sign to phase voltage generated by circulating phase currents multiplied with R coil resistance.

$$f_{cem} = K_T \omega_r \tag{2.2}$$

$$V_{stator} = I\,R - K_T \omega_r \tag{2.3}$$

$$T = K_T I = \frac{V K_T}{R} - \frac{K_T^2}{R}\,\omega_r \tag{2.4}$$

2.1.3 Motor Regulation System

The BLDC output mechanical power is composed of two main terms: torque and rotor speed; the motor torque is a function of phase current and external load. Therefore to regulate motor output power is more efficient to design a speed control system considering that the phase commutation logic is based on rotor angular position measurement. Rotor angular speed is a function of phase applied voltage amplitude, as reported in fig. 1.6 on page 14 the control circuit is connected to HVDC at constant 270VDC, therefore it's possible to drive voltage managing motor output power.

There are different solutions to drive voltage on the BLDC regulation system, the employing of the variable resistor as a potentiometer control voltage, is a low-efficiency solution by dissipating power by Joule effect, not requested by different operating conditions. A more efficient solution to regulate BLDC motor output power by driving phase voltage is a PWM [57] pulse with modulation system logic, which offers precise control over motor speed and torque modifying variable duty cycle to modulate voltage pulses toward decoder circuit. There are three control schemes for electronic commutation: trapezoidal, sinusoidal and Field Oriented Control (FOC), but sinusoidal and FOC are too expensive to implement and is reserved for high-end applications and are not discussed.

Trapezoidal control is used in the model-based BLDC motor, it has a downside related to torque ripple due to stepped trapezoidal commutation especially at low speed. The motor speed is calculated by derivation of rotor position measurement in time by hall sensor, and a control system compares both position and speed with the pilot command calculating the error managed by a PID control system to drive PWM duty cycle modulation to the command.

Different fault types on BLDC control system can cause irreversible damage to the actuator, they can be prevented by on-board control system prevention logic that overrides the normal motor controls to preserve the system. The currents overheating is one of these fault types, it may occur when external load get stuck the rotor in a fixed position for a long time, the counter electromotive forces drop and the active phase currents growth over security level. The overheating could damage coils insulation and demagnetize rotor permanent magnets, which for example in NdFeB alloy have a Curie point at 80° inducing a sudden velocity reversal. In fast transient during startup motion from zero velocity to a commanded position, phase current could overcome maximum peak current suddenly recovery by PWM protection logic. In the same way, the PWM control system prevents the crossing of maximum working current during normal operations.

The onboard system control, prevention logic could detect faulty hall sensors, since only one combination of sensors output is allowed by the rotor geometry so when the sensors don't work correctly a not compliance signal pattern will be generated and recognized.

2.2 EMA Reference Model

The numerical model, for EMA electromechanical actuator, can simulate with adequate degree of confidence and high detail level, the physical behaviour for an electromechanical actuator under different boundary conditions described in 3.1 at page 53. The EMA numerical model is developed in *MatLab Simulink®*, and could be represented at high detail level by figure 2.6 on page 28 in five main simulation blocks, suggested by [53], representative of physical EMA component or an external input to the system:

1. **COM**: pilot command simulation for flight control surface;
2. **ACE**: actuator control electronics;
3. **BLDC Motor**: PWM power electronic system and electromagnetic BLDC model;
4. **TR**: external load acting on aerodynamic surfaces;
5. **EMA Dynamic Model**:mechanical dynamic model for transmission lines from the motor to user (aerodynamic surface);

The reference model robustness allows simulating different types of the electromagnetic actuator with different technical specifications. The technical parameters, used in the proposed work, are referred to a specific brushless DC Servomotor model 4490H048BS whose model specifications are collected in table A.1 on page 144, from supplier technical brochure in appendix A on page 141. All the simulation parameters are filled in a *Matlab* script input file to be launched before starting *Simulink* simulation. The input file contains also some technical parameters, necessary to define simulation parameters as friction coefficients, cinematic backlashes, PID coefficients and so more. The integration method, used for convergence, is a first order Runge Kutta equivalent for Euler's method, referred to a fixed time step equal to $10^{-}6\ s$ two order of magnitudes below the smallest time system characteristic as described in [26] and [27]. The fixed time step integration methods require only one evaluation function every time step compared to the variable time step integration method concerning the recursive evaluation of the error function. The choice of the first order *"Runge Kutta"* is a compromise between performance on numerical convergence and stability since the proposed reference model is complex and costing a large computational effort, indeed a single simulation second needs four minutes to get results.

2.2.1 COM Block

The *COM* block is able to simulate command signals, coming from SAS stability augmentation system, it processes the pilot command integrating in real time the pilot command and other flight parameters calculated or acquired by sensors aircraft. Several options are available as indicated in fig. 2.7, and are possible to make combinations by selecting more than one command type, the specific command parameters can be

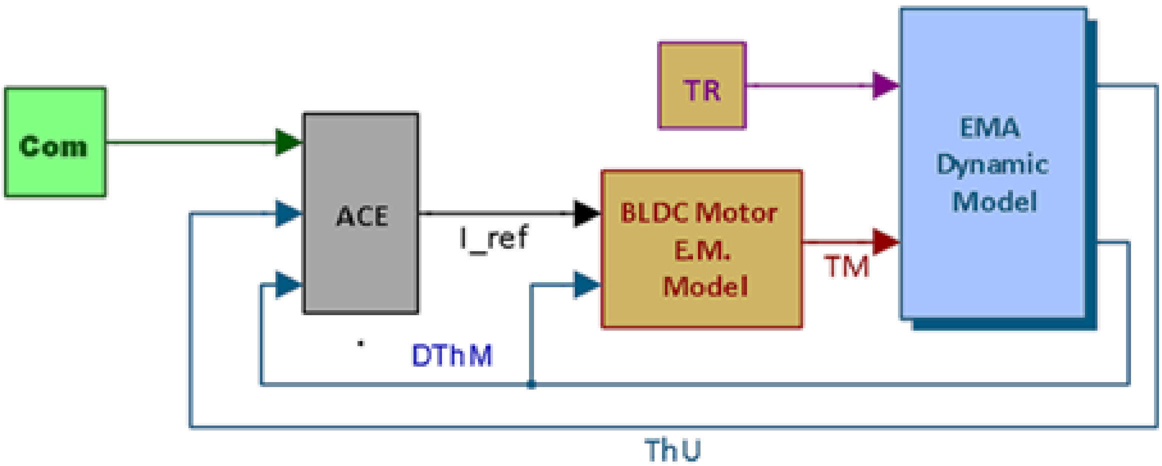

Figure 2.6: Reference Model for EMA Electro-Mechanical Actuator

updated directly from Simulink GUI graphical user interface or through variables within *Matlab* input file. The *COM* generates an input signals in time representing system forcing, the output EMA model is a function of both types forcing signals and technical simulation parameters, including the parametrization of the progressive failure types described in 2.3 on page 36. The AC oscillating command signals: SINE and Linear Chirp are used to better evaluate the dynamics behaviour of simulation output on the aerodynamic surface in terms of FRF frequency response function comparing system input and output amplitude, frequency, and phase.

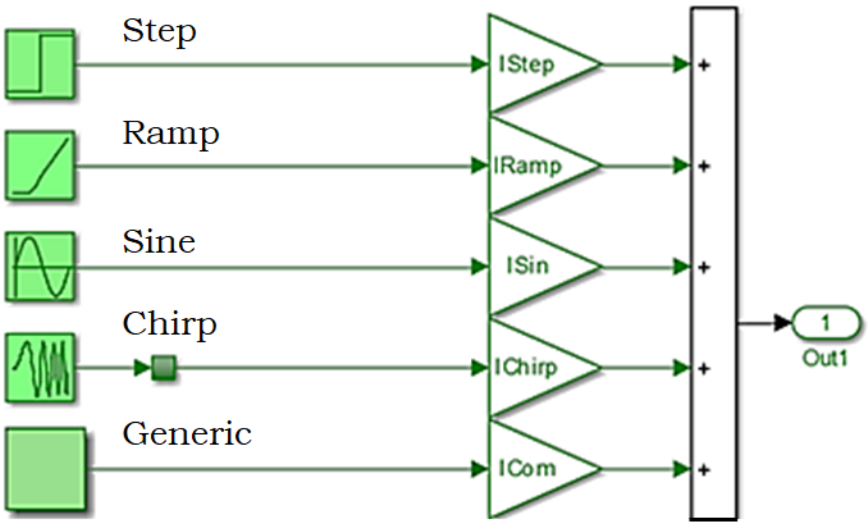

Figure 2.7: Command options available as an input of EMA Reference Model

2.2.2 ACE Actuator Control Electronics

This simulation block implements numerical calculation of I_{ref} reference current, a variable quantity expressed in $[A]$ Ampere useful only for control algorithms without physical relation with real phase currents circulating within motor coils. The input parameters are ThU user rotation angle, Com position commanded by SAS, and $DThM$ rotor speed used as the speed and position control system for aerospace application as in [80]. The algorithm calculates position error between the actual rotor position and the commanded one, calculating W_{ref} reference velocity by proportional constant, a motor design parameter. This reference velocity is compared with the rotor speed $DThM$ to calculate speed error the input variable for the *PID* controller. The *PID* controller, used in different technical solution as [9] and [29], calculates TM_{ref} reference torque, but to avoid the effect of noise and ripple on feedback signals derivative constant is fixed to zero. The reference torque is divided for K_t defined as proportional constant representing linear relationship function between torque and current, an important design parameter specific for each BLDC motor configuration.

In this simulation block two reference limiters are integrated to avoid over-speed, applied to reference velocity, and overcurrent, applied on reference current during normal operations. The reference current, in low power conditions, is affected by white noise disturbance so a band-limited white noise function is added to the calculated signal to improve simulation accuracy. The algorithm calculates position error, between

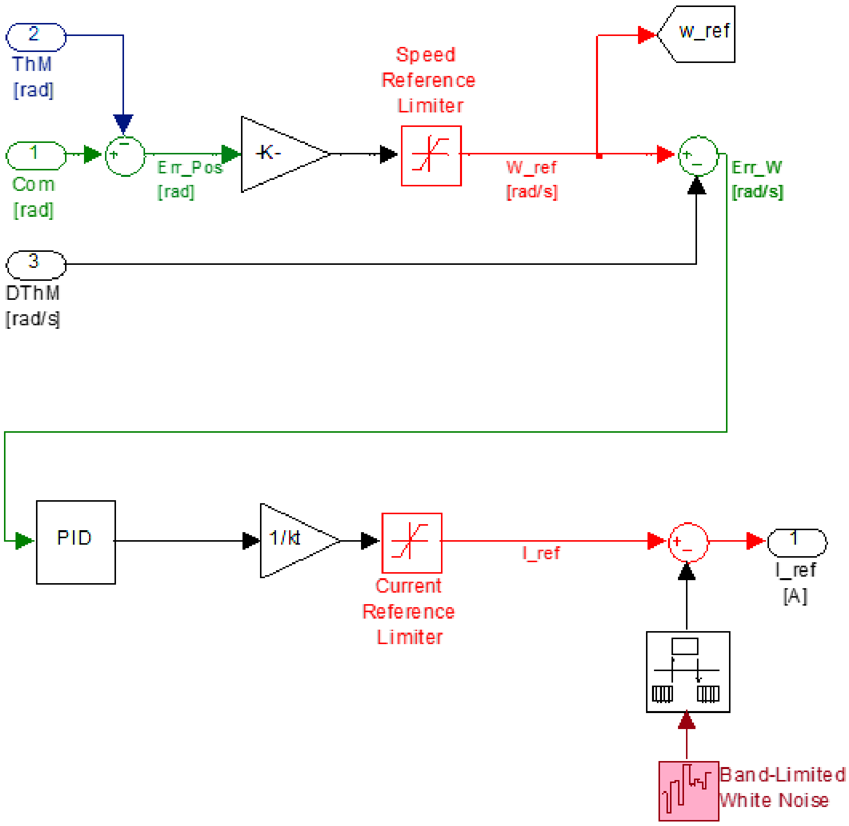

Figure 2.8: ACE Actuator Control Electronics

the actual rotor position and the commanded one, calculating W_{ref} reference velocity by proportional constant, a motor design parameter. The *PID* controller [9], calculate TM_{ref} reference torque, but to avoid the effect of noise and ripple on feedback signals Derivative constant is fixed to zero. This reference velocity is compared with the rotor speed $DthM$ to calculate speed error the input variable for the *PID* controller. The reference torque is divided for a K_t a proportional constant that represents the linear function between torque and current, an important design parameter specific for each BLDC motor configuration.

In this simulation block two reference limiters are integrated to avoid over-speed, applied to reference velocity, and over-current applied on reference current during normal operations. The reference current in low power conditions is affected by white noise disturbance so a band-limited white noise function is added to the calculated signal to improve simulation accuracy.

2.2.3 BLDC Electromechanical Model Block

The electromechanical model block is one of the most complex simulation blocks within EMA reference model, it is composed of six subsystems able to simulate power electronics behaviour and electromagnetic coupling between stator and rotor. The whole simulation block calculates as output the filtered phase currents I_a, I_b, I_c, supplying the phase winding coils and mechanical motor torque T_m by two parallel numerical streams as indicated in fig. 2.9 on page 32. The first numerical stream is represented by the following subsystems connected in series:

- Reference Current calculation;
- PWM;
- Inverter MOSFET H bridge transistors;

The second stream is dedicated to Motor Torque elaboration block by normalized Counter Electro Motive Force (CEMF), as input both phase currents and torque calculation and is it composed by following subsystems:

- ”Back CEMF phase”;
- ”Ei_n normalized CEMF”;
- ”Motor Torque computation”;

Reference current: The inputs of this subsystem are θ_r angular rotor position, split into three lookup tables, and I_{ref} reference current. Each setup table returns +1 when the related phase is powered with a polarity, -1 when the polarity is reversed and 0 otherwise. At each time instant one phase will be powered at $+1$ another at -1 and the last at zero, therefore the algorithm is able to simulate the commutation logic of a three-phase trapezoidal BLDC motor as in fig. 2.10.

PWM Pulse Width Modulation: each reference phase currents is compared with phase currents feedback signals (I_a, I_b, I_c) through a hysteresis block considering for each hysteresis block a reference dead band around the origin. The comparison evaluation returns the value 1 if the input is greater than $+hb$ positive half dead band, 0 if it is less than a $-hb$ negative half dead band. Until the input comparison input falls into hysteresis dead band the output keeps its previous state. The output is essentially a Boolean output not a physical quantity as a function of

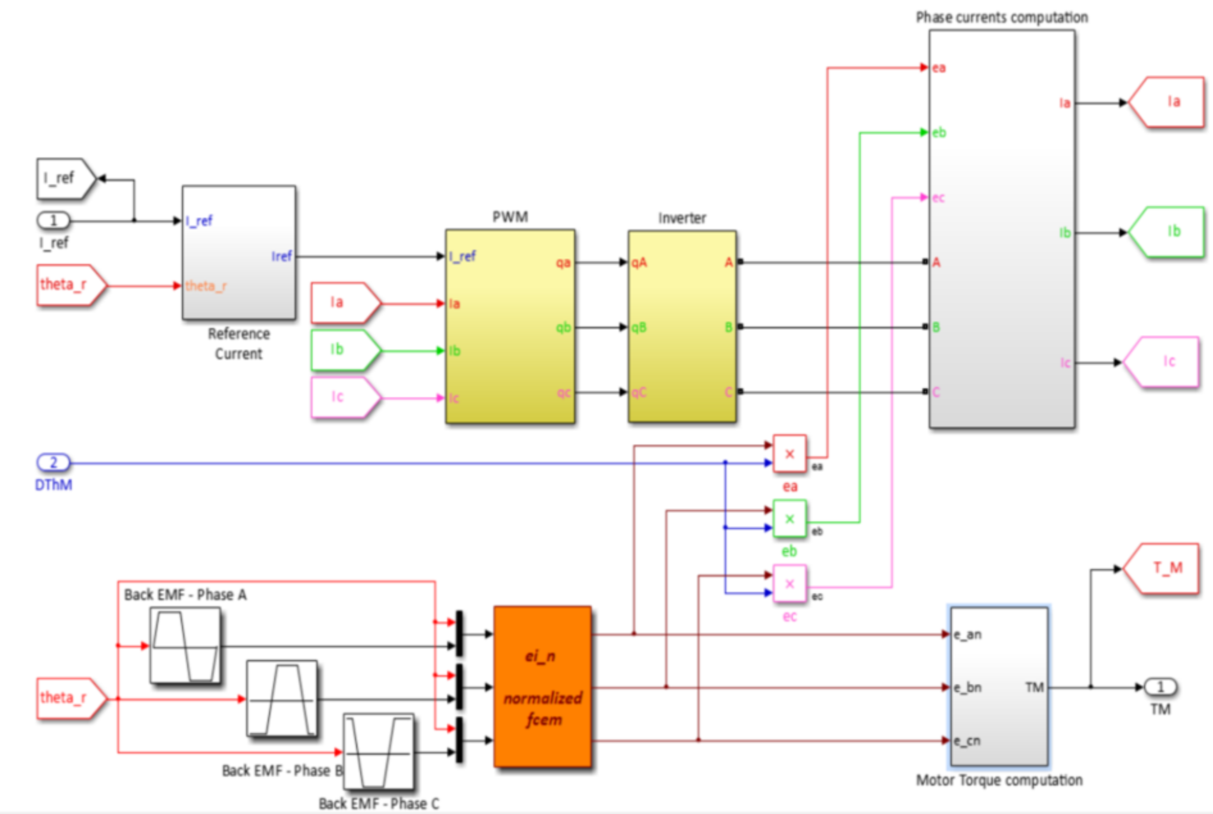

Figure 2.9: BLDC MOTOR simulation block details

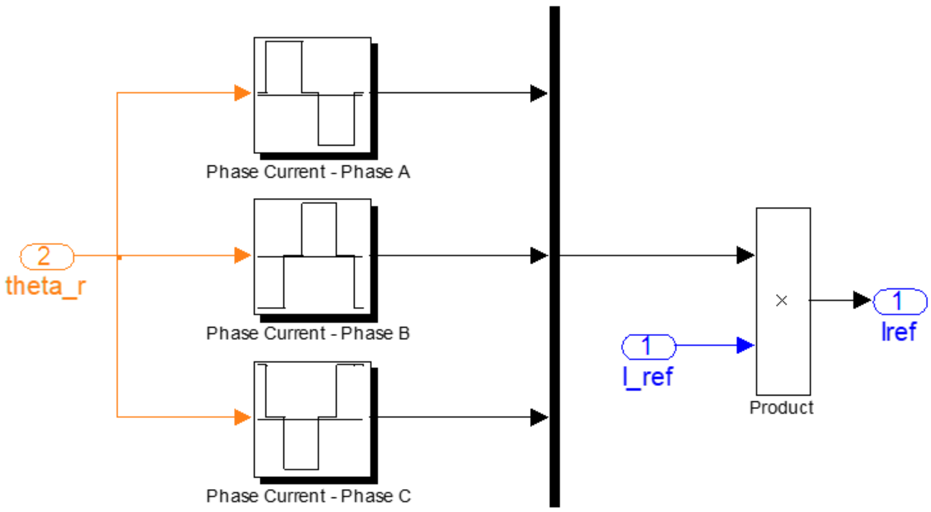

Figure 2.10: Reference Current Subsystem

dead bandwidth from which is defined as the PWM carrier frequency. The PWM carrier frequency for Nyquist Shannon theorem could be at least one order greater than phase switching frequency at 10KHz bandwidth avoiding aliasing problems.

The inverter: this subsystem simulates, as reported in Fig. 7, the H bridge transistor power supply by *"Universal Bridge" Simulink* ® block from *Simscape*® library. The universal bridge is connected to HVDC supply at $270V\,DC$, each Boolean PWM signals (q_a, q_b, q_c), and their logical negation NOT ,activate one of the six *MOSFET* power transistors of the H bridge supplying the three-phase winding coils. When a power transistor is connected to supply one phase the corresponding connection to the ground is off avoiding short circuit phase to ground inside the bridge configuration, that should stop the brushlike motor. All the supply phases connected to the *H* bridge are the output of this subsystem (A, B, C).

Normalized CEMF: The system simulates the normalized counter electromotive force for each phase by input the θ_m rotor angular position. The normalized counter electromotive forces multiplied by $\dot{\theta}_m$ rotor speed gives the actual counter electromotive force needed to evaluate the actual phase currents. The electromagnetic coupling constant K_{fcem} is equivalent to the normalized counter electromotive force $CEMF_{norm}$ as indicated in the following equation:

$$CEMF_{norm} = \frac{CEMF}{\omega_m} = K_{fcem} \tag{2.5}$$

The effect of *RSE* rotor static eccentricity affects the electromagnetic coupling constant as a function of rotor angular position θ_m.

$$K^i_{fcem} = K^i_e(\theta_m) \cdot \left(1 + \zeta \cos\left(\theta_m + \frac{(i-1)^2}{3}\pi\right)\right) \tag{2.6}$$

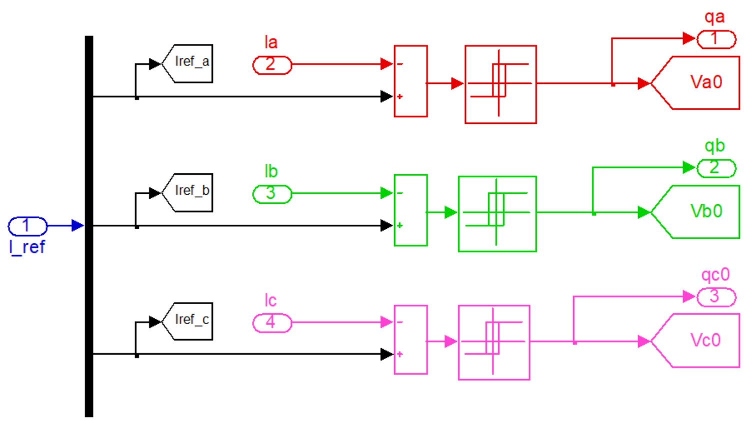

Figure 2.11: PWM Pulse Width Modulation, commutation logic subsystem

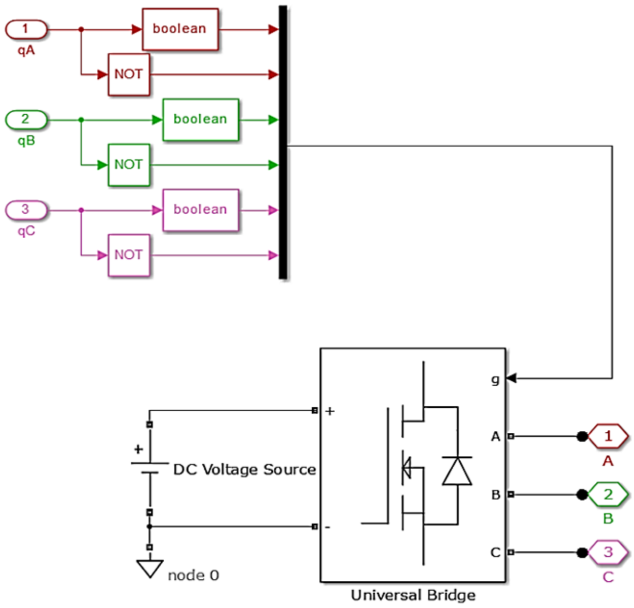

Figure 2.12: Inverter subsystem with Universal H Bridge of 6 MOSFET power transistor

Where, as indicated in [10], $K_e^i(\theta_m))$ is the trapezoidal wave shape of the normalized counter electromotive force of the i-th phase evaluate by lookup table indicated in fig. 2.13, and ζ is a-dimensional RSE evaluated as the ratio between rotor eccentricity and the nominal air gap between rotor and stator.

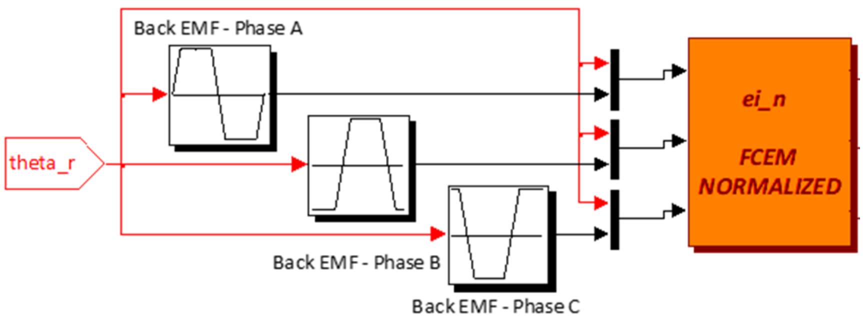

Figure 2.13: BLDC motor Normalized CEMF

Phase Currents computation: The three-phase voltages elaborated from Inverter subsystem and the three counter electromotive forces from Normalized CEMF subsystem is the input of thr Phase current computation subsystem achieved by *Simscape* ® *toolbox*. The stator coils are configured in balanced star three phase connection as described in 2.1.1, as inductive-resistive electrical features

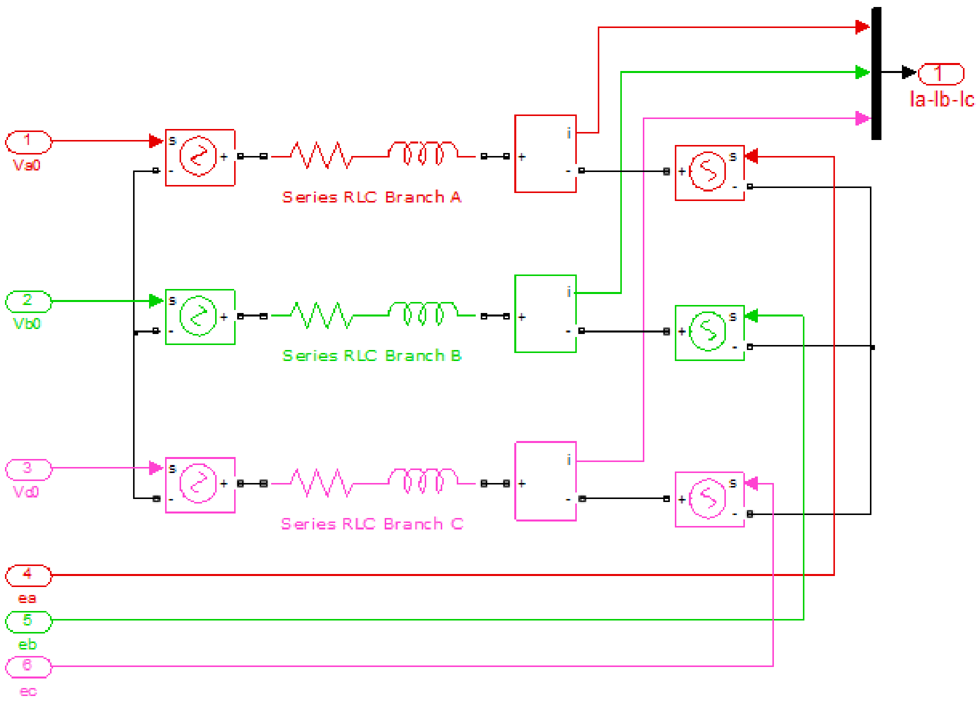

Figure 2.14: Phase Currents Computation subsystem

connected in series to a counter electromotive generator placed between the phase voltage and the star node. The elaborated phase currents are used as current feedback signals for the PWM logic subsystem and as output for the motor torque evaluation as indicated in 2.14 Phase Currents Computation subsystem. The actual phase currents are filtered by low pass filter provide a smoother form of a signal, removing the short-term fluctuations and leaving the longer-term trend.

Motor Torque Computation: each supply phase gives a contribution to generating resultant motor torque which is limited by TMM maximum torque motor prevention limit, considering the saturation magnetic field in the stator steel core. The subsystem inputs are both filtered phase currents and normalized counter electromotive forces.

2.2.4 EMA Dynamic Model Block

The electromechanical model control subsystem elaborates phase currents and TM motor torque, TR represents external load referred to hinge torque acting on the aerodynamic surface (called user), considering also mechanical efficiency of the gearbox and all rolling and coulomb friction along the transmission line up to rotor actuator. The mechanical assembly of motor, gearbox, transmission

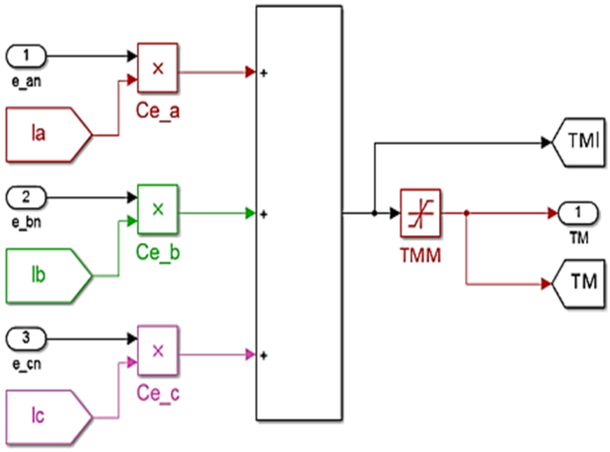

Figure 2.15: Motor Torque Computation subsystem with TMM torque limiter

line, surface is overall simulated by a second-order model with one degree of freedom considering inertial and viscous effects and several non-linearity. The non-linearity considered within the presented model are several as the end of travels, compliance and backlash acting on gearbox and balls screw jack [25], Analogical To Digital Conversion (ADC) of the feedback signals electrical noise and offset of the position transducers [17], and friction phenomena acting on bearings gears hinges and screw [19]and [16] . The model, in fig. 2.16 on 37 estimates the ThU actual angular position user by accounting for backlash and gearbox transmission ratio, the fast shaft is considered the BLDC rotor shaft and the low shaft is the output gearbox shaft connected to the ball screw jack mechanism. The electric angle θ_e is calculated as indicated in (2.1) from ThU user angle position. The subsystem in fig 2.24 on page 50 is related to Borello friction model.

2.3 EMA Failures and Model Integration

2.3.1 EMA Failures Motor Statistics

In the recent electric literature only two extensive investigations on engine failures are available: the first was carried out in 1985 by *EPRI* (Electric Power Research Institute) on about 5000 engines employed in different applications and in various industrial fields in the USA; the second survey is dated 1995, it is limited to companies in the oil sector in Norway. It's evident that the first investigation considers a wider range of applications supplied both in AC and DC voltage major of 1000 V with installed power major than 150 kW whereas the second survey includes only asynchronous with AC voltage minor than 1000 $V\,AC$ normally used for low power major than 10 kW. As a consequence of this different acquisition failure database in terms of installed power and voltage type and range, the results are partially different, it's noticed that the second survey engines are almost located outside on cold environment.

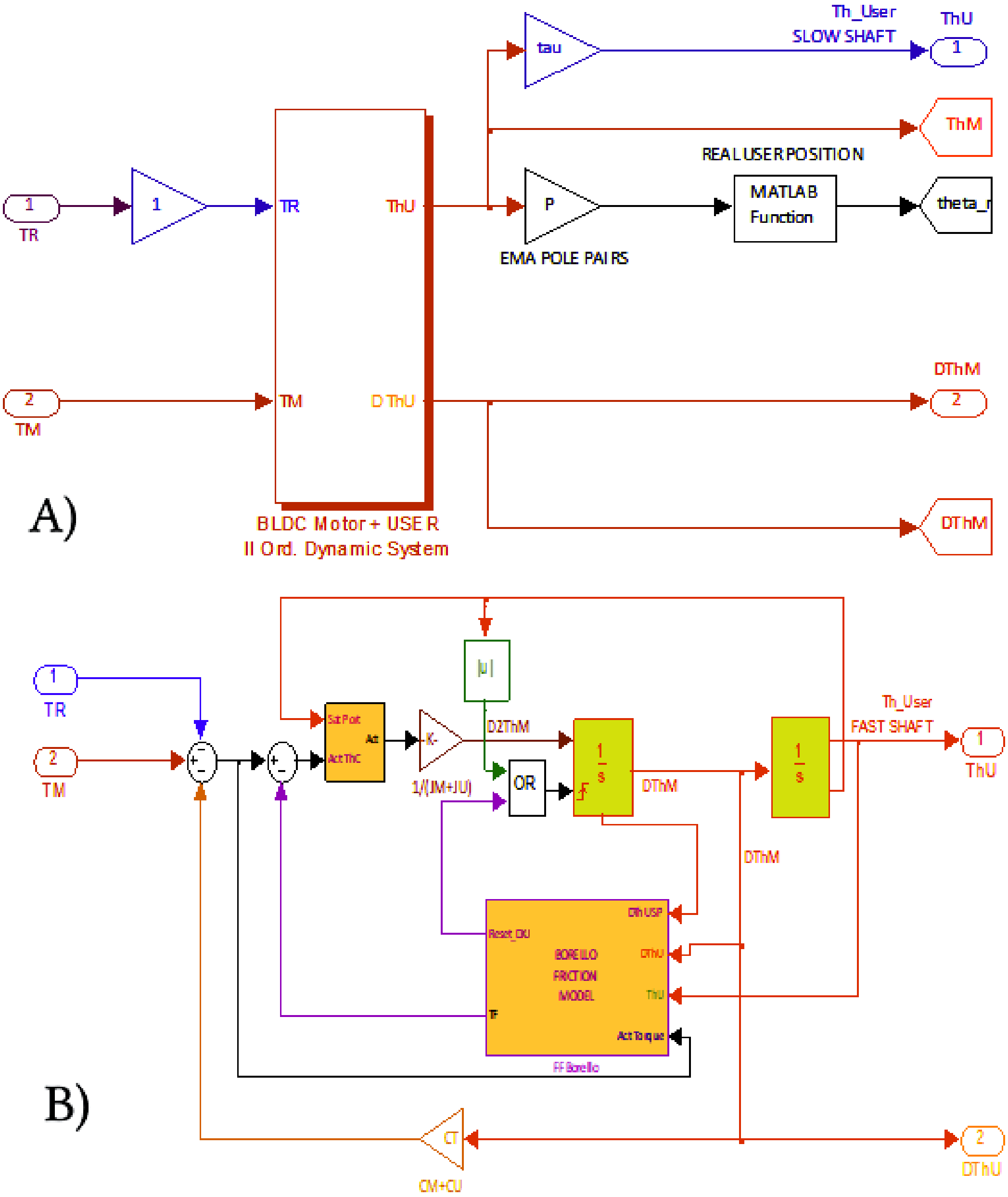

Figure 2.16: A) BLDC MOTOR + User dynamic model subsystem B) Second order dynamic subsystem with Borello Friction Model

In the first survey on EMA faults, bearing and stator faults are respectively the 41% and 37% among all motors interested in the investigation. Analyzing the stator faults type the 23% is due to ground insulation related to thermal fatigue phenomena.

In the 1995 survey, the followed-up motors were 2596 subdivided into different power categories of study, the considered aeronautical interesting category able to satisfy the requirements for primary flight control systems is the low power supply 11 kW that represents the 57.94 % of the followed-up motors.

The statistics report also in this second survey that the bearings damages are the majority of the failures with 51.07% of the total recorded failure amounts, followed by the stator windings failures with 15.76%. The evaluation of starting causes for these two main failures categories, reports that bearing failures are due to mechanical faults, overheating, enduring overload, high vibration referred to wear phenomena as pitting.

The winding stator faults are caused by thermal balance problems, mechanical damages (unbalancing rotor, misalignments), insulation ageing for the coils. The failures event frequency is considerably dependent by specific operating conditions for the electrical motor. The statistics data reveals that outside environment, as the altitude conditions on aircraft flight, structure vibration referred to aeroelastic wing behaviour, influence the fault event frequency growing 2.5 times than indoor application without external vibrational sources.

Another incident example of fault event frequency for Rotor failures under operating conditions is represented by applications requiring start and stop motion under high load. This is the typical operating conditions on which aerodynamic surfaces of primary flight control system operates eespecially in fights military aircraft. Monitoring and diagnostics are based on acquisition and elaboration of some signals called *"prognostic precursors"* including symptoms information about incipient failures or progressive degradation paths.

2.3.2 FDI Fault Detection and Identification

As above-mentioned indicated in 1 on page 5, monitoring and identification techniques are based on selecting in complex aircraft system the appropriate prognostic precursors, acquired by sensor framework. The sensor framework, in aerospace environment for monitoring flight control systems, must satisfy strict requirements by control flight certification authority. In general, a reliable sensor framework for *FDI* purposes should not be invasive avoiding measurement influence, with technical features to allow an accurate measurement useful of the precursor's variables for the prognostic algorithms. If the system requirements and *FDI* general guidelines will be compliance by sensor framework, the integration between model-based *FDI* algorithms and data-driven behaviours, it should be more effective in reducing differences and improving the added value to presented model-based approach on safety-critical systems.

On the other point of view is several EMA aerospace applications it's very difficult to quantify a right estimation of the RUL remaining useful Life, without complex statistical methods and reliable faults operational data not jet enough structured. The FDI model-based approach satisfying could consider different concurrent physical aspects they may interact as reported in fig. 2.17, where different interaction generates different failures types. The Mechanical and Structural phenomena are a major concern for EMA aeronautical operations affecting motion transmission lines from EMA rotor to aerodynamic surface. The causes are several, such as environmental conditions, lubrication issues, manufacturing defects, with difficulty able to determine during the design process. The EMA operates at a very high rotational speed, with rotor dynamic issues related to vibrations, bearings wear and fatigue and especially for BLDC motors with permanent magnets the magnets junction integrity for centrifugal forces. The Electrical and Electronics phenomena are not less concern in EMA health state, eespecially for what concerning thermal balance issues among overheating and overcurrents events, generating safety-critical consequences. The proposed model-based FDI approach considers an EMA for actuation purposes taking into account a mechanism complexity with fault non-linearity phenomena as wear, increasing friction on mechanical transmission and thermal fatigue on insulations.

2.3.3 RSE Rotor Static Eccentricity

The main components of the BLDC motor are stator and rotor, the rotor is connected to the mechanical transmission line. In the application of BLDC motor as EMA on the primary flight control system, the rotor shaft is considered *"rigid"* as design parameter

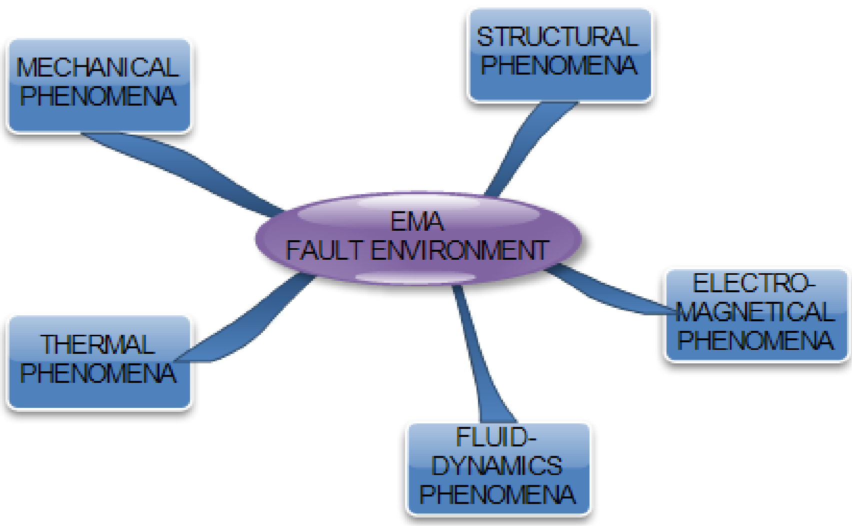

Figure 2.17: Different physical aspects interacting in concurrent mode to define the EMA operating environment with progressive incipients faults

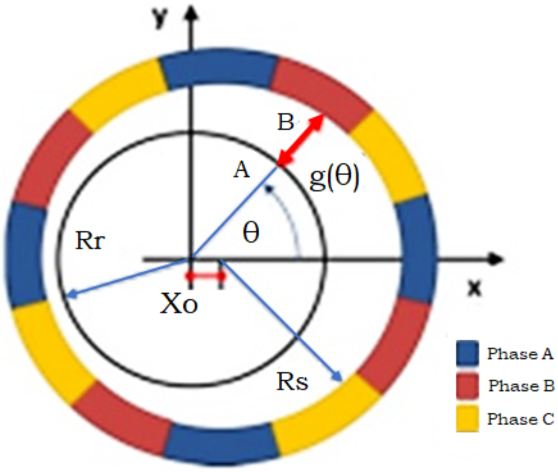

Figure 2.18: Schematic of BLDC Motor geometrical reference system in Rotor Static Eccentricity in faulty condition

a rigid shaft mounted on roller ball bearing. The rotor static Eccentricity is within the mechanical and structural failures, the failure phenomena may occur, as reported in fig. 2.18, when rotor turns around its own axis but the rotor axis line is different than the stator axis. Important study boundary conditions are referred to some important rotor dynamic assumptions:

- The rotor mass is symmetric compared to the rotor shaft axis;
- The rotor turns without static or dynamic unbalance or mechanical looseness for mechanical connecting elements;

These are a very important assumption, for the model-based approach because under rotational speed the inertial forces could deform the rotor axis as a linear combination of its dynamic mode shapes. Indeed, when the rotor speed is near to one of own resonant frequencies $f_r = \omega_r/2\pi$ (or pulses ω_r), the rotor configuration is near to this mode shape modifying the static eccentricity configuration. Therefore, in the considered study case, the rotor axis deformability could be neglected, considering rotor perfectly stiff, and angular speed is far from the half value of first own resonance pulse ω_0. Under rotor perfectly stiff hypothesis, the unbalance is not a function of rotational speed, adding to this the perfect rotor masses symmetry around the rotational axis, from the initial condition for the rotor static eccentricity, it could only growth in the same direction, respect to the rotor reference system, underwear effect on mechanical supports. The rotor static eccentricity is due to misalignment and manufacturing tolerances, combined with progressive rolling bearing wear during operational life cycles. The faulty condition is geometrically described by eccentric positioning between the circumferences described by rotor radius R_r and stator radius R_s:

$$x^2 + y^2 = R_r^2 \tag{2.7}$$

$$(x - x_0^2)^2 + y^2 = R_s^2 \tag{2.8}$$

Expressed in polar coordinate:

$$\rho = R_r \rho^2 - 2\rho x_0 cos\theta + x_0^2 - R_s^2 = 0 \tag{2.9}$$

The air-gap non-symmetrical distribution, expressed as $g(\theta)$, a difference between two-point A and B on a generic straight line, in correspondence respectively on rotor and stator circumferences, from the origin of reference coordinates, placed on geometric stator centre. In the equation (2.10) the air gap is approximated by a sinusoidal function where g_0 is the reference air gap in a healthy condition:

$$g(\theta) = x_0 cos\theta + R_s \sqrt{1 - \left(\frac{x_0}{Rs}\right)^2 \sin^2\theta} - R_r \tag{2.10}$$

$$g(\theta) \cong x_0 cos\theta + R_s \left[1 - \frac{1}{2}\left(\frac{x_0}{R_s}\right)^2 \sin^2\theta\right] - R_r \tag{2.11}$$

$$g(\theta) \cong x_0 cos\theta + g_0 \tag{2.12}$$

$$g(\theta) \cong g_0(1 + \zeta\cos(\theta)) \;\; where \; \zeta = \frac{x_0}{g_0} \tag{2.13}$$

The geometrical asymmetry takes effect on magnetic flux only if a number of permanents magnets pair poles P_p is over one. In healthy condition, without rotor static eccentricity, considering the mechanical angle $0 \leq \theta \leq 2\pi$ and the electrical angle $\theta_E = \theta \bullet P_p$, the polar step $\tau_E = \pi/P_p$, the magnetic flux lines on generic angle θ_1, as indicated in fig 2.19 crossing the air-gap closing loop at $\theta_1 + \pi/2$ in case of two pair poles rotor configuration. Given the geometry of rotor and stator configuration, the induction magnetic field is a function of the following parameters expressed in eq. (2.14) in a faulty condition referred to generic angular position θ_1:

- F_m: Magneto-motive force generating from rotor permanent magnets;
- S: crossing surface for magnetic flux;
- $g(\theta)$: the air-gap distance between rotor and stator surfaces;

$$\Phi = \frac{F_m}{R_1 + R_2} = \frac{F_m}{\frac{g(\theta_1)}{\mu_0 S} + \frac{g(\theta_1 + \frac{\pi}{2})}{\mu_0 S}} = \frac{F_m \mu_0 S}{g(\theta_1) + g(\theta_1 + \frac{\pi}{2})} \tag{2.14}$$

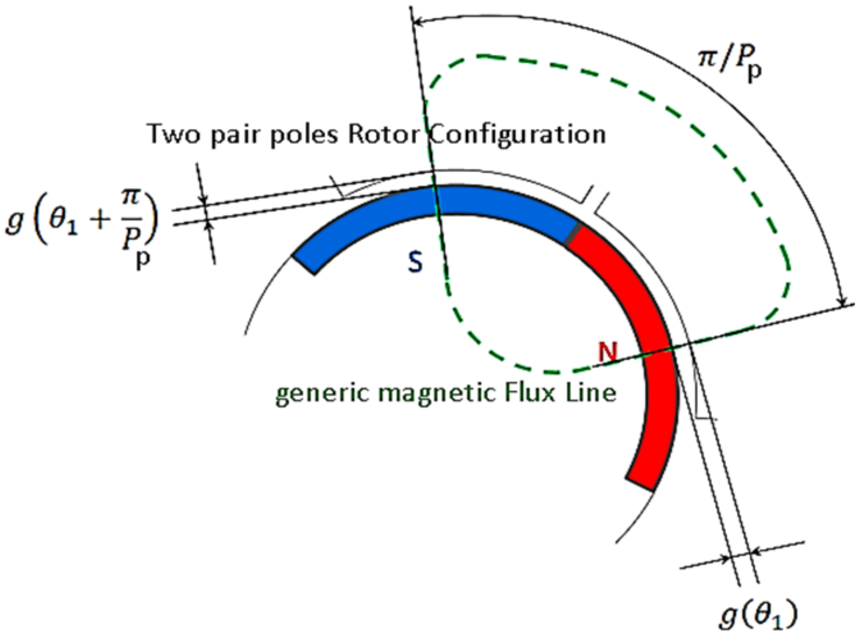

Figure 2.19: Qualitative Geometry to evaluate magnetic flux configuration crossing air gap between Rotor an Stator

If the (2.14) is integrated with (2.13) it's possible to achieve formulation expressed in (2.15) following indicated:

$$\Phi = \frac{F_m \mu_0 S}{g_0 + x_0 \cos(\theta_1) + g_0 + x_0 \cos(\theta_1 + \frac{\pi}{2})} = \frac{F_m \mu_0 S}{2g_0 + x_0(\cos(\theta_1) + \sin(\theta_1))} \tag{2.15}$$

In generic healthy condition without rotor static eccentricity the corresponding magnetic flux Φ_0 is defined as a function of $\mathfrak{R}$ the reluctance of the magnetic circuit:

$$\Phi_0 = \frac{F_m}{\mathfrak{R}} = \frac{F_m \cdot \mu_0 \cdot S}{2g_0} \tag{2.16}$$

Following the (2.16) and (2.14) imposing Pp=1 in the faulty condition is not possible to distinguish Φ form ϕ_0 because if the magnetic flux derivative is equivalent to counter electromotive force constant therefore is valid the following condition:

$$2g_0 = g(\theta_1) + g(\theta_1 + \pi) \tag{2.17}$$

The implementation within the reference model described in paragraph *"Normalized CEMF"* on page 33 simulation block, is performed by modulating the counter electromotive force coefficients $k_{fcem}^{(i)}$ expressed as function of static eccentricity parameter ζ for the (i) supply phase (where i=1 indicating I_a, i=2 indicating I_b, and i=3 equivalent

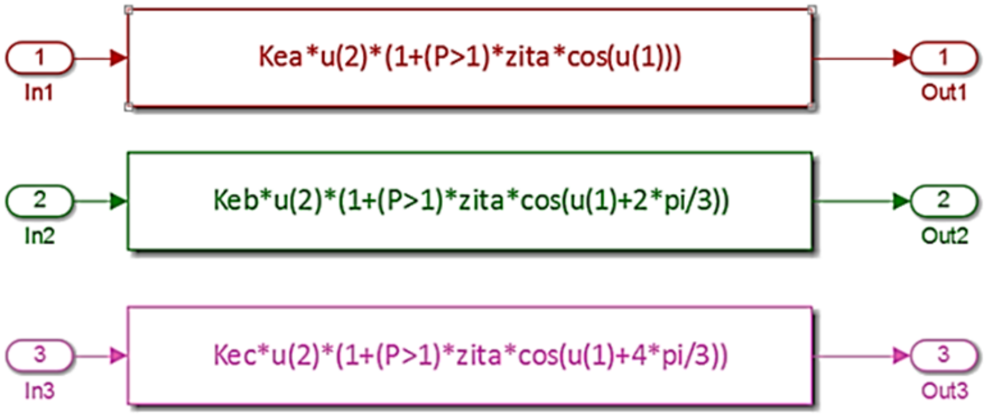

Figure 2.20: Simulink Model Block in Reference Model, representing the modulation for counter electromotive force coefficients, for each current phase to model the effects on the model of rotor static eccentricity fault

to I_c). Other mandatory variables are the angular mechanical position θ_m, where the trapezoidal shaped coefficients in healthy condition are expressed within normalized $fcem$ coefficients $k_e^{(i)}(\theta_m)$, evaluating by lookup tables, expressed in the relation (2.6). The counter electromotive coefficients modulation allows reproducing with accuracy based on analytical representation the interaction between the rotating magnetic stator field driving the magnetic field of permanent rotor magnets avoiding to run complex and heavy computation Finite Element Methods (FEM) as indicated in [58]. The air-gap in rotor static eccentricity varies its width over the rotor revolution, with a fixed direction of minimum airgap on the fixed stator reference system. The RSE disturbance, affecting the magnetic coupling between rotor and stator magnets, is evident on Torque gain and counter electromotive force becoming a function of the angular position related to different $\Re$ reluctance associated with the equivalent magnetic circuit.

2.3.4 RDE Rotor Dynamic Eccentricity

The RDE is an evolution of the rotor static eccentric failure, classified within the mechanical and structural failures, this failure phenomenon may occur, as reported in fig.2.21, when the rotor turns around its own axis but the rotor axis centre Cr rotates around the stator centre mass centre Cs with a rotational speed Ω. In this failure mode, the rotor dynamic assumptions are not still valid, as defined in the previous paragraph for the RSE. It's only considered the assumption of avoiding the radial air-gap changes between rotor and stator due to elastic shaft deformations referred to dynamic behaviours. In this failure the minimum air gap direction is not constant, related to a stator reference system coordinates, but it rotates with speed Ω around stator mass centre Cs. The Cr

rotational speed, in the simulation framework, is placed at 44% of the rotor speed around its rotational axis, considering this assumption as related to the bearing cage rotational speed, for ball radial bearing on which coupled rotor shaft. The mathematical model is

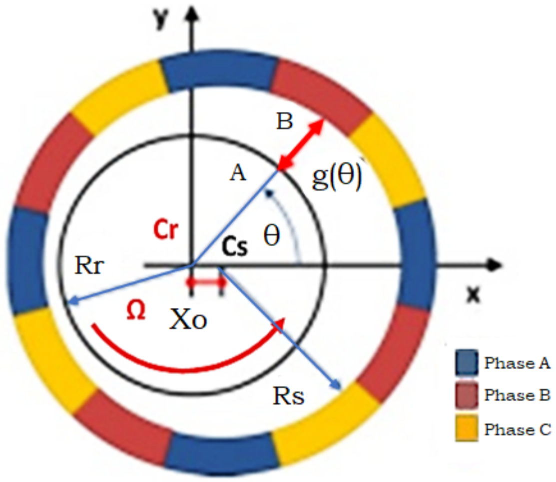

Figure 2.21: Schematic of BLDC Motor geometrical reference system in Rotor Dynamic Eccentricity in faulty condition

expressed by (2.18) as the evolution of (2.13) where the minimum air gap position is a function of Cr rotational speed Ω.

$$g(\theta) = g_0(1 + \zeta cos\Big(\frac{(i-1)2}{3}\pi - \Omega t\Big) \;\; where \; \zeta = \frac{x_0}{g_0} \tag{2.18}$$

The induction magnetic field equations as (2.14) and (2.15), changes by substituting the air gap formulation with (2.18), therefore the rotor dynamic eccentricity evolve referring to counter electromotive force implemented in the simulation reference model:

$$K^i_{fcem} = K^i_e(\theta_m) \cdot \Big(1 + \zeta \cos\Big(\theta_m + \frac{(i-1)2}{3}\pi - \Omega t\Big)\Big) \tag{2.19}$$

The counter electromotive coefficient modulation K^i_e expressed in (2.19) as mechanical angle θ_m, allows reproducing with accuracy based on analytical representation the effects on counter electromotive forces by the rotor dynamic eccentricity modulating the mechanical and the electrical air gap angle as time and Cr rotational speed function. The (2.19), considers also the 120° the (i) current phases displacement, it is integrated within Simulink® EMA reference model by applying trigonometric transformations in function block showed in 2.22.

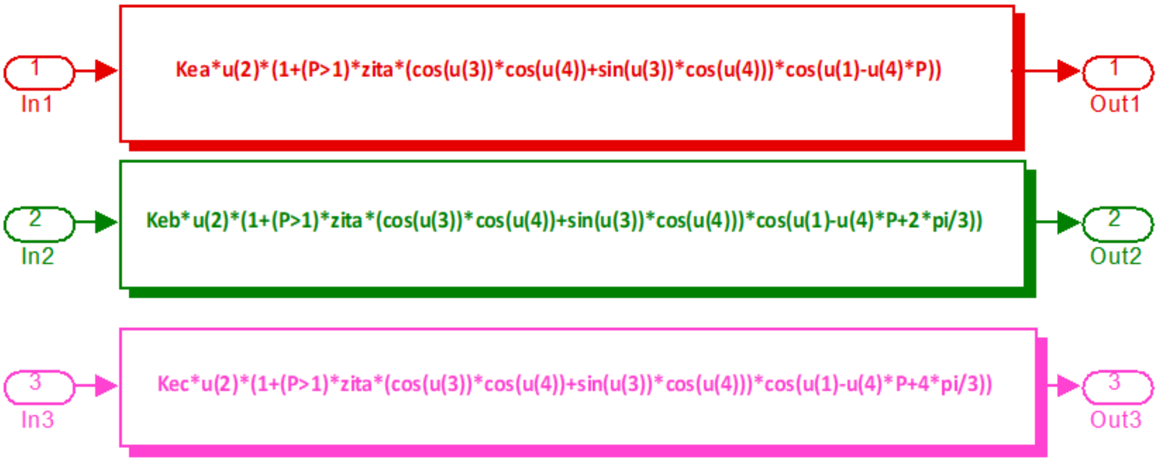

Figure 2.22: Simulink Model Block in Reference Model, representing the modulation for counter electromotive force coefficients, for each supply current phase to model the effects on model of dynamic fault

2.3.5 Short Circuit Fault

The short circuit fault is an electric connection among at least two lines of an electric circuit at a different voltage, ideally considered without internal resistance and voltage drop across the accidental connection so the current is limited only by the resistance of the whole circuit. In a stator electrical configuration, the *"active lines"* interested by electromotive force generation, are positioned within the stator caves, two active connections connected with the respective *"frontal connections"*, that are not interested in EMF positioned in front of *"active connections"*, they constitute a stator turn. The set of turns which the active connections are displaced in the same pair caves, constitutes a coil, on the other site the coil frontal connections are defined as *"end winding"*. The turns are connected between them to constitute a phase winding, powered following a commutation logic by BLDC control system as described in fig. 2.4 on page 23. The short circuit phenomena, arising among the winding coils, can occur in three different fault modes:

1. Turn to Turn: Short circuit between windings belonging to the same phase;
2. Phase to Phase: Short circuit between windings belonging to different phases;
3. Phase to Ground: short circuit between windings coils and ground connection;

Statistically, a short circuit fault begins to arise between at least two turns of the same phase, inside the same coil, if not suddenly detected this SC type reducing motor performances, until fault propagation and evolution to SC phase to phase or phase to ground, in these cases the on-board safety electronic system completes a system breakdown.

The evolution from short circuit turn to turn in to motor failure is very difficult to simulate in the time domain, as a function of beginning insulation degradation and load profile of the BLDC, referred to aerodynamic load on the commanded primary control flight surfaces.

The main causes of the short circuit could be referred to a combination of different type of insulation stress:

- Thermal stress and exchange: ageing, overload, repeated starts.
- Electrical: dielectric, transient.
- Environmental: humidity, chemicals, abrasion, external objects.
- Mechanical: relative movement of the winding, rotor creep, vibrations induced by internal and external BLDC motor Mechanical behaviour.

The insulating coating prevents coils contacts and other conductive components, from the degradation beginning the phenomenon time evolution could be mainly due to windings temperatures associated with the previous study approach used by [8], focused on SC fault progression although based on different anomaly detection methods than the presented one in this research.

Thermal Stress

Usually, for each 10℃ of increasing temperature step the insulation cycle life, is halved, the thermal ageing makes the insulation exposed to the combination of another stress type as environmental factors. The only solution for this stress type could be reducing operating temperature increasing cooling actuator system or using insulation material with improving thermal resistance. The thermal overload could be caused by different electrical causes as voltage variations and unbalancing phase voltage. The maximum voltage variation is around ± 10% of nominal reference supply voltage, a three-phase supply for every 3.5% of unbalancing phase voltage, the temperature phase with the relative higher circulating current, increases of 25% respect a perfect voltage balancing operating condition. The repeated starts, increasing thermal stress related to starting currents normally are 6 times the maximum normal circulating current at full external load. This overcurrent coil increasing temperature but is limited in time envelope occurring during each actuator starting moving. The second repeating starts phenomenon is related to expansion and contraction of coils insulation, in a long time the insulation material under ageing become fragile and a fracture begins to arise. The coil temperature increases with the external load squares, generating overload thermal fatigue on insulation coils.

Type of voltage	Maximum voltage at the motor input terminals (V_{peak})					
				Example for V_{line}=400 V_{rms}		
	Phase to ground (frame) 2	1 Phase to phase	3 Turn to turn	2 Phase to ground	1 Phase to phase	3 Turn to turn
Sinusoidal voltage, V_{line} (V_{rms})	√2 V_{line}/√3	√2 Vline	(√2 Vline/√3)/N	± 327	± 566	± 327/N

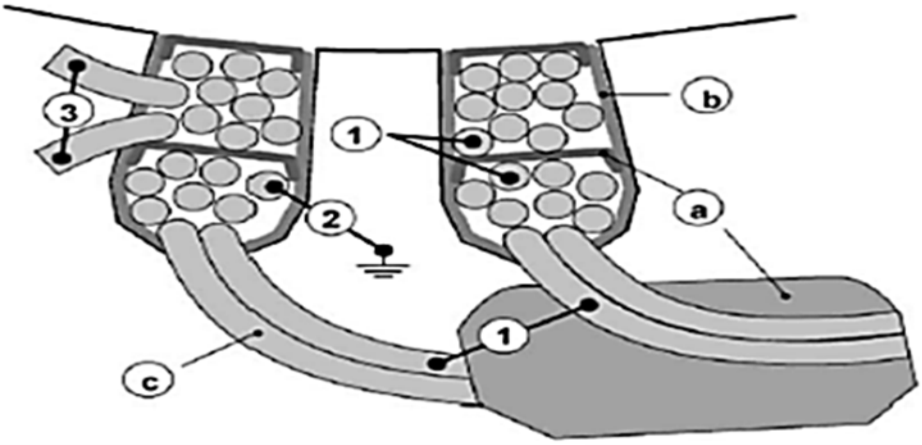

Figure 2.23: Stator windings components with an overview Voltage mapping referred to V_{line} voltage supply

Electrical Stress

The electrical stresses for low voltage supply ($V_{supply} < 2300V$), are mainly due to a different voltage at the different winding parts, where N is the number of phase coils. The inverter supply for BLDC motor, used as an electromechanical actuator in this research, is affected by electrical stresses caused by voltage transients as consequences of the value of impulse frequency. In this case, the turn voltage may increase up to $40 - 70\%$ of the nominal voltage supply at the motor terminal board. The PWM pulse with modulation attempts to simulate a sine wave by activating full voltage pulses in rapid succession, to avoid electrical noise the frequency commutation can be raised to 20KHz. The pulse voltage shape, to get higher modulation frequency, is set from 10% to 90% of the bus voltage line supply, in 1 μs one-millionth of a second the thermal balance is strongly influenced by satisfying this requirement. Another electrical stress on insulation due to voltage transient is the voltage spikes from a PWM output, where each trapezoidal pulse begins with over-voltage spikes nearly twice the DC bus generating pin holes in coils insulation. The implementation within the reference model considers only the short circuit turn to turn type since is the only short circuit allowing motor operation. In the first approximation turn to turn short circuit causes a decrease in phase resistance and inductance acting on counter electromotive force and torque gain defined as follow:

$$K_{fcem} = \frac{\partial \Phi}{\partial \theta_m} = nA\frac{\partial}{\partial \theta_m}\left(\int_A B - nd\,S\right) \tag{2.20}$$

Indicating with n the number of coils within a phase winding, A the normal stator area referred to a winding cave, B the magnetic rotor flux density. In this research we indicate with N_i (where "i" is the phase index for phase a, phase b, phase c), the percentage of operative coils affecting respectively for each phase resistance R_i inductance L_i and $k_e^{(i)}$ normalized counter electromotive force, calculated respect the same variable R, L, k_e in healthy conditions as indicated follow:

$$R_i = N_i R \tag{2.21}$$

$$L_i = N_i^2 L \tag{2.22}$$

$$K_e^{(i)} = N_i K_e \tag{2.23}$$

The electrical stresses, related to ramp slope focused on voltage pulse shape, in the presented reference model are avoided by simulating a t_r time ramp up (or rise time) at 1 μs and squaring overshoots. Therefore, the simulation framework is focused only to analyze the effect of increasing short circuit turn to turn in concurrence mode with another type of EMA failures as rotor static eccentricity.

2.3.6 Mechanical Faults and Tribology

Part of the work described in this section was also previously published in [13]. The aerodynamic load, acting on primary control surfaces in aircraft, is transmitted to rotor actuator shaft through transmission line elements as a gearbox, screwball jack and bearings. Thus, the transmission line surfaces in relative motion, are subject to mechanical wearing, a strongly no linear degradation, increasing looseness, backlashes affecting position accuracy and efficiency of the whole primary flight control system. Beginning from the initial manufacturing tolerances and defects, mechanical wear is distributed among all surfaces contacts in motion, so it is possible to estimate the increasing consumption by indirect evaluation of friction coefficients increasing (static and dynamic). This evaluation is correct in the same load, boundary conditions and material, of a mechanical system, avoiding environmental effects able to influence hydraulic behaviour of lubrication system directly involved in Tribology responses as temperature and contaminants. It's important to notice that, for prognostic evaluation methods and algorithms, other important wear effects, on safety-critical components like mechanical fatigue, are not considered in this work because starting for initial fracture nucleation the fatigue effects have a hidden evolution to be investigated only by non-destructive controls, often by complex experimental investigation, before the sudden fracture failure may occur.

The incipient failures, related to progressive wear, could be estimated by increasing friction coefficients except for wear consumption affecting the rotor bearings where rotor static and dynamic eccentricity are considered in the reference model by a specific mathematical model. The wear effects on mechanical transmission improve backlashes and misalignment phenomena, acting along axis line and meshing gearbox contacts, improving vibration responses until actuator jamming with catastrophic consequences.

Several simulation models are deployed on bibliography, detailed analysis and comparison of the main contributes are presented in [19]. In the presented EMA reference model, the *Borello* friction model [16] is implemented within *"BLDC motor Dynamic model"*. The friction simulation model, with adequate accuracy, must consider an appropriate identification and modelling of dissipative phenomena compared to the real progress of the physical system. The Friction phenomena are a function of the normal load exchanged between surfaces of the relative sliding speed, in addition the relationships between the dry and friction forces, considering these speeds have an extremely non-linear trend. Therefore, a too large linearization would result in a loss accuracy of the simulation model, due to the study of algorithms compensation improving performances. The elaboration of models, able to describe the behaviour of the phenomenon in question, considers beyond the relative sliding speed, the load exchanged between the mechanical components and the lubrication regime acting between the surfaces.

Depending on the sliding speed, the phenomenon can be divided into friction static, in which the relative movement between the surfaces is null, and in dynamic friction in which the surfaces are in relative motion. The friction forces exchanged between surfaces in the two relative speed regimes (F_s Static friction force, F_d Dynamic friction force) it is described by the following mathematical relations where N is the normal load exchanged by the surfaces in contact f_s is static friction coefficient and f_d is the dynamic friction coefficient:

$$F_s = f_s N \tag{2.24}$$

$$Fd = f_d N \tag{2.25}$$

$$\tag{2.26}$$

The elaboration of an exhaustive friction model must be able to describe mathematically the behaviour of the mechanical element, discriminating among the following kinematic conditions are shown below:

- **Static condition:** the mechanical elements in contact initially stationary, without relative motion, remain stationary as a function of the load resultant applied;
- **Starting Condition:** the initially stationary mechanical elements in contact, begin to relative motion, changing from static friction condition to dynamic condition;
- **Motion condition:** the mechanical elements initially in motion state, these elements maintain motion condition since the load resultant acting on it;
- **Stopping condition:** the mechanical elements initially in motion state stop changing in a null motion condition;
- **Condition of Sign:** in the case of dynamic friction the system must discriminate the sign of the frictional force according to the sliding speed reference system;

A friction model, able to satisfy the aforementioned conditions, allows calculating with sufficient accuracy, a dynamic tribological framework. We prefer to integrate into the reference simulation model a *Borello* algorithm classified as *"High fidelity Performance Models"*. This friction model is able to provide a global representation of the friction representation on operating conditions, rather than defining more complex FEM models of tribological derivation able to capture effects and local dynamics to the detriment of the global behaviour of the system under analysis.

Borello Friction Model

In the *Borello* Model, the frictional force F_f is a function of the active force resultant F_{act} and of the sliding speed $DXJ\, or\, \dot{x}$ as reported following equivalent coulomb model. The other quantities that appear in the mathematical model are Fsj static friction force in stick condition, Fdj the dynamic friction force. The proposed Simulink® model, shown in 2.24, proposed a logic block able to detect the zero crossing velocity point, used to reset the integrator block to calculate sliding speed for an integration time step to a null value. Indeed, the particularity *Borello* model [16] is focused on reset sliding velocity to a null value in the presence of inversion speed sign avoiding numerical oscillation typical for numerical model affected by step discontinuity as all the numerical friction models. In the time step following when the null velocity is imposed by crossing zero point detection, if the Fact active forces resultant, is greater than Fsj static friction force the system is configured in start-up motion condition otherwise the current position is held. The stop condition is represented by multiplication of sliding speed value at generic integration time t_n and t_{n+1}, if the results are minor or equal to zero in crossing point condition the sliding speed at tn+1 is imposed to zero value. This numerical solution

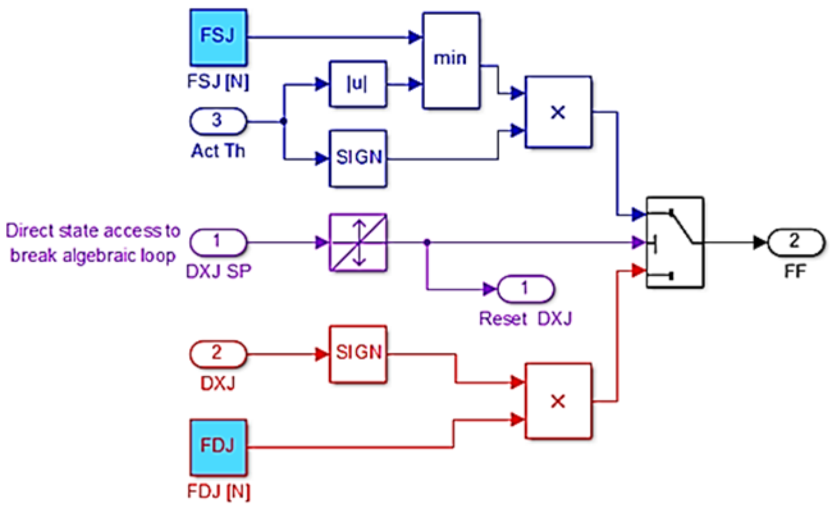

Figure 2.24: Simulink® reference model integration of Borello friction model

allows avoiding reset physical model parameters to ensure numerical convergence to detect stick condition as used in other numerical friction models like Karnopp's [49] model with a dead band across zero sliding speed value, or Quinn's model [65] with the related linear hyper viscous coefficient. The reset DXJ output after the zero-crossing sign detection block is used to reset the speed integrator State port to calculate the motor speed when it is reset the state port take the output speed value assumed if the reset condition did not occur avoiding algebraic loop.

$$F_f = \begin{cases} F_{act} & \text{if } \dot{x} = 0 \wedge |F_{att}| \leq F_{Fsj} \\ F_{dj} \cdot sgn(F_{act}) & \text{if } \dot{x} = 0 > |F_{att}| \leq F_{Fsj} \\ F_{dj} \cdot sgn(\dot{x}) & \text{if } \dot{x} \neq 0 \end{cases} \tag{2.27}$$

Chapter 3

Harmonic Analysis

3.1 Simulation Boundary Conditions

The numerical model, for EMA electromechanical actuator described in previous section 2.2 on page 27, can simulate with an adequate degree of confidence, the physical behaviour for an electromechanical actuator used for primary flight control system considering different types of non-linearity as:

- Columbian friction models both static and dynamic conditions;
- Backlashes and End-Run conditions as in [18]
  (es. Simulating End-Run for components in relative motion);
- Electrical Hysteresis PWM Controller Commutation Logic;
- Electrical White Noise acting on ACE Actuator Control Logic System;

The electromechanical actuator represents a mechatronic component on which interact three interconnected sub-discipline fields, able to transform the electrical power, driven by the electronic control system, into mechanical power, connected by transmission line and gearbox to the aerodynamic surface, through the rotating magnetic field. The technical parameters, used for the setting of the Simulink® simulation model, are derived from technical brochure spreadsheets of a real EMA coming from Faulhaber Model 4490 series, whose technical data are reported in appendix A on page 141. The Faulhaber Model 4490 series is chosen as real reference EMA, in this dissertation improving results accuracy for the proposed FDI algorithms. The FDI model-based approach puts in evidence the degradation path of EMA affected by following combined progressive failures:

- **SC** turn to turn short-circuit;
- **RSE** rotor static eccentricity;
- **RDE** rotor dynamic eccentricity;

- **Friction Static User coefficient (FSU)** static friction user coefficient as a marker for mechanical transmissions and lubrication inefficiency;

The Interactions among the above-mentioned different failures types, work in concurrent modes on several variables, but the generally FDI algorithms consider only a limited set of variables called *"prognostics precursors"*. In this work the main prognostic precursors are the filtered phase currents I_a, I_b, I_c supplying the stator coils, generating the rotating magnetic field, identifying malfunctioning, minimizing the unannounced failures by applying the proposed FDI methodologies. Other variables could be considered as prognostic precursors, for example the bearing operating temperature as a further precursor of bearings wear, but in the proposed methodology based on spectral harmonic analysis, filtered phase currents are the only failure precursors signals composed by DC static and AC oscillating dynamic components able to define a system dynamic firm referred to the interaction of the four failure types and the three physical fields. In other words, RSE, RDE and FSU are three different types of incoming failures, related to mechanical wear of bearings, sliding surfaces, and meshing contacts in gearbox connecting EMA to the aerodynamic surface, but the effects of these mechanical failures modify the symmetry and intensity of the magnetic field. In a BLDC motor changing symmetry and intensity of the magnetic field, due to wear and related misalignment between stator centre and rotor centre axis or indirectly by increasing friction coefficients, induces changes in the waveform for filtered phase current, more evident after a proper application of digital signal processing. If we consider coils insulation wear due to thermal fatigue, the short circuit *turn to turn* modify in a different way the waveform of the prognostic precursors and the influence on the dynamic EMA firm is reported in following sections of this elaborate. Therefore, in conclusion, the filtered phase currents can describe in the frequency domain, by the proposed methodologies, the physical health state of the EMA and the driven mechanical transmission line under reference operating conditions.
The reference operating conditions are referred to flight phase called *"Standing"* used by the Aviation Data Reporting Program (ADREP), maintained by the International Civil Aviation Organization (ICAO), to categorize operational flight phases, before takeoff and landing phases. The *"Standing"* phase interested by the main reference operational conditions to compare with FDI algorithms results, is that occurs before the takeoff phase during the pre-flight test on avionics subsystems. There is a phase called "preflight" by International Air Transport Association (IATA) classification, it could be considered an inner sub-phase within the *"Standing"* flight phase since an increasing standardization of industry accepted taxonomy covers an essential role in safety as indicated by [72].
In this reference sub-phase, all the self-checks of avionics subsystems are performed by the crew, to guarantee safety to the following flight phases, reducing risk around airports, as reported by improvements for calculation of third-partyrisk performed by [3]. The aircraft, on this reference phase, is on the ground at the gate, ramp or parking area, while it is stationary, prior to push-back or taxi phase, the related reference operational conditions provide for a fully driven movement of ailerons from the minimum to the

maximum upward angular range imposing a step command at the maximum value by pilot. The above-mentioned reference operational condition needs to be translated in the following simulation boundary conditions:

Step Command at high value: the simulation model quickly saturates all feedback loops of the electromechanical actuator controller, acting as an open loop dynamic response, allowing to reach in any load condition the maximum actuator user speed connected with EMA rotor used in simulation framework by [11] and reported by [83]

No External load: during the preflight phase the aircraft is stationary therefore maximum no load velocity is reached in the minimum time applying step command at a high value. The only force, acting on the aerodynamic surface, is the weight force applied to surface mass centre generating in these operating conditions the hinge moment. The wind effects on ailerons during Stationary phase on the ground is negligible compared to increasing resistant torque correlated by increasing friction constants affected by mechanical transmission line and gearbox.

These reference operational conditions, are defined to perform both proposed model based FDI algorithms, to be compared with experimental data driven approach in the same conditions, avoiding on prognostic precursors dynamic responses the dynamic contributions due to aerodynamic and structural spectral contributions. The aerodynamic load and structural vibrations could be considered harmonic sources very difficult to manage in a model-based framework affecting the precursors' dynamic bandwidth responses, not directly correlated with the physical health state of the mechatronic component. During the aircraft stationary condition, before the takeoff phase when the engines are not operating,the correlated structural vibrations transmitted by the wing structure, with its own viscous elastic dumping, could be considered negligible on EMA or well filtered by a signal filter applied to FDI precursors. The respect of the reference operational conditions on the ground, guarantees the best comparison conditions to perform the real test on EMA for primary flight systems with the failures maps derived by the proposed FDI algorithms able to quantify system health state.

3.2 The Fourier Transform

Defined boundary conditions for EMA numerical simulations in 3.1, the simulated prognostic precursors are the main targets for the harmonic analysis to detect the impact of incoming different type of failures operating in concurrent mode on the actuator. The harmonic analysis is the disciplines concerned the study of time signals, based on decomposition of basic waveforms through analytical transformations, a class of signal analysis techniques: time-frequency analysis. The set of analytical transformations for time-frequency analysis in bibliography [21], includes several time-frequency distributions, classified by Cohen class, but in this work the harmonic analysis is performed

based on the most important transformation "The Fourier Transformation" [41].
The Fourier transformation is a linear and integral transformation able to associate every continue time functions to an equivalent representation in the frequency domain as represented by (3.1) and the inverse transform in (3.2).

$$X(f) = \int_{-\infty}^{+\infty} x(t)e^{-i2\pi ft}\,dt \tag{3.1}$$

$$x(t) = \int_{-\infty}^{+\infty} X(f)e^{i2\pi ft}\,df \tag{3.2}$$

The Fourier Transformation (FT) application field is not limited to only continuing time functions but is extended also to the stepped continue time function during the all-time history allowing integration. The transformation on the frequency domain, it makes possible and easier to characterize and describe different physical functioning conditions by correlating the results in equivalent terms of amplitude frequency and phase for infinite sums of sinusoidal components. In the proposed FDI algorithm, the performed harmonic analysis, detailed described in the following sections, can define in the frequency dominion based on FT, how the dynamic firm is modified by the effects of incipient failure types described in section 2.3 on page 36, impossible to define easily in the time dominion for time variant simulated prognostic precursors.
As a direct consequence of the original signal decomposition, the Fourier transformed function is parametrized only as frequency functions, in other words there is no coupling correlation between time dominion e frequency dominion except for the mutual relationship between time and frequency. A non-stationary time domain function is transformed by Fourier operator in a variable frequency domain function, therefore the limit of harmonic analysis is confined in the frequency domain without understanding when the harmonic studied frequencies took place in the time history, with an evident time localization for the spectral component. From the Signal Theory, the Parseval Theorem [56], the time signal energy is equal to the same equivalent frequency signal in the frequency domain, therefore the density energy distributions are correlated under the global relationship.

$$\int_{-\infty}^{+\infty} |x(t)|^2\,dt = \int_{-\infty}^{+\infty} |X(f)|^2\,df \tag{3.3}$$

The above-mentioned harmonic analysis characteristic, seems to limit the FT only for quasi static problems where it is not needed a simultaneous analysis of the complex problem simultaneously in time and frequency. Similarly to what happens during a doppler phenomenon, a simple analysis in the time domain would not be exhaustive mainly when the spectrum signals change for each considered time. Therefore it is needed introducing an accurate methodology able to give effective information about the frequency domain.
The EMA simulation model simulates the filtered phase currents under specific reference operational conditions, but these signals are non-stationary during the time history,

modulating sinusoidal frequency component for these waveforms in frequency and amplitude. The best solution, to extend the above-mentioned FT limit to the coupling between time and frequency domain, is represented by the STFT analytically represented by the following equation:

$$STFT\{x(t)\}(\tau,\omega) \equiv X(\tau,\omega) = \int_{-\infty}^{+\infty} x(t)\omega(t-\tau)e^{-j\omega t}\,dt \tag{3.4}$$

Avoiding calculating the signal spectrum, over whole observation time, the STFT divides the non-stationary signal into smaller time intervals and applies the Fourier transform to each interval. Using the short time approach, the Fourier transformation generates many spectral diagrams localized in different time intervals, each harmonic contribution is associated with a specific time interval coming from partitioning of the time history observation. The time partitioning of the complete time history, is performed in the time domain, applying a windowing function w(t-τ), on integral linear transformation indicated in (3.4). There are some side effects related to applying windowing function on the original signal in the time domain, in fact by the convolution propriety of the Fourier integral linear transformation the multiplication in time has effects on frequency domain:

$$x(t) \cdot s(t) \Leftrightarrow X(f) \cdot S(f) \tag{3.5}$$

3.2.1 The Fourier Series

The Fourier Series (FS) is a transformation of a periodic function in the time domain in an infinite sum of sines and cosines that define an orthonormal function base as reported follow by function decomposition in a trigonometric polynomial:

$$\begin{aligned} x(t) &= A_0 + 2A_1\cos(2\pi f_0 t + \theta_1) + 2A_2(2\pi 2 f_0 t + \theta_2) + 2A_3(2\pi 3 f_0 t + \theta_3)\cdots \\ x(t) &= A_0 + 2\sum_{k=1}^{+\infty} A_K \cos(2\pi k f_0 t + \theta_k) \end{aligned} \tag{3.6}$$

The series is a main tool for the harmonic analysis to break up an arbitrary periodic function of T_0 period, into simple terms solved individually. The sinusoidal terms are harmonically linked, in fact each sine had multiple frequencies of the fundamental frequencies f_0 as the inverse of function period under analysis. The frequency analysis calculates frequency amplitudes, defining the Fourier Coefficients A_k, and phases θ_k of the (3.6). There are three convergence types of the FS :

1. **Uniform Convergence (or full convergence)**: if the time origin function is uniformly continuous in the observation time, the FS can remark all original time function points by inverse FT applied on FS decomposition;

2. **Punctual Convergence**: the FS remark the original time function only in the point on which the continuity property is verified. The sufficient conditions for this convergence type are defined by Dirichlet;

(a) The time function can be integrated on T_0;

(b) The time function is continuous except a finite points number with a jump discontinuities;

(c) The time function derivative exists except a finite points number where the right and the left derivative exist even if different;

3. **Convergence on Average Quadratic**: this is the less restrictive convergence for FS, based on Parseval theorem, assuring that the difference $e(t)$, between the signal and its representation within the frequency domain, has null energy:

$$\int_{T_0} |e(t)|^2 \, dt = 0 \tag{3.7}$$

As indirect propriety of the convergence on average quadratic, is that the FS on periodic signals that present finite energy on period T_0 satisfying the following condition:

$$\int_{T_0} |x(t)|^2 \, dt < +\infty \tag{3.8}$$

The power of a periodic signal in analogy with Parseval theorem, could be expressed as an infinite sum of FS harmonic components considering quadratic amplitude:

$$\frac{1}{T_0} \int_{T_0} |x(t)|^2 \, dt = \sum_{k=-\infty}^{+\infty} A_k^2 \tag{3.9}$$

Therefore, the energetic content of a time signal is preserved changing representation in the frequency domain by FS decomposition.

3.3 Signal Discretization

The FT and FS are the main linear transformations to decompose a time signal in to simply sum of harmonic components, changing perspective to analyze it. The digital system, to carry out these transformations, needs these fundamental operations on analogical continuous signals: **sampling, partitioning, frequencies discretization**. Each of these main operations can significantly influence the harmonic analysis reliability.

3.3.1 The Sampling

An analogical signal $x(t)$, is sampled by the constant f_s sampling frequency, extracting only the function values in correspondence of time equidistant points spaced of T_s as reported in fig. 3.1. In the analytic field, the sampling could be expressed a convolution for $x(t)$ multiplying $s(t)$, an impulses function of unitary magnitude and equidistant

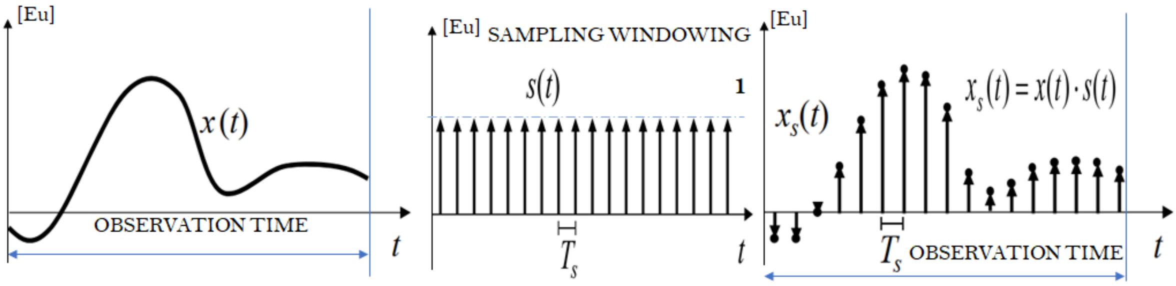

Figure 3.1: The sampling operation to make discrete a continuous time signal $x(t)$

spaced of T_s , whose $S(f)$ is the relative transformed function in frequency domain. Also, in frequency domain $S(f)$,it is still an impulses function but equidistant spaced of f_s. The result of this sampling convolution $x(t) \cdot s(t)$, is reported in fig. 3.1 with the related FT, they are analytically expressed by following relations:

$$x_s(t) = x(t) \cdot s(t) = x(t) \cdot \sum_{i=-\infty}^{+\infty} \delta(t - iT_s) = \sum_{k=-\infty}^{+\infty} x(iT_s) \cdot \delta(t - iT_s) \tag{3.10}$$

$$X_s(f) = X(f) \cdot f_s \sum_{k=-\infty}^{+\infty} \delta(f - kf_s) = f_s \sum_{k=-\infty}^{+\infty} X(f - kf_s) \tag{3.11}$$

A generic graphical representation of the DFT is shown in fig. 3.1 referred to equation (3.10), where the spectrum of the sampled signal is composed by harmonic replies of the $X(f)$ spectrum, multiplied by scale factor f_s. This simplified representation of a DFT,

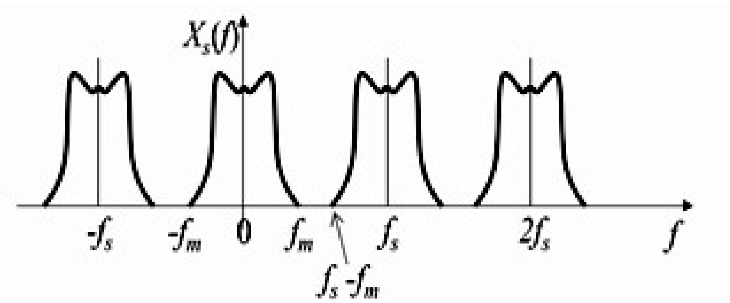

Figure 3.2: A generic graphical representation of a DFT in frequency dominion $X_s(f)$

gives a graphical simple way to describe the most important issues related to sampling operation: The **Aliasing phenomenon**. Indeed, to avoid overlapping of the spectral components, as showed in fig.3.2 the point $f_s - f_m$ must satisfy the condition reported in following relations representing the Sampling Theorem:

$$\begin{gathered} f_s - f_m > f_m \\ fs > 2f_m \end{gathered} \tag{3.12}$$

But this condition is the main requirement to avoid spectral distortions due to sampling called Aliasing that generates spectral artefacts not correspondent to any physical or simulated phenomenon under harmonic analysis.

3.3.2 The Aliasing

In signal processing discipline, the Aliasing phenomenon refers to spectral distortion due to windowing sampling function $s(t)$ multiplied to original time function $x(t)$. The sampling windowing function is characterized by a specific f_s sampling frequency, and the original time signal presents f_m the maximum frequency harmonic contribution within the observed considered time. According to *Nyquist Shannon Theorem*, the sampling frequency f_s must be twice of the f_m maximum signal frequency, during the ADC analogic to digital conversion. This requirement for frequency sampling, ensures a discretization without information loss, allowing signal recovery from frequency decomposition by the inverse discrete Fourier transformation.
The EMA Simulink numerical model, calculates all the discrete variables with an integration time step equal to 10^{-6} seconds, during the whole simulation time. Therefore, the simulation model works as a virtual test bench with an equivalent virtual acquisition system, acquiring at 10^6 Hz of sampling frequency. The proposed simulation sampling density allows avoiding any Aliasing issues, for the simulated prognostic precursors giving a bandwidth of 5^6 Hz for each performed Short Time Discrete Fourier Transformation (STDFT) (3.13).

$$STDFT\{x[N]\}(m,\omega) \equiv X(m,\omega) = \int_{-\infty}^{+\infty} x[N]\omega(N-m)e^{-j\omega N} \tag{3.13}$$

The sampling process, from ADC analogical to digital conversion, implies to use DFT able to evaluate harmonic content of a sampled signal with N number of the x(t) time samples. In a similar way to compare correctly the harmonic results of the proposed FDI algorithms coming from virtual simulation test bench, and the real acquisition data system onboard, the avionics systems must be equipped with anti-aliasing subsystem to guarantee the same accuracy in the harmonic analysis performed by the proposed simulation framework.

3.3.3 The Spectral Leakage

Summarizing up to this point, the original time signal $x(t)$, which in the present work is representative of the FDI prognostic precursors, is elaborated by STDFT including both sampling operation $s(t)$ (3.10) at fixed f_s , and partitioning operation through another windowing function $w(t)$ (3.4), which divides the whole time history signal into finite time observation subsets. Both the windowing functions have a strong impact on the original signal, being applied over time dominion by the convolution property of Fourier Transformation. The windowing operation, both in continuous and discrete mode, introduces high distortions also in the frequency domain. This phenomenon is called *Leakage* and is essentially related to the truncation of a generic time signal by means of a time interval called T_w *Time Section.* The partitioning phase of a sampled signal is performed by applying rectangular window function, defining a finite number of samples to be transformed by STFT in frequency dominion, smearing the spectral energy to all the bandwidth frequency.

$$w(t) = \begin{cases} 1 & -\frac{T_w}{2} < t < \frac{T_w}{2} \\ 0 & \end{cases} \tag{3.14}$$

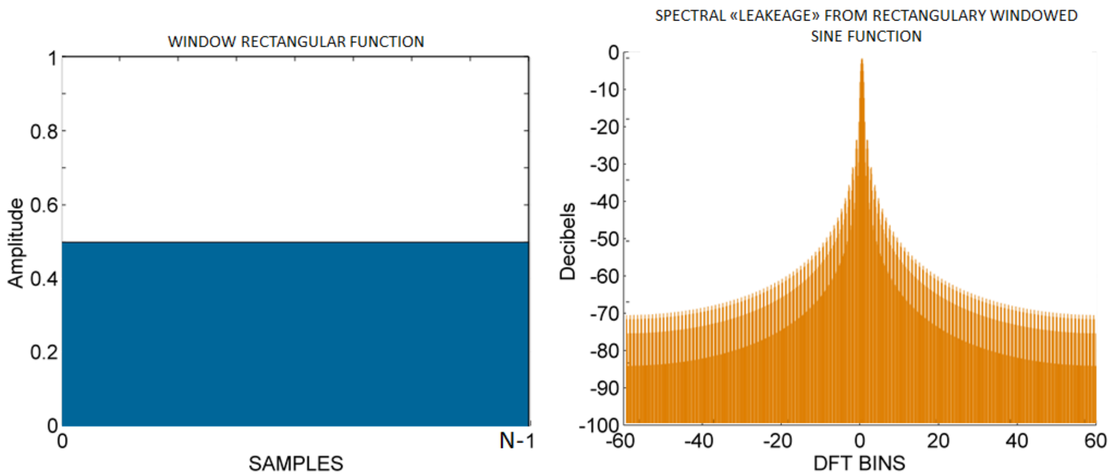

Figure 3.3: Rectangular Windowing Function on the left expressed in time dominion as function of N-1 samples on the right the related DFT spectrum

In the frequency dominion, the smearing entity is a function of T_w the length in time of the time section, and its analytical form. The analytical window form, determines the accuracy for the spectrum calculation, introducing a different type of smearing amplitude focusing differently near the maximum amplitude frequency. The rectangular window function smears the spectral energy to all frequency within the signal content bandwidth. Instead of the Hanning windowing own to smoothing windows class, presents a more focused frequency interval, on which smearing the spectral energy of the partitioned

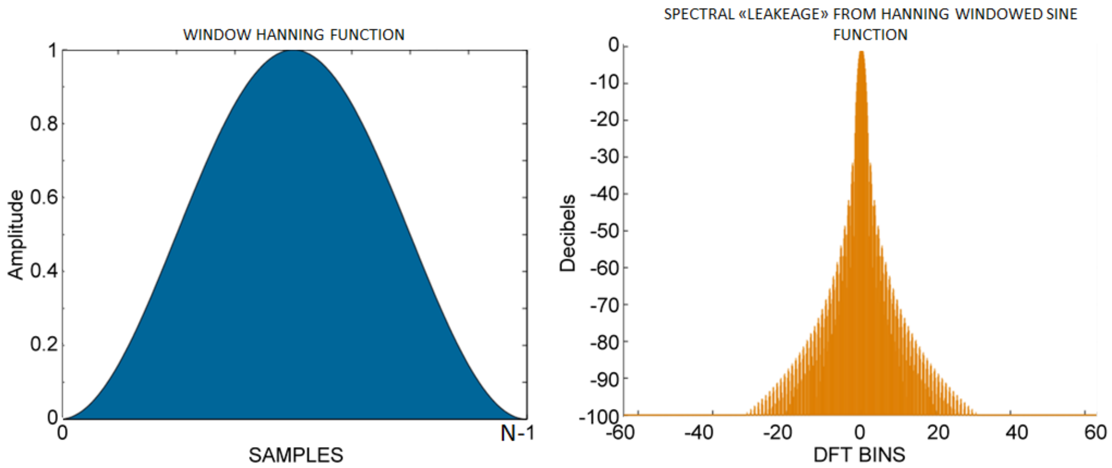

Figure 3.4: Hanning Windowing Function on the left espressed in time dominion as function of N-1 samples on the right the related DFT spectrum

signal, with the same time section at the same sampling frequency as showed comparing fig. 3.3 and fig. 3.4 in the frequency domain.

3.3.4 The Frequency Discretization

The finite time sequence, with samples N, is transformed in a discrete representation in frequency dominion by DFT, where the spectrum is represented by equally spaced X_k harmonic components called *spectral bins* or *spectral lines*. The distance among spectral bins is called f_w *frequency resolution*, directly related to the inverse of time section length T_w. In the eq. (3.14), the DFT transforms the time sampled x_i into a finite sum of complex exponential to determine X_k spectrum harmonic components, following the harmonic order k (integer order k=1,2,....) within the bandwidth.

$$X_k = \sum_{i=0}^{N-1} x(iT_s)e^{-j2\pi k f_w iT_s} = \sum_{i=0}^{N-1} x_i e^{-j\frac{2\pi}{N}ki} \qquad \left(with\ f_w = \frac{1}{T_w} = \frac{f_s}{N}\right) \tag{3.15}$$

Practical interest for operative application is the Discrete Fourier Series (DFS), a time-frequency transformation applied to periodic discrete time function for harmonic analysis. In this case, the leakage phenomena, ever related to time signal partitioning, is strongly influenced by the synchronization between the f_s sampling frequency with f_0 the sinusoidal main frequency, observing the Nyquist Shannon Theorem requisite at (3.12). Indicating with m the number of function period T_0, captured by partitioning algorithm, the relation between the sampling frequency, the frequency resolution f_w and the main signal frequency f_0 is expressed in Eq. (3.16).

$$f_s = N f_w = N f_0/m \tag{3.16}$$

If m is an integer and the N/m ratio is an integer, therefore we are in a condition of coherent sampling in perfect synchronization between sampling frequency and the main signal frequency, where the STFT transformation giving a correct spectrum representation minimizing leakage phenomena. On the contrary, if the N/m ratio is not an integer number, it means that the *time section* doesn't fill an integer number of the signal period. The main consequence is a strong spectrum distortion due to leakage related to signal to partition by windows function. To solve this issue, a choice of a function within smoothing windowing class is performed partitioning time signal, reducing spectrum leakage, and satisfying local periodicity on time section as reported in fig. 3.5.

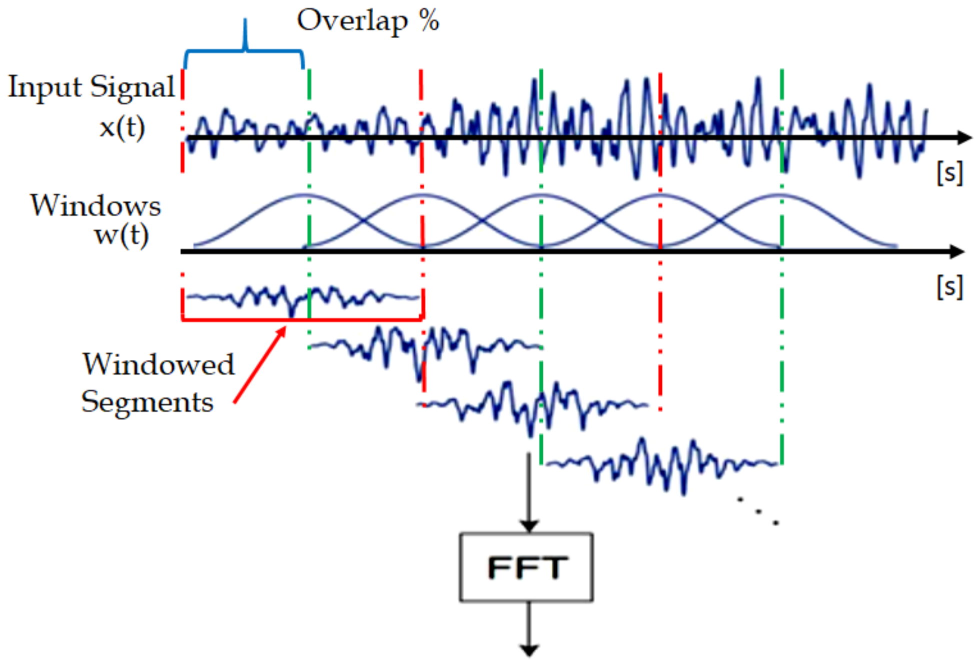

Figure 3.5: Overview Partitioning and Windowing operation, with overlap on time signal

The probability of loss signal information in time is high, respect samples placed on outer interval limits, where the windowing function usually tapering up to zero, in comparison with the samples placed on the middle of the *time section*. The solution, to mitigate this type of loss information towards time interval extremes, consists to slide the *time sections* by a time percentage from the original signal beginning, overlapping separated time sections. The overlapping process reduces the loss information, due to smoothing windowing functions, applied to partitioned not sequential *time sections*. Moreover, it increases the number of the calculated spectrum by STFT improving accuracy in the spectrum related to FFT performed on time non-stationary signals. However this analysis method for non stationary signals elaborated by FFT, just introduced by [46] has a number of limitations. All the limitations could be summarized in the research of the proper windowing function, to apply on time signals able to highlight the main signal significant characteristics related to the physical behaviour of the study case.

3.4 Digital Signal Processing Parameters

This paragraph has a target to summarize the above-mentioned technical parameters performing an STFT on input time signal, defining a dynamic firm for prognostic precursors generated by EMA simulation model:

- **Sampling Rate**: it is commonly indicated as f_s *sampling frequency*, and it is expressed in *Samples/s* rather than *Hz*. The higher frequency components need to be measured, the faster you need to sample. The frequency resolution governs the size of digital data files, the T_s elapsed time between samples, and spectrum bandwidth. To get close to the correct peak amplitude, in the time domain by sampling, it is important to sample at least 10 times faster than the highest frequency of interest;

- **Frequency Range**: it commonly indicated as f_m, it is the maximum signal frequency, calculated from input time signal. An acceptable sampling discretization it's necessary to satisfy the Nyquist Shannon Sampling Theorem in (3.12);

- **bandwidth**: it is commonly indicated as bdw, and it is the maximum frequency calculated by the FFT algorithm, as a function of the sampling rate. The relation between sample rate and bandwidth depends on dynamic acquisition software. More diffuse acquisition systems indicate in a technical spreadsheet, anti-aliasing hardware filter in the frequency domain: $bdw = \frac{fs}{2{,}56}$. Normally the bandwidth must be wider than the frequency range to describe it without further approximations due to anti-aliasing filter attenuation;

- **block size**: it is commonly indicated as N, and it is the number of samples in time dominion analyzed in a single FFT operation within a time section;

- **time section**: it is commonly indicated as T_w or Δs, and it is the time interval needed to collect a representative quantity of samples in time dominion, to elaborate a single spectrum FFT calculation. It should be a power of two, to have a more efficient FFT calculation avoiding *complement to the next power of two*;

- **frequency resolution**: it is commonly indicated as f_w or Δf, and it's the spacing between two consecutive spectral lines within an FFT spectrum. A higher frequency resolution allows, with the appropriate windowing function, to discern closely spaced frequency. The frequency resolution is the inverse of the time section, when are fixed sample rate, and windows type. Consequently, if frequency resolution is improved, the time section should be wider, introducing smoothing amplitude effects on the harmonic components calculated by FFT;

- **spectral lines**: they are commonly indicated as Sl, they indicate a total number of frequency domain samples, equal to half of N block size. Each harmonic component is represented by a magnitude correlated to a single spectral line, and they are equally spaced by frequency resolution;

The main DSP are technical parameters related to a simple mathematical relation useful to understand how fixed some parameters, other values are automatically set:

$$\Delta f = \frac{f_s}{N} = \frac{bdw}{Sl} = \frac{1}{\Delta s} \tag{3.17}$$

3.4.1 The FFT Fast Fourier Transformation

In the previous paragraphs, the mathematical evolution of the Fourier Transformation is explained, applying to sampled time signal by STFT, partitioning by windowing function with overlap for improving accuracy. The DFT is associated with a high computational effort, based on N time samples within the time section coming from time history partitioning. The number of operations needed, to calculate all spectral components, are on the order of N^2 (ex: for $N = 1000$ Samples are needed 10^6 arithmetical operations). The FFT algorithms, as [22] *"radix2"* Algorithm, are tools able to calculate the same DFT results with a more efficient number of arithmetical operations equal to $N \log(2N)$ (i.e. for a DFT results based on $N = 512$ samples FFT uses 4608 operations than 262144 without FFT). The radix2 FFT algorithm provides for N input samples, they must be an integer power of 2, but this requirement should be satisfied by *"complement to the next 2 powers"* where adding zeros to initial N samples to nearest 2 power. This procedure is called *"zero paddings"*, it doesn't introduce spectral distortion but only an improving frequency resolution proportional to the number of added zeros samples. Several implementations of DFT are developed adapting algorithm performance to hardware specifications as FFTW3 described by [33] as adaptative evolution of FFT. These FFT evolutions represent a best fitting computing solution to be installed on avionics hardware to perform a comparison between the proposed failure maps coming from proposed simulation framework and the real-timeharmonic results coming from onboard sensors on EMA. Although adaptative FFTW algorithms seem to be more efficient than the traditional one, several open problems remain. For the main research purpose the implementation of FFT, considering the continuous changing of computer hardware, is the best solution in terms of accuracy and stability for all generalized signal application. In this work to calculate the dynamic firm and its variation, under an incipient different type of failures, it's developed a specific module called *"Spectra"* based on STFT with FFT function with a complement of 2 powers following DSP parameters.

3.4.2 Technical Parameters for Windowing Function

In the subsection 3.3.3 and subsection 3.3.4, are illustrated the most important overviews, for what concerning a windowing functions applications on time input signal, considering spectral leakage. In the (3.14) is presented the rectangular window function, as the simplest windowing function able to cut off a signal portion for FFT transformation. The spectral leakage is due mainly by extremes discontinuities, they may occur during signal partitioning, therefore to understand how to prevent or mitigate spectral leakage effects should be useful to describe the main technical specifications for windowing function. The best window function selection is based essentially on the application of interest, in the PHM study a proposed assessment is performed, based on prognostic precursors signals, but there aren't general deterministic laws to choose uniquely the best windowing function. The harmonic analysis of a windowing class represented in 3.6 gives in the on sided FFT result, a graphical overview of the main window technical parameters:

1. Main lobe width: it is defined as the number of spectral lines corresponding to main lobe amplitude attenuation of -6dB corresponding to a halving of the maximum amplitude of the main lobe;

2. Side Lobes Maximum height: it is defined as the maximum amplitude level of the lateral side lobes expressed in decibel;

3. Roll-off rate: it is defined as the asymptotic slope that interpolates amplitudes decay, for the side lobes expressed in decibel/decade of frequency;

The main lobe width, fixed the frequency resolution for FFT transformation, impacts directly to distinguish two close harmonic components, in this case the width of the main lobe should be smaller than the frequency difference. On the other side, an improving frequency resolution, to distinguish close harmonic components, generates as side effects the smearing of signal energy on side lobes with higher spectral leakage. Therefore, the windowing function choice is a compromise between frequency resolution for the harmonic components or smearing dispersion on the side lobes.

In the proposed FDI algorithm, based on STFT applied to prognostic precursors, the choice of the best window function among the smoothing window functions class, is based on critical evaluation on harmonic analysis results assessment showed in the following chapters. A prearranged evaluation of the time signal could support the windowing choice. If close harmonic components are present in the spectrum, the width of the windowing main lobe represents the main windows parameter to evaluate avoiding masking effects. On the other hand, if harmonic interferences are not contiguous to the frequency of interest, the main window parameters should be a high *roll-off-rate* for the side lobes. For the most used window functions, the table 3.1 reports the technical DSP.

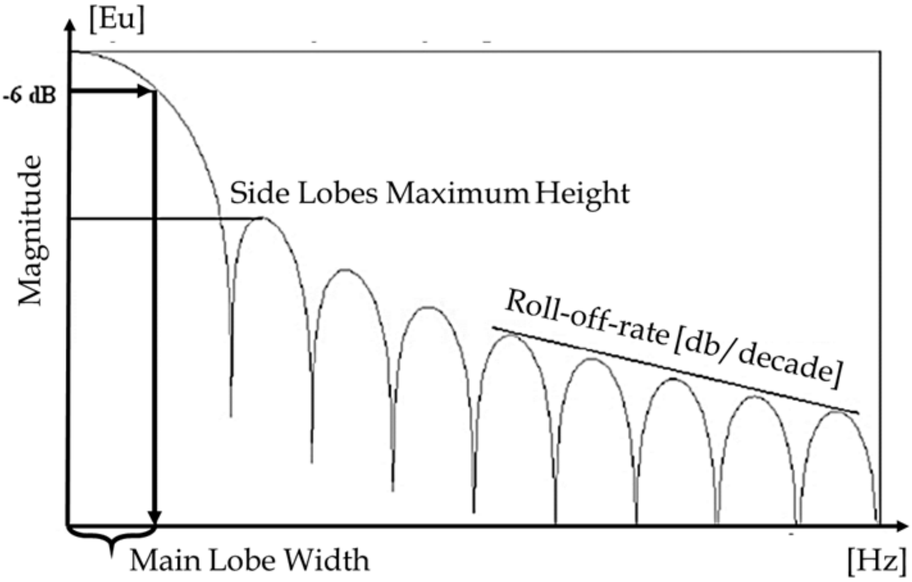

Figure 3.6: Technical parameters for windowing function based on one side FFT spectrum

Table 3.1: Main technical parameters for most used Windowing Functions

Windows Type	Main Lobe width (-6dB)	Side Lobes Max height	Roll-off rate (dB/decade)
Uniform	1.21	-13	20
Hanning	2.00	-32	60
Hamming	1.81	-43	20
Blackman-Harris	2.27	-71	20
Exact-Blackman	2.13	-67	20
Blackman	2.35	-58	60
Flat-top	3.56	-44	20

3.4.3 Amplitude Scaling for Windowing

The convolution product between input time signal and smoothing windowing function modifies the amplitude spectral lines but coming from the analytical expression of the windowing function in the time domain. The windowing functions are effective changing the time signal and take effects on the frequency dominion, therefore spectral amplitudes are scaled after FFT transformation. The amplitude scaling factor, known as *"window coherent gain"* reported in the tab. 3.2 is necessary to compare results coming from the same time signal using different windows functions. Another issue, related to spectral leakage, is the evaluation of windowing in the power spectrum signal, described in 3.4.6, where the power frequency of each spectral line is smeared on a number of near spectral bins. In an additional point of view, some smoothing window functions implied enlargement of power bandwidth, therefore to consider the power signal, associated with a single spectral component, it is fundamental defining the number of spectral bins near the interested frequency summing the power values for each not null spectral lines, divided for a coefficient *"noise equivalent power bandwidth"* as reported in tab. 3.2.

Table 3.2: Correction factors for most used Windowing Functions

Windows Type	Coherent Gain Scaling Factor	Noise equivalent Power Bandwidth	Amplitude Error Worst case(dB)
Uniform	1.00	1.00	3.92
Hanning	0.50	1.50	1.42
Hamming	0.54	1.36	1.75
Blackman-Harris	0.42	1.71	1.13
Exact-Blackman	0.43	1.69	1.15
Blackman	0.42	1.73	1.10
Flat-top	0.22	3.77	<0.01

Reference Spectral Bins: Indeed the smearing grade is a function of the windowing form, in the condition of coherence sampling,for example a sinusoidal reference signal, the windowed spectrum signal is smeared on 1 single bin for rectangular-uniform window, 3 spectral bins for Hanning window, and 5 spectral bins for Flattop window. If coherence sampling condition is not verified, the spectral leakage induces wider power smearing .

3.4.4 Picket Fence Effect

The DFT operates on the sampled time input signal, generating a discrete frequencies distribution equally spaced of f_w frequency resolution. Only the harmonic components in correspondence of discrete spectral lines are calculated and plotted on discrete FFT spectrum. This effect is known as *"picket fence effect"* to evidence that, where sampling generates spectral lines, an analogous view of the FT is placed behind a picket fence of width equal to f_w frequency resolution, observed through the tiny slits that separate them. The FFT calculates for each harmonic component the spectral lines correspondent to a maximum of main lobes and the zeros of the side lobes, incoherence sampling condition. Without a coherent sampling requirement, the maximum peaks are not exactly calculated in correspondence of the spectral lines equally spaced of frequency resolution. In this case, the FFT would calculate a maximum peak between two spectral lines but the power is distributed by spectral leakage over several near spectral lines, therefore to identify the *estimated frequency* and the *estimated magnitude* of the real

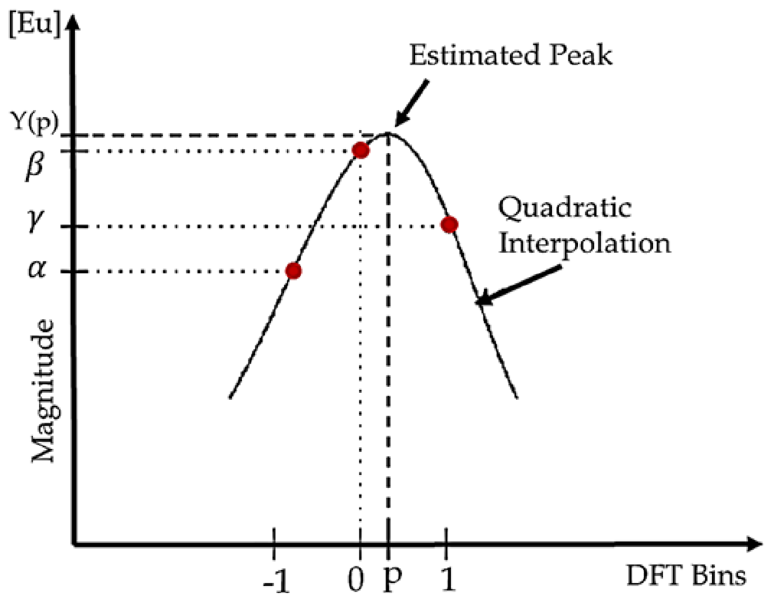

Figure 3.7: Qualitative quadratic interpolation to calculate frequency and magnitude for estimated peak based on 3 spectral bins in red points

peak, an evaluation is performed by a specific type of interpolation. The number of spectral lines, involved in the interpolation, to calculate the *estimated frequency* and the *estimated magnitude*, is function of the windows function used during the time windowing as reported in 3.4.3 for Hanning and Flatop windowing functions.

In presented work, the quadratic polynomial interpolation is used to estimate frequency and magnitude spectral peaks, under the hypothesis that the signal power around a frequency peak is distributed following a Gaussian distribution in time around nearest spectral lines as reported in fig. 3.7.

Using typical windowing functions, quadratic interpolation of spectral peaks is more accurate on logarithmic magnitude scale than on linear magnitude scale. The quadratic interpolation algorithm to detect peaks in spectral is reported below starting from generic quadratic function in (3.18).

$$y(x) = a(x - p)^2 + b \tag{3.18}$$

The estimated frequency p is expressed in spectral bins considering as local origin *Bin0* the maximum amplitude calculated by FFT algorithm. The correspondent parabola amplitudes $y(x)$, to be interpolated, are expressed in dB, quadratic curvature 2a is a function of windowing function applied.

$$\begin{cases} y(-1) & = \alpha \\ y(0) & = \beta \\ y(1) & = \gamma \end{cases} \tag{3.19}$$

$$\begin{cases} \alpha & = ap^2 + 2ap + a + b \\ \beta & = ap^2 + b \\ \gamma & = ap^2 - 2ap + a + b \end{cases} \tag{3.20}$$

Resolving equations system reported in (3.20) with the DFT calculated magnitudes in (3.19), the calculated parameter p is expressed in spectral bins on a local reference system as reported in (3.21) .

$$p = \frac{\alpha - \gamma}{2(\alpha - 2\beta + \gamma)} \tag{3.21}$$

$$y(p) = \beta - \frac{1}{4}(\alpha - \gamma)p \tag{3.22}$$

For what concerning the phase there are no relation between quadratic amplitude interpolation and the correspondent phase therefore a Linear interpolation to interpolate the unwrapped samples can be used.

3.4.5 The Double Sides FFT

In the DFT and FFT a real-timesignal is decomposed in harmonic components in the frequency dominion defined by amplitude, phase e frequency. But a real-time signal is decomposed in the complex plain with imaginary and real component, therefore a real signal could be decomposed in two complex vectors each with the half time magnitude, counter rotating with an angular velocity equal to $\pm\omega = \pm 2\pi f$. The FFT algorithm returns as a result of a *two-sided* frequency spectrum with both positive and negative frequencies but only the positive frequency have a real physical correspondence, thus for a *single-sided* diagram with only positive frequencies, the spectrum amplitudes are multiplied by 2, except for the component corresponding at frequency zero that represents the time signal DC (direct current signal). The amplitude scaling allows distributing time domain signal power in the positive frequency on *single-sided* spectrum representation of discrete harmonic components.

Another important consideration is referred to the engineering unit format on which the spectrum results, calculated by FFT are presented for harmonic analysis correlation, to better understand physical behaviours. According to Fourier decomposition, the amplitude of a sine wave can be expressed in the resulting spectrum as RMS or Peak to Peak or 0-Pk. A sine wave analytically is characterized by a fixed relationship between the three-above-mentioned possible formats for the amplitude as reported in fig. 3.8, the choice of the rights format is mainly due to the specific application of the harmonic analysis results. It's important to distinguish the RMS amplitude format from the RMS of a spectrum known also as overall spectrum level. The RMS amplitude format gives useful information about how the equivalent waveform steady state energy for each spectral lines, by the scaling amplitude from peak to RMS equal to 0.707.

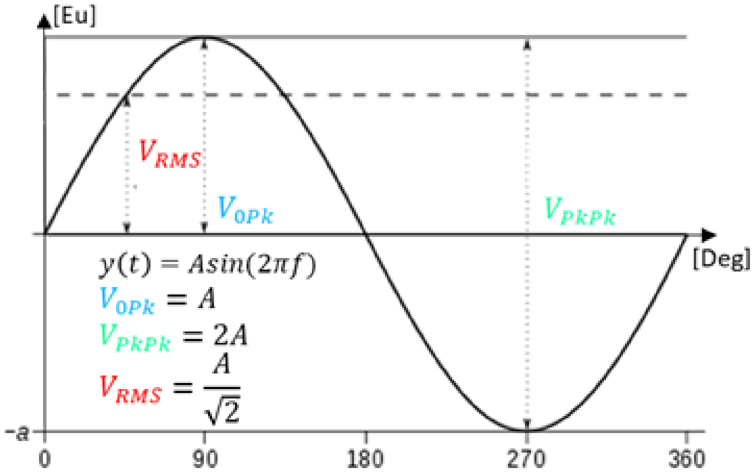

Figure 3.8: sine wave amplitude is shown in RMS, $0pk$ peak, $pkpk$ peak to peak Value

The overall RMS value of a spectrum is the RMS calculate over the entire spectrum interval bandwidth representing overall energy across a frequency range as shown in (3.23), on the other site,the RMS spectrum is a scaling amplitude factor, to represents the same A_i spectrum harmonic amplitudes in one of the three different ways.

$$RMS_{overall} = \sqrt{\frac{A_0^2}{2} + \sum_{i=1}^{k-1} A_i^2 + \frac{A_k^2}{2}} \tag{3.23}$$

There are some important considerations that must be considered to calculate spectrum overall RMS:

1. The data base starting to calculate the overall RMS value must be in the linear format if the spectrum is an auto power *taylor2003vibration* spectrum it must be squared to the linear unit before calculating overall RMS

2. The spectrum starting to calculate the overall RMS, must be composed by spectral lines in RMS linear format.

The overall RMS is a useful spectral parameter to evaluate the signal energy referred to a spectrum frequencies interval, comparing different operating varying conditions. Indeed using STFT approach the signal time history is partitioned into overlapped *time* *section*, when recording a time dependent event, that is changing, it is often preferred to track overall RMS for every increment of time.

On the other site, as indicated in the equation (3.23), all spectral contributes are filled in overall RMS, then also a noise or disturbance components. For this reason is not often used as a reference parameter in FDI algorithm to apply on prognostic precursor, in particular when the FDI methodology considers a comparison between simulated precursors and experimental data in the equivalent operating conditions. Although the proposed simulation model considers noise, the precursors are filtered, and the boundary conditions are designed to avoid disturbances not correlated with the study cases, the driven experimental data could include different harmonic components generating misleading responses.

3.4.6 The Autopower Spectrum, PSD

Autopower Spectrum: In the complex domain the *autopower spectrum* is the product between amplitudes of the frequency spectrum and its complex conjugate, the squared magnitude of the frequency spectrum of all harmonic components. An auto power spectrum is a real number without any phase information lost in the product. The advantage to use *autopower spectrum* respect the amplitude spectrum (described in in the previous paragraph), is the loss of the phase component during the averaging process, avoiding the resulting amplitude being wrong to ensure a meaningful average. Obviously, the averaged results are expressed in Eu^2 with Engineering Unit (Eu) squared, to avoid squared amplitude units, the autopower averages are squared root, so the units could be easier to understand. The frequency resolution has a great impact on the amplitude spectrum calculation, the same time signal presents greatly amplitudes differences increasing amplitude value according to increasing frequency resolution values. Indeed, an increasing frequency resolution is linked to a smaller time section on which performing FFT operation reducing smoothing amplitude evaluation on the spectral component within the considered observation interval.

Power Spectral Density (PSD): The PSD power spectral density is the normalization despite the frequency resolution, so the amplitude level differences are minimized (not eliminated) the corresponding engineering units are squared divided by Hz related with the frequency resolution normalization. The PSD is meanly used for comparison among random broadband signals or for example during shaker testing to quantify fatigue effects created from random vibrations on test articles.

As the frequency resolution gets finer, an example from 10 Hz to 2Hz, more spectral lines are involved to calculate spectrum with the same bandwidth or frequency calculation interval, and equivalent overall RMS. Since the energy signal content in time must be conserved, during the FFT more spectral lines are involved in the spectrum each with lower amplitude than higher *frequency resolution* since, coming from the same time signal, the power is distributed near a wider set of spectral lines as indicated in (3.17).

Therefore the PSD represents the distribution of the average signal power in time over spectrum frequencies For sinusoidal data the concept is opposite, the sine amplitude in an *autopower spectrum* does not vary mainly as function of spectral lines because the signal is focused in main frequencies, in the hypothesis of coherence sampling and linear sine waves combinations. For 400 Hz sine wave even if is transformed by DFT with different *frequency resolution*, puts all signal power in a single spectral line so autopower spectra will have the same amplitude as a function of different *frequency resolution* but presenting PSD with have different amplitude for different *frequency resolution*.

3.4.7 RMS root Main Square

In the previous paragraph of this chapter 3, the RMS root main square calculation is applied on frequency dominion as RMS amplitude scaling for each spectral lines and applied on a frequency bandwidth intervals calculating $RMS_{overall}$. The physical meaning of the general continuous RMS formula reported in (3.24) is the calculation of the average signal energy on a time period. Therefore the RMS calculation is useful also in the time domain even if the signal is sampled by f_s sample frequency because should be useful to calculate RMS in a specific time interval different from *"time section"* that represents the reference time interval by the DFT transformation. The needs to elaborate time RMS with different time interval than the reference *time section* used by DFT are related to the possibility to focus custom time interval on the transient signal part of interest to better understanding a mean energy physical phenomenon otherwise cut off by STFT algorithm. It's important to reaffirm that the spectral leakage is irrelevant on RMS on *time section* since energy evaluation within an STFT the energy calculated on discrete time samples and spectral lines must be equal, for Parseval theorem in discrete form as reported in (3.25), where N is time samples and m are number of spectral lines.

$$x_{rms}(t) = \sqrt{\frac{1}{T_2 - T_1} \int_{T_1}^{T_2} [x(t)]^2 \, dt} \tag{3.24}$$

$$x_{rms}(N) = \sqrt{\frac{1}{N} \sum_{N} x[N]} = \sqrt{\sum_{m} \left| \frac{x[m]}{N} \right|^2} \tag{3.25}$$

The above-mentioned property descends from decoupling from time domain e frequency domain linked by FT Fourier transformation and related STFT approach.

Chapter 4

FDI Methodology for Rotor Static and Dynamic Eccentricity

4.1 The Main Elaboration Process

The proposed FDI prognostics methodology based on harmonics analysis fundamentals considers the electrical brush-less motor as the *"itself sensor"*, able to detect early failure path for a different type of failures. Since having an increasing impact on the interaction among mechanical behaviour, electrical supply circuits, and magnetic coupling between rotor and stator. The complexity of the EMA numerical high-fidelity model is described, for each main simulation block, in chapter 2.3.3 from page 39. The proposed methodology is based on a robust model-based approach, to simulate properly the chosen prognostic precursors, represented by filtered stator phase currents, under specific boundary conditions described in 3.1.

The boundary conditions are proposed with the main goal to define best requirements, to perform both the simulations under incipient and improving types failures and the real ground test on aircraft 3.1. The comparison between "model-based" failure maps, defined with the methodology described in this chapter, and the "data-driven" approach, coming from aircraft ground test, could improve accuracy by detecting the health state of the primary flight control system, without a too invasive hardware sensors frameworks, minimizing the post-processing algorithms weight performed by avionics modules.

Normally, simulation accuracy and algorithms complexity are antithetical aspects for all *"model-based"* approach referred to the elaboration efforts required by a comparison system on aircraft avionics system, especially for harmonic analysis algorithms. The time-frequency transformations are a wide functions class, described analytically by Cohen class formulation [20], to improve efficiency reducing the calculation effort for harmonic analysis,based on STFT short time Fourier transformation in discrete form. The FFT algorithms are used to solve the STFT approach, improving efficiency for calculating Fourier coefficients and related spectral diagrams, since in the last forty years the FFT is employed on several industrial, application related to vibration and acoustic study as in [31]. Other time-frequency transforms as wavelet, are developed to study transient and not stationary time signals without the STFT limits, but they require more complex computational efforts for example Wigner Ville transformation requires additional ambiguity functions to reduce the impact of cross terms note directly related to the physics of the problems but related to analytical form. After an attention assessment among the most used time-frequency transformations, in different prognostic applications, the STFT with FFT algorithms are a compromise results between advantages and disadvantages on the practical proposed application.

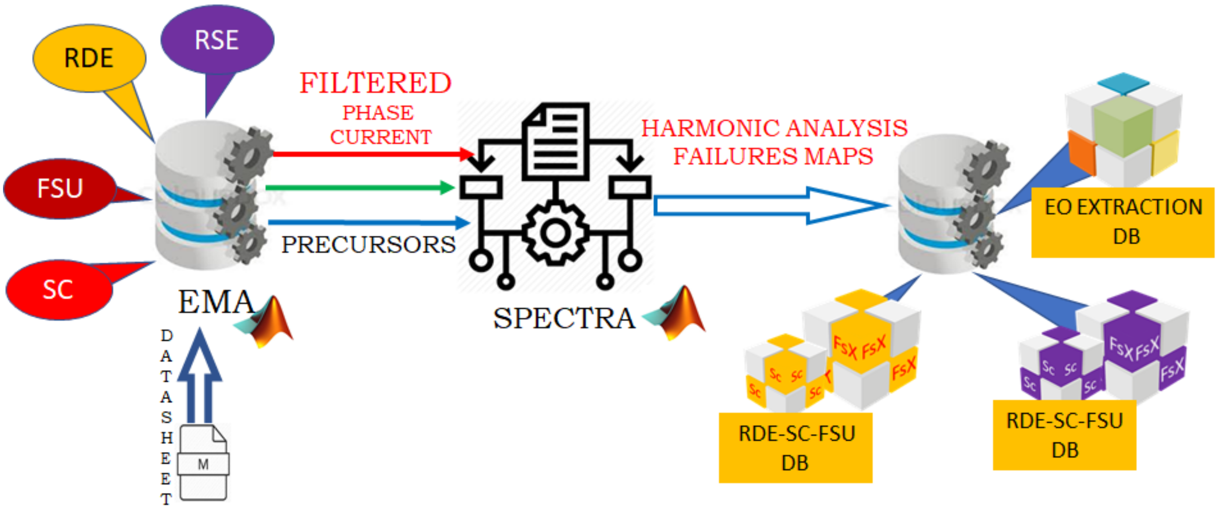

Figure 4.1: High Level FDI proposed method representation with all considered type of failures: RSE Rotor Static Eccentricity RDE Rotor Dynamic Eccentricity SC Short Circuit *"Turn To Turn"* and FSX friction variable condition

The proposed method is illustrated at a high level on fig. 4.1, where are applied fixed BC simulation boundary conditions and defined technical parameters referred to an EMA data sheet, inclusive of real actuator technical parameters and simulation parameters (cut off frequency filter values, failures model parameters etc...). The EMA model generates a time history for prognostic precursors I_a, I_b, I_c, on which a second *MATLAB* script modulus called *"Spectra"* perform with specific settings the FFT generating a data collection of spectrum diagrams. Recognition and analysis logics are applied to each data collection database to detect the health state of the system as a function of the progressive path for different failure types acting in concurrent mode on the same set of prognostic precursors. It should be noted, as reported in [14], that this fact is not in itself obvious, because these failures generate contrasting effects on the adopted prognostic parameters (i.e. stator phase currents) that, sometimes, they could hide one each other. Other model-based FDI methods presented in the literature, implement FEM analysis and/or statistical methodology, interactively computed up to the convergence of suitable fitness functions (e.g. L1-norm or L2-norm error), to evaluate the EMA health status

[62]. Therefore, the proposed method performs an early FDI analysis by calculating in off-line mode, and comparing with failure maps a real-time prognostic precursors acquisitions during aircraft ground test as described in 3.1.

The FFT results are elaborated following three spectral numerical approaches able to define from a different point of view about the system dynamic firms with the aim to understand the system health state:

1. Magnitude track: this approach is based on tracking amplitudes for both main harmonics in the frequency domain and in the time domain by using RMS of the precursors time signal.

2. Frequency track: this approach is based on tracking main harmonics in spectral diagrams within the fixed bandwidth, by applying peak hold filter defining different dynamic system firm.

3. Engine order extraction: this approach is based on synchronous sampling on precursors time signal extracting the amplitudes of the engine orders (exciting oscillation causes a function of the rotation speed values) as a function of the increasing mechanical wear.

The above-mentioned approaches are the support for a decision-making logical process applied on model-based results, coming from simulation and post-processing harmonic analysis, that generates different database categories specialized for failure interaction on prognostic precursors time signals.

4.2 *RSE* Magnitude Track

The RSE physical phenomenon described in 2.3.3 by the main misalignment between rotor rotational centre and stator geometrical centre, that during healthy operating condition without misalignment generates a symmetrical magnetic field among supplied stator coils and permanent magnetic rotor poles. Therefore, RSE is associated with a misalignment of the magnetic field along EMA cross-section, as in 4.2, generating the Maxwell tensor radial stresses resultant not null applied to the rotor by the airgap reduction.

4.2.1 Maxwell Electromagnetic Tensor

In many bibliographic sources, the Maxwell tensor is defined as symmetric second-order tensor representing the interaction between electromagnetic forces and mechanical momentum. In other words, the radial stress component δ_n expressed in (4.1), where μ_0 is the vacuum magnetic permeability, is generally defined as the normal electromagnetic force between stator and rotor expressed per surface engineering unit, considering the surface the normal surfaces on stator and rotor cross by field lines of magnetic

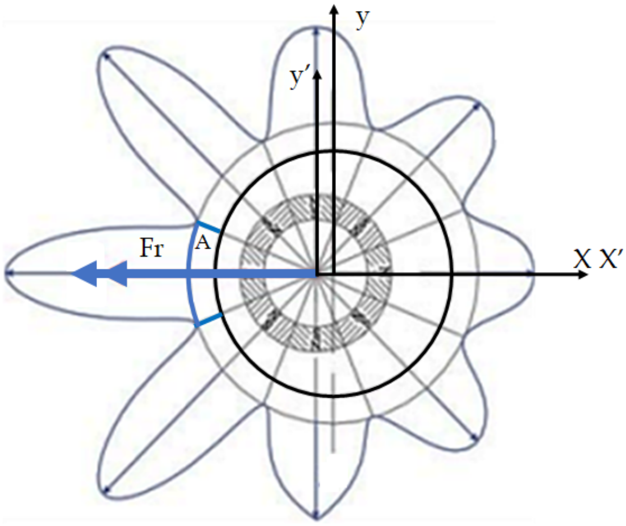

Figure 4.2: Qualitative magnetic field distribution on the EMA cross-section affected by RSE rotor static eccentricity, and the related F_r Radial Force resultant;

induction density flux $\boldsymbol{B}$, with sine amplitude modulation and two components: neglected tangential component $\boldsymbol{B}_\theta$ e radial component $\boldsymbol{B}_n$ If the magnetic field is symmetric the magnetic stress field is symmetric with null resultant as expressed in (4.2) under rotor and stator concentric, and uniform and isotropic air-gap hypotheses. This last hypothesis neglects slotting effects due to the space among caves and teeth geometry, the magnetic flux follows the minor reluctance adding other harmonic components on the sinusoidal flux induction waveform.

$$\sigma_n = \frac{\boldsymbol{F}_n}{\boldsymbol{S}} = \frac{\boldsymbol{B}_n^2}{2\mu_0} \tag{4.1}$$

$$\boldsymbol{F}_x = \int_0^{2\pi} \sigma_n(\theta, t)\cos\theta \, d\theta = \boldsymbol{F}_y = \int_0^{2\pi} \sigma_n(\theta, t)\sin\theta \, d\theta = 0 \tag{4.2}$$

The rotor bearings wear progressively improve the RSE changing magnetic symmetry and affecting the spatial distribution of the radial magnetic induction field $\boldsymbol{B}_n$, function of maximum magneto-motive force $\boldsymbol{M}_1$, with pair poles $\boldsymbol{P}_p$, starting from air-gap equation (2.13), and substituting the last member of (4.3) in the first member of (4.4).

$$\frac{1}{g(\theta)} \cong \frac{1}{g_0}\left[\frac{\zeta - 2\cdot\left(1-\sqrt{1-\zeta^2}\right)}{\zeta\sqrt{1-\zeta^2}}\cos\theta\right] = \frac{1}{g_0}\left[A_0 - A_1\cos\theta\right] \tag{4.3}$$

$$B_n(\theta, t) = \frac{\mu_0 M_1}{2}\cos\left(\omega t - P_p\theta\right)\frac{1}{g(\theta)} = \frac{\mu_0 M_1}{2g_0}\cos\left(\omega t - P_p\theta\right)\cdot\left[A_0 - A_1\cos\theta\right] \tag{4.4}$$

The (4.4) represent magnetic induction field B affected by RSE associated to misalignment between rotor and stator rotation centre, applying prosthaphaeresis trigonometric identities the main induction field is represented by interaction of three harmonics with a different number of pair poles P_P around differences of one integer as in (4.4).

The integration on angular dominion the related σ_n associated to magnetic induction field in (4.1) gives a not null resultant with a radial force directed in the minimum reluctance $\Re$ direction.

$$B_n(\theta, t) = B_1 cos\left(\omega t - P_p \theta\right) - B_2 cos\left(\omega t - \left(P_p - 1\right)\theta\right) - B_2 cos\left(\omega t - \left(P_p + 1\right)\theta\right) \tag{4.5}$$

$$B_1 = \frac{\mu_0 M_1 A_0}{2 g_0} \tag{4.6}$$

$$B_2 = \frac{\mu_0 M_1 A_1}{4 g_0} \tag{4.7}$$

4.2.2 *RMS* Failure Maps

The EMA simulation model is performed with the step command at a high value to saturate control loop producing open loop dynamic response therefore the user (aerodynamic surface) gain the maximum no-load velocity in the minimum simulation time of one second interactively for each RSE value ζ from 0% to 50%.

This RSE percentage interval is considered up to 50% as the maximum allowable misalignment in all the presented work, the higher air-gap reduction could have catastrophic consequences on flight safety considering that BLDC motor has indicative air-gap from 0.3 to 3 mm. The first presented failure maps consider for each filtered stator supply phase current I_{fA}, I_{fB}, I_{fC} an RMS value calculated processing the rotor static eccentricity values from 0% to 50% with 1% RSE increasing step; the results are three signals, called $I_{a_{RMS}}$, $I_{b_{RMS}}$ *and* $I_{c_{RMS}}$, evolving as shown in fig. 4.3.

Describing the RMS trend for each prognostic precursor in fig. 4.3, it is evident that I_a phase is affected by the RSE minimum air-gap since it requires less electric power than the other two ones, reaching and maintaining the actuator maximum speed, associated to minimum reluctance $\Re$. Moreover, the difference between $I_{a_{RMS}}$ and $I_{c_{RMS}}$, taken as a reference, increases more and more with increasing eccentricity while $\Delta I_{b_{RMS}} I_{c_{RMS}}$ remains almost constant in all considered RMS range.

Progressive eccentricity causes progressive asymmetry of the magnetic field so the RMS filtered phase current values increase and, the actuation speed decreases as in [12]. The RMS calculation based on one second time interval, for each filtered phase current, could be mediated defining a failure maps to perform an EMA health conditions evaluation exposed in fig. 4.4 on following qualitative eccentricity percentage as in [10]:

1. **Green Phase**: from 0% to 10% of the rotor static eccentricity (with respect to the stator-rotor air gap); this operating interval corresponds to **Normal Mode** with

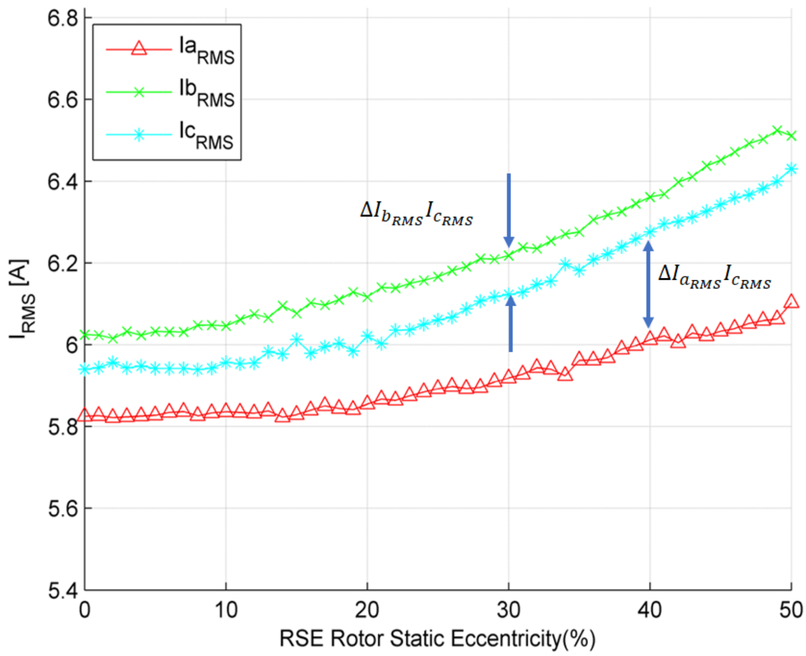

Figure 4.3: RMS evolution for three filtered phase current as a function of ζ, RSE rotor static eccentricity, each time RMS point is calculated on one second simulation;

acceptable actuator performances; it is related to a negligible static eccentricity, mainly due to tolerances of manufacturing and beginnings of mechanical wear. It must be noted that, respect to reference value mean RMS on 0% RSE static eccentricity, this green phase has a wide interval of 16 mA;

2. **Orange Phase**: from 11% to 26% of the rotor static eccentricity percentage; this operating interval corresponds to **Moderate Mode** with actuator performances related to incoming evaluable command degradations. Respect to reference value on 11% RSE static eccentricity this phase has a wide interval of 100 mA;

3. **Red Phase**: from 27% to 33% of the rotor static eccentricity; this operating interval corresponds to **Serious Mode** where actuator performances are degraded and condition-based maintenance operations need to be planned. Respect to reference value on 27% RSE static eccentricity, the red phase has a wide interval of 60 mA;

4. **Violet Phase**: from 34% to 50% of the rotor static eccentricity; this operating interval corresponds to **Extreme Mode**. In this case the actuator performances are very degraded and the based maintenance operations are needed as soon as possible. Respect to reference value mean RMS on 34% static eccentricity, this violet phase has a wide interval of 200 mA;

The RMS value, as RSE function for each phase precursor, gives a first evaluation of the energy that may occur to reach the maximum actuator speed. This approach could

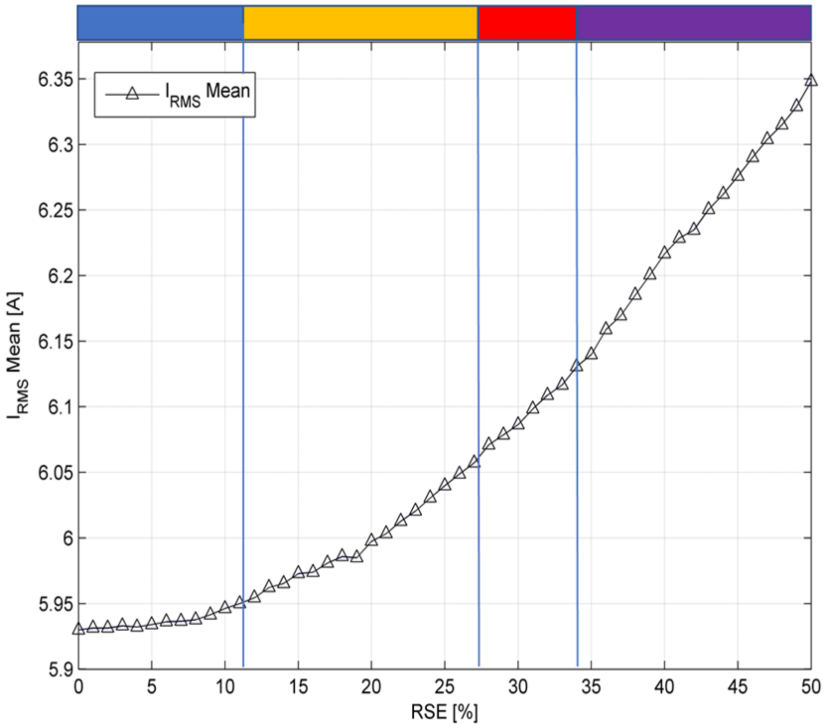

Figure 4.4: RMS mean evolution based on RMS of three filtered phase currents as a function of ζ, on the graph are identified 4 main evaluation health actuator states;

give only qualitative feedback by comparison with the same RMS calculated on the same time interval at real acquired precursors. Because of many causes and different failure types could generate increasing supply energy with actuation speed reduction like improving friction coefficient, due to inefficiency lubrication. However, this failure map represents a baseline on which it's possible to improve accuracy by integrating RMS trend with harmonic analysis results structured as maximum magnitude harmonic track and frequency track approach.

4.2.3 Maximum Magnitude Harmonic

The above-mentioned sine wave equations, referred to magneto-motive force and magnetic induction, consider as oscillation frequency the motor supply frequency as main harmonic, but in a PWM the coils supply current are results of voltage impulses with different time widths. Therefore to detect H_{max} the main supply maximum magnitude harmonic, an STFT approach is used by applying FFT. The STFT is performed by defining the DSP parameters starting from the integration time step used in Simulink, fixed to $10e^{-6}$ and assumed as the sample rate of the simulated physical variables used as prognostic precursors. Coming from this baseline, the DSP parameters are in relation to

Eq. (3.17) on page 65, observing the precursors time signal the first main DSP parameter to choose is the time section. The time section governs the N block size, Sl the number of spectral lines, representing the Δf inverse of the frequency resolution. Another fundamental parameter, to perform STFT is the time windowing function, described in 3.3.4, since everything else being equals to DSP parameters and the input signal, the windowing produces effects on spectral amplitudes. Digital signal processing performed, to better understand the best solution for the FDI algorithm, is the results of a robust assessment observing the main waveform characteristic in the time domain over one second of simulation.

Results assessment is conducted considering more significant information, coming from the harmonic analysis performed on STFT approach, considering that at fixed very high sample rate the physical behaviour of the simulated prognostic precursor allows precise discrete reproduction of the time function. The set of DSP coming from different combinations, during the assessment process, are indicated in fig. 4.1 on reference to which the harmonic results are calculated. The overlap between the partitioned time section extracted from the time signal is a compromise between the amplitude smoothing windowing effects on the extremes and the increasing number of spectra calculated on fixed simulation time.

Table 4.1: DSP digital signal parameters used to perform STFT for Harmonic analysis

DSP Parameters	Value	Engineering units	Description
f_s	10^{-6}	[Hz]	Sample Rate
Δs	0.25	[s]	Time Section
Δf	4.00	[Hz]	Frequency Resolution
N	250	[KSa]	Block Size
Sl	125	[Kbins]	Spectral Lines or Bins
bdw	390	[KHz]	BandWidth
Windowing	Hanning	Na	Type Windows Function
Interpolation Bins	5	[#]	Spectral Bins for peak Interpolation
Overlap	67%	[#]	Overlap superposed Time sections

Diagram 4.5 shows the H_{max} maximum amplitude harmonic as a function of increasing RSE rotor static eccentricity with an incremental step of 1%. The maximum magnitude harmonic is extracted as a result of a *peak hold function*, where by a comparison of each calculated spectrum extracts the maximum amplitude for each frequency value. Therefore the diagram 4.5, expressed in Ampere Peak versus ζ or RSE percentage, shows the maximum amplitude among peak hold magnitudes extracted from FFT spectra.

$$H_{max} = A_{max}(\zeta) \cdot \cos\Big(2\pi f_{PKmax} \cdot t\Big) \tag{4.8}$$

The H_{max} trend is correlated with magnetic induction flux in (4.5), as a function of the air gap affected by increasing misalignment. Interaction of the three harmonics on which is made up, determine the H_{max} trend, where the *"Critical Event"* representing the global minimum value at 33% RSE. The first diagram zone from 0% to 18% represents H_{max}

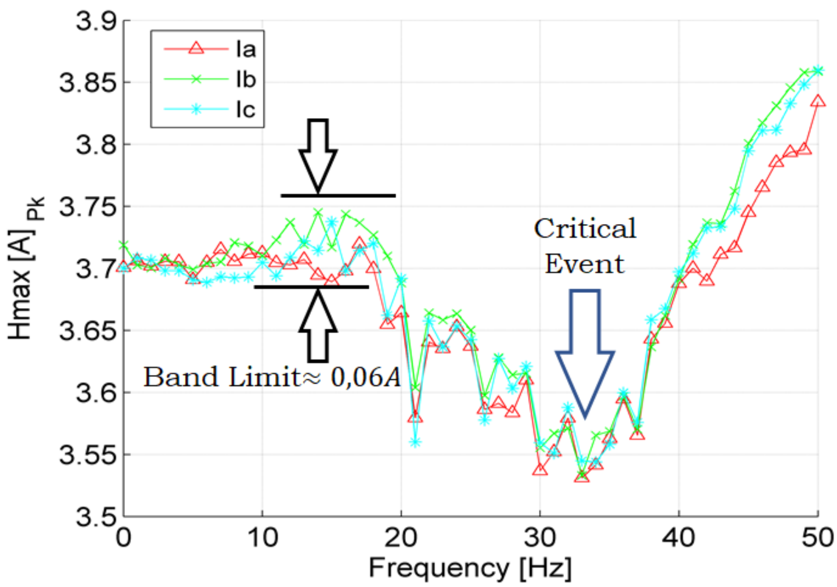

Figure 4.5: Maximum Amplitude FFT harmonic evolution as a function of RSE percentage

quite constant for each prognostic precursors, the corresponding peak values are limited in amplitude band with a maximum value of 0.06 A (respected band limit for all H_{max} diagram). The second main zone starts from 19% to 33% RSE representing the descending trend from the quite constant mean value of the previous zone at 3.72 A to global H_{max} minimum value at 3.533 A corresponding to "Critical Event". The third diagram zone starts from 33% to upper study limit of 50% RSE percentage, with an increasing amplitude trend up to the maximum value. Above mentioned diagram zones, based on the trend of three-phase max magnitude harmonic, could improve with further information the qualitative RSE estimation coming from time RMS failure maps by fig. 4.5 adding the important information about the *"new Warning Event"* placed at 18% RSE the beginning of descending H_{max} trend [12].

4.3 RSE Frequency Track

In the previous paragraph H_{max} magnitude is tracked overall RSE study interval with 1% increasing step, but the frequency of the main harmonic with the maximum amplitude changes at *"CriticalEvent"* at 33% RSE percentage. Indeed over this RSE event the magnetic induction field change energy harmonic distribution and new frequency $H_{max}^{new} = 32.805$ Hz takes place to $H_{max} = 33.568$ Hz with a difference of $\Delta f_f = 0.763$ Hz for main shifting frequency. This information is significant to analyze deeper the pick hold function results able to improving accurate detection of the health state related to RSE rotor dynamic eccentricity distribution. Further analysis shows that the peak hold diagram could refine the correlation between harmonic analysis and incipient failure due to wear for RSE. The peak hold function calculates for each spectrum the maximum value for all spectral lines, the only the first five peaks are extracted. Each filtered phase current presents different harmonic configurations but with acceptable accuracy each peak hold extraction, for increasing misalignment percentage, could represent a significant dynamic firm associable with a failure path percentage with low ambiguity.

From *peak hold* diagram it can be seen that current harmonics appear as an integer multiple of the H_{max} maximum magnitude frequency, also considering that over *"Critical event"* H_{max}^{new} takes place on H_{max} as reference for some *"shifted"* harmonics up to 50% RSE. The main H_{max} harmonics are enlightened on graph 4.6.

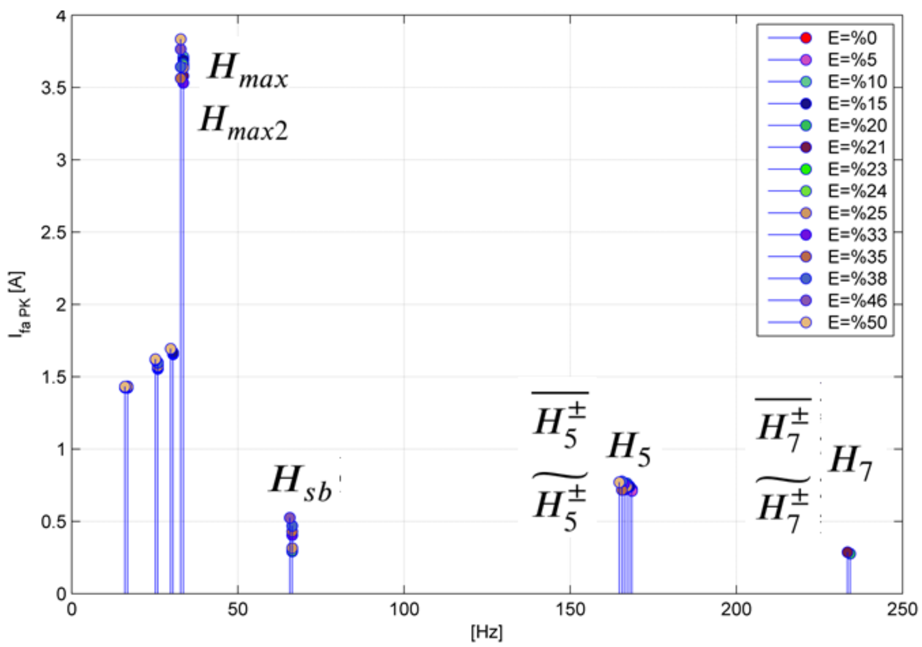

Figure 4.6: Peak Hold Diagram for the first 5 peaks of maximum magnitude, for filtered phase current I_{f_a} as a set of some RSE percentages

$$H_2 = A_2(\zeta) \cdot \cos\Big(2\pi \cdot 2f_{PKmax} \cdot t\Big) = H_{sb} \tag{4.9}$$

$$H_5 = A_5(\zeta) \cdot \cos\Big(2\pi \cdot 5f_{PKmax} \cdot t\Big) \tag{4.10}$$

$$H_7 = A_7(\zeta) \cdot \cos\Big(2\pi \cdot 7f_{PKmax} \cdot t\Big) \tag{4.11}$$

Within the current harmonics, a particular harmonic called H_{sb} equal to $2X\ H_{max}$ frequency, appears on peak hold extraction of the first 5 magnitude peaks, form 23% RSE, with the interesting characteristic of quasi-linear monotone increasing value, as a function of RSE percentage. Therefore a frequency track filtering on calculated spectra fixed at H_{sb} frequency could give a fine evaluation of the RSE path starting from 23% percentage. It could be noted that H_{sb} is not available on *peak hold* diagram for RDE rotor dynamic eccentricity, therefore this harmonic is only influenced by increasing friction coefficient but still remain quite linear with RSE incipient failure.

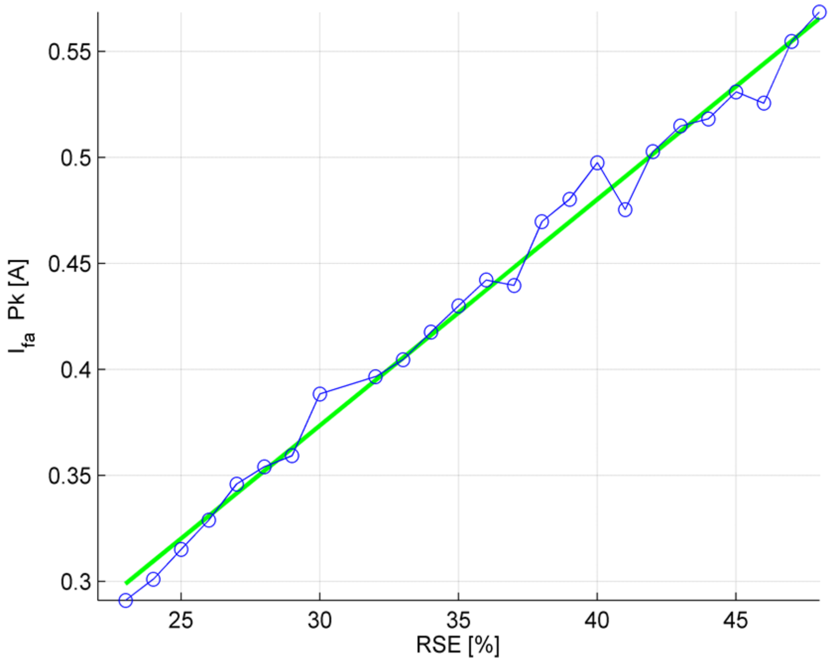

Figure 4.7: Peak Hold Diagram for H_{sb} amplitude unbalancing harmonic with frequency equal to 2x H_{max} frequency for filtered phase current I_{f_a} as RSE percentages function

Analyzing *peak hold* filter on spectra with different misalignment percentage in 4.2 on page 93, it is apparent that not only integer harmonics emerged but from 19% RSE some *"shifted harmonics"* take place on the graph.

However, coming from the peak hold analysis, the 19% RSE percentage is near the previous *"new warning event"* at 18% RSE, coming from descending trend analysis on graph 4.3, therefore the two approaches define the same physical event.

$$\overline{H_7^{\pm}} = \overline{A_7}(\zeta)\cos\Big(2\pi(7f_{PKmax} \pm \Delta f_f)t\Big) \tag{4.12}$$

$$\widetilde{H_7^{\pm}} = \widetilde{A_7}(\zeta)\cos\Big(2\pi(7f_{PKmax} \pm 2\Delta f_f)t\Big) \tag{4.13}$$

$$\overline{H_5^{\pm}} = \overline{A_5}(\zeta)\cos\Big(2\pi(5f_{PKmax} \pm \Delta f_f)t\Big) \tag{4.14}$$

$$\widetilde{H_5^{\pm}} = \widetilde{A_5}(\zeta)\cos\Big(2\pi(5f_{PKmax} \pm 2\Delta f_f)t\Big) \tag{4.15}$$

Shifted harmonics are defined from integer reference current harmonics adding or subtracting the same discrete frequency value of Δf_f, or its integer multiple. This result is very interesting because it improves the frequency track algorithm able to assign for each harmonic or shifted harmonics combination, a specific RSE percentages range with a low ambiguity margin not well covered by magnitude track approach.

A second important added value, coming from *peak hold* diagrams, is progressive changes on air-gap, to the main direction of supply current I_A, affecting the energy distribution on main harmonics in discrete mode. Indeed shifted frequency harmonics are shifted by integer discrete frequency interval of $\Delta f_f = 0.763 Hz$ for all supply filtered currents. The frequency track approach is based on harmonics and *shifted* harmonics with multiple frequencies of the maximum magnitude frequency H_{max} (33.568 Hz) and H_{max}^{new} (32.805 Hz) neglecting the frequency components in peak hold extraction lower than H_{max}^{new}, because real acquisition test on the ground could be affected by low frequency disturb components. Therefore the *peak hold* lower frequency components than H_{max} are considered not effective to the main comparison process between simulated and real post processed signals. The main maximum amplitude harmonic H_{max} presents the same frequency for all supply filtered phase currents, and after *Critical Event* changes into H_{max}^{new} as consequence from 34% RSE H_{max}^{new} frequency become reference value for *shifted harmonics*, for peak hold extraction (also for H_{sb} unbalancing harmonic) up to the RSE upper study limit. The discrete shifting about H_{max} frequency to H_{max}^{new} of (33.568 Hz), is coherent with valuable rotor speed velocity that decreases for each misalignment improvement, consequently related to reducing phases commutation speed logic.

4.4 RDE Magnitude Track

The RDE rotor dynamic eccentricity, as previously described in 2.3.4, is another type of eccentricity related to unbalanced magnetic pull due to the main misalignment between rotor rotational centre and stator geometrical centre. In the disposition of this geometrical component, the magnetic field along EMA circumference, as shown in 4.8, generates in correspondence of minimum air gap a radial force coming from Maxwell tensor forces. Considering EMA in a cross-section plane, but unlike static study case, the minimum air-gap changes position on stator angular reference system, generating a radial stress resultant not null rotating with angular speed Ω. Real value of the rotation speed is fixed in first approximation at 44% of rotor speed its rotational axis, it could be not constant due to non linear lubrication efficacy effects, neglected in the proposed numerical model even if a tribological friction model is considered to improve simulation framework accuracy.

4.4.1 Maxwell Electromagnetic Tensor

Proposed RDE numerical model is based on a dynamic model equation (4.16) of the air-gap derived from cinematic cross-section schema in 2.21 and the related impact on the counter electromotive force model.

$$g(\theta, t) \cong g_0(1 + \zeta \cos(\theta - \Omega t)) \quad where\ \zeta = \frac{x_0}{g_0} \tag{4.16}$$

The Maxwell radial stress tensor component σ_n is proposed as a time function of new

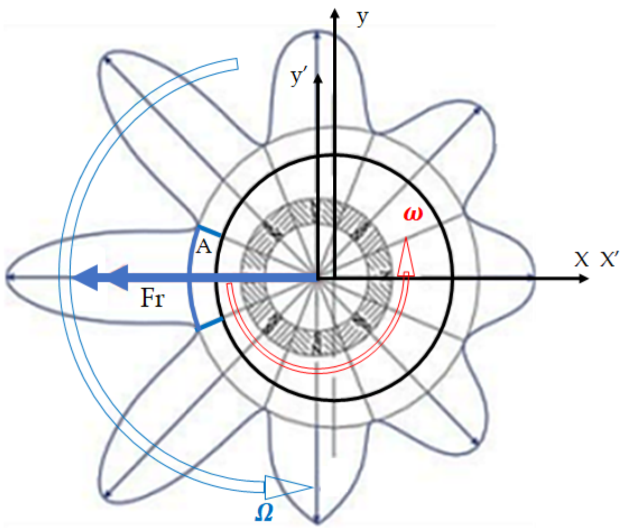

Figure 4.8: Qualitative magnetic field distribution on EMA cross-section affected by RDE rotor dynamic eccentricity, and the rotating F_r Radial Force resultant;

air gap formulation $g(\theta, t)$ in 4.16, and in the first approximation is related to radial magnetic induction field B_n in (4.1) and μ_0 vacuum magnetic permeability. The radial magnetic induction field B_n in (4.4) changes in (4.17) where air-gap is a time function not only a θ function then the coefficients A_0 *and* A_1 are not time constant function of ζ. Therefore changes, in the formulation of magnetic induction flux B_n, are not any more decomposed as in (4.5), by main harmonics with constant time coefficients, but a new harmonic configurations with time dependent coefficients B_1 *and* B_2.

$$B_n(\theta, t) = B_1 cos\left(\omega t - P_p\theta\right) - B_2 cos\left(\omega t - \left(P_p - 1\right)\theta\right) - B_2 cos\left(\omega t - \left(P_p + 1\right)\theta\right) \tag{4.17}$$

$$B_1 = \frac{\mu_0 M_1 A_0(t, \zeta)}{2g_0} \tag{4.18}$$

$$B_2 = \frac{\mu_0 M_1 A_1(t, \zeta)}{4g_0} \tag{4.19}$$

4.4.2 *RMS* Failure Maps

In the same simulation boundary conditions, considered for the RMS failure map elaborated for RSE, the maximum allowable misalignment is up to 50% also in dynamic eccentricity. The second time RMS failure map is showed in 4.9 with 1% RDE increasing step. Describing the time RMS trend, for each prognostic precursors, filtered phase I_a is angular starting point with the minimum air-gap, requiring less electric power to reach and maintain the maximum rotor speed associated with minimum reluctance $\mathfrak{R}$. Although, from the starting point fixed by boundary conditions, the minimum air-gap rotates with precession velocity Ω, equal to 44% of rotor speed ω, the phase I_a presents mainly minimum time RMS trends as a function of increasing RDE percentage during the simulation time fixed at 1 s. Rotor centre rotation affects the time RMS trend with less accentuate slopes than RSE behaviours, needed energy more distributed among the supply current phases. Indeed globally the energy requested by increasing misalignment is more equally distributed among three supply currents by the rotor centre rotation during the simulation time of one second, reaching the maximum actuator rotor speed. Moreover, the relative RMS values differences between phase current I_a, I_c took as reference current, and I_b are not divergent as a function of RDE percentage compared with 4.4 RSE study case. As previously described the proposed failure time RMS maps subdivided in different evaluation zones as in 4.4, had only a high level estimation value for EMA health state monitoring. The detailed description, of time RMS evaluation zones in 4.2.2, has the same approach used for RDE giving only qualitative feedback by comparison with real acquisition data.

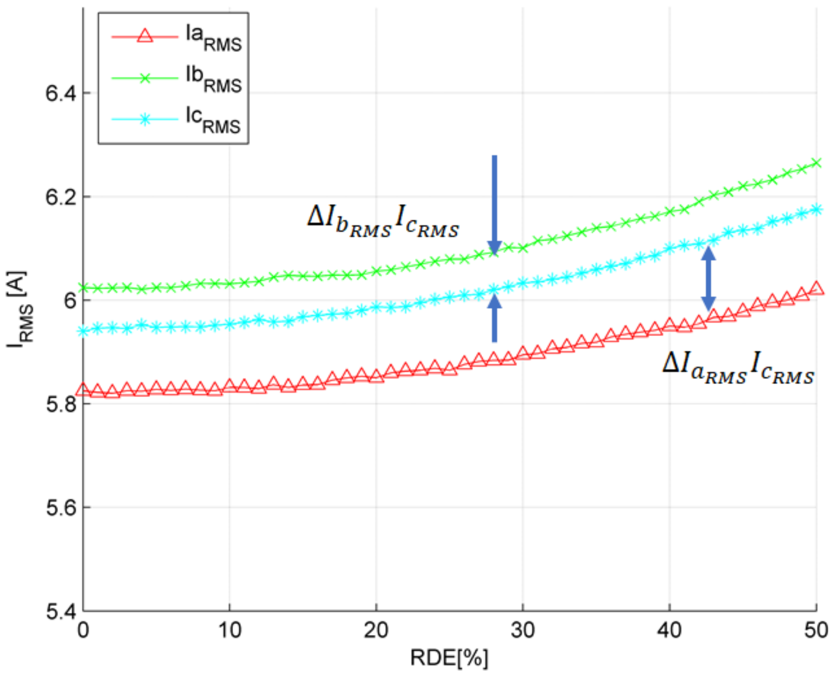

Figure 4.9: RMS evolution for three filtered phase current as a function of ζ, RDE rotor dynamic eccentricity, each time RMS point is calculated on one-second simulation;

4.4.3 Maximum Magnitude Harmonic

The prognostic precursors are analyzed in the frequency domain by STFT short time Fourier Transformation approach, based on DSP digital signal processing parameters defined in 4.1. Therefore the same digital signal processing parameters are used on prognostic precursors improving the comparison between RDE and RSE about failure maps derived by harmonic analysis and timeRMS qualitative approach.

Diagram 4.11 shows the H_{max} maximum amplitude harmonic as a function of increasing RDE rotor dynamic eccentricity with an incremental step of 1%. The maximum magnitude among harmonic components is extracted as a result of *peak hold function*, where (by spectra comparison) extracting the maximum amplitude for each frequency value. Therefore the diagram 4.11, expressed in Ampere Peak versus ζ or RDE percentage, shows the H_{max} maximum amplitude among peak hold magnitudes.

The three main harmonics in which it has been divided the radial magnetic induction flux B_n in (4.17), generate the H_{max} trend for RDE displayed in 4.11, presenting main differences by comparison with *RSE* H_{max} in 4.5. Although the first diagram zone represents a quite constant H_{max} value, for each prognostic precursor near the same mean of 3.72 A similar toRMS trend, the extension is wider from 0% to the *"Critical Event"* identified on 33% RDE. The H_{max} behaviour is due mainly to the airgap rotation during the fixed simulation time, and in all diagram evolutionH_{max} for each prognostic precursors, is limited within an amplitude band with a maximum value of 0.03 A.

Unlike *Critical Event*, meaning in H_{max} RSE failure, within RDE evaluation this event is defined with the descending slope of H_{max} characteristic as increasing misalignment percentage up to the upper limit of 50%, considering global minimum at 49% RDE with 3.524 A. Above mentioned diagram zones, based on trend of three-phase max magnitude harmonic, could improve with further information the qualitative RDE estimation coming from timeRMS failure maps by 4.11 as RSE function adding the important information about the *"Critical Event"* placed at 33% *RSE* the beginning of descend H_{max} trend.

4.5 RDE Frequency Track

The H_{max} amplitude track diagram 4.11, gives less information than homologous magnitude track approach in RSE, because the rotor minimum air-gap rotation affects three current phases during simulation fixed time during both speed transient and maximum speed running. Analyzing H_{max} frequency is the same with fixed misalignment in stator angular position, but even if at 33% is detected as *"Critical Event"*, in RDE main H_{max} frequency doesn't change. The main cause is indirectly related to rotor centre rotation and the energy requested by supply phases. Indeed the commutation supply poles speed is reduced with increasing eccentricity, but the speed interval between

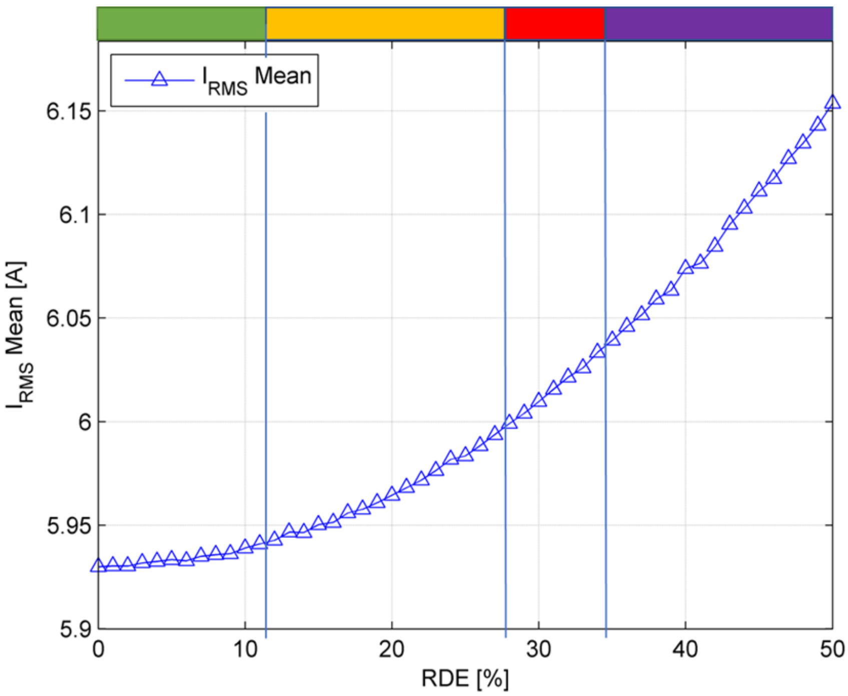

Figure 4.10: RMS mean evolution based on RMS of three filtered phase current as a function of ζ, on the graph are identified 4 main evaluation health actuator state;

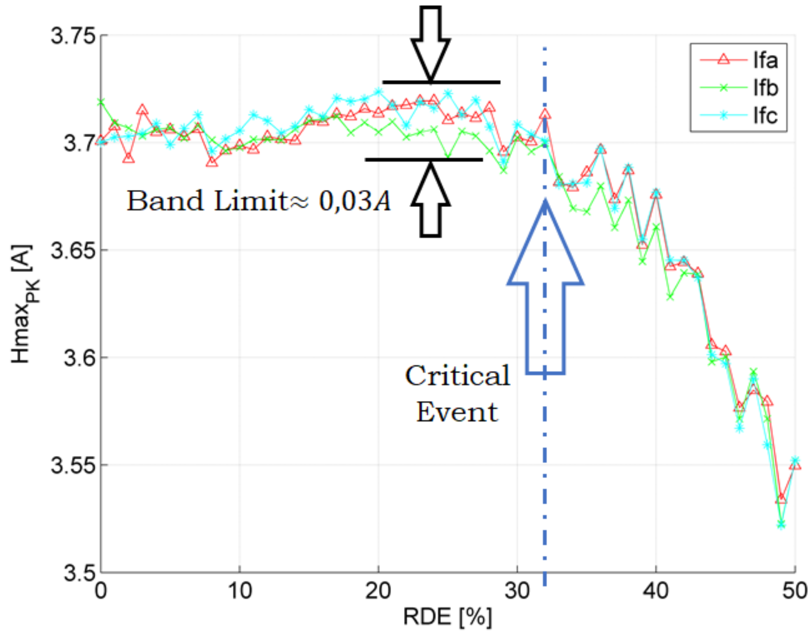

Figure 4.11: Maximum Amplitude H_{max} evolution as a function of RDE percentage

$0\% \div 50\%$ during RDE condition is $72\,rad/s$ versus $15\,rad/s$ in RSE failure condition.

Introducing peak hold filter, on all calculated spectrum coming from simulation time history, it is possible to improve information about the main harmonics, as related *shifted harmonics*, by extracting the maximum value for each spectral lines. Among the peak hold selection, only the first 5 peaks are considered in diagram 4.12, to define a failure frequency mapping in table 4.3 on page 94 for each air-gap reduction percentage.

The first evidence on *peak hold* analysis for RDE concerns the poor presence of H_{max} integer harmonics, because only H_5 and *shifted* harmonics $H_5 + \Delta f_f$ are evaluable on 5 peaks filtering. After the first interval from 0% to 9% with $H_5 + \Delta f_f$ on all filtered currents, starting from 10% integer harmonics higher frequency than H_{max} are evaluable only for prognostic precursor I_{fc} until 23% (with exception of 20% where no higher harmonics respect H_{max} are present within the peak hold diagram). This particular behaviour is due by boundary conditions and the phase current poles geometrical disposition in stator caves, indeed the starting minimum air gap is placed in correspondence of phase I_{fa} therefore in one simulation second the phase I_{fc} is interested in a variable air gap time function that generates a filtered phase current affected by this harmonic and the related *shifted* harmonics with $\Delta f_f = 0.763\,Hz$.

Although the air gap reduction equal to 23% is a particular event both in RSE (with Hsb within peak hold first 5 peaks) and RDE, in dynamic eccentricity this is the last percentage with *peak hold diagram* without components with a frequency higher than H_{max} frequency up to the 50% eccentricity percentage.

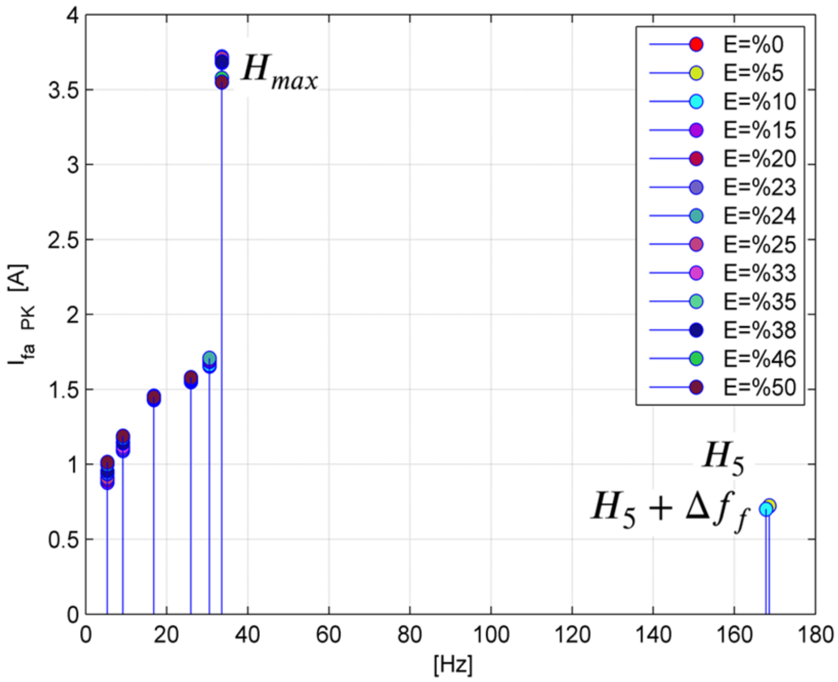

Figure 4.12: Peak Hold Diagram for the first 5 peaks of maximum magnitude, for filtered phase current I_{f_a} as a set of some RDE percentages

The differences between peak hold mapping in RSE and RDE are evident but integrating with H_{max} versus eccentricity percentage ζ diagrams (or H_{sb} for RSE), it is possible to distinguish and evaluate the type of failures and misalignment percentage with acceptable accuracy. Uncertainty margins for RSE is quantified around RSE 3 percentage steps and RDE 7 percentage steps, considering that in RDE are not evaluable a harmonic like H_{sb} proportional to eccentricity percentage, On the other side, during RDE evolution the H_{max} magnitude from 33% to 49% could be estimated inversely proportional to increasing misalignment if the harmonic amplitudes are linearly interpolated by minimum quadratic interpolation straight line. In the proposed FDI algorithm, for eccentricity due to wear, is based on the maximum available amplitudes given by *peak hold* process for each spectral line and for each calculated spectrum referred to specific DSP parameters set. Among the mean processes is considered for example the RMS overall (described on page 71) calculated on each overlapped time section. The simulation time history is partitioned, but this approach considers in the calculation, all the signal harmonics contributions available within the bandwidth, not opportunely filtered on prognostic precursors. Therefore the RMS overall approach and other mean processes on time or spectral signals could be not effective respects to proposed FDI approach especially if it is considered that the post-processing methodology must be applied on real-time monitoring during a ground test on aircraft where unexpected interference harmonics could appear on calculated spectra.

Table 4.2: Harmonics mapping table for Frequency track approach, after critical event at 33% RSE, $f_{H_{max}^{new}}$ take place on $f_{H_{max}}$ in all main maximum amplitude harmonics

RSE [%] Interval	I_{f_a} [Hz]	I_{f_b} [Hz]	I_{f_c} [Hz]
0÷2	$5f_{H_{max}} + \Delta f_f$	$5f_{H_{max}} + \Delta f_f$	$5f_{H_{max}} + \Delta f_f$
3	Only $f_{H_{max}}$	$5f_{H_{max}} + \Delta f_f$	$5f_{H_{max}} + \Delta f_f$
4÷6	$5f_{H_{max}} + \Delta f_f$	$5f_{H_{max}} + \Delta f_f$	$5f_{H_{max}} + \Delta f_f$
7 ÷10	$5f_{H_{max}}$	$5f_{H_{max}}$	$5f_{H_{max}}$
11	$5f_{H_{max}}$ & $7f_{H_{max}}$	$5f_{H_{max}}$	$5f_{H_{max}}$
12÷18	$5f_{H_{max}}$	$5f_{H_{max}}$	$5f_{H_{max}}$
19	$5f_{H_{max}} - \Delta f_f$ & $-4\Delta f_f$	$5f_{H_{max}} - \Delta f_f$	$5f_{H_{max}} - \Delta f_f$
20	$5f_{H_{max}} - \Delta f_f$ $7f_{H_{max}} - \Delta f_f$	$5f_{H_{max}} - \Delta f_f$	$5f_{H_{max}} - \Delta f_f$
21	$5f_{H_{max}} - 2\Delta f_f$ $7f_{H_{max}} - 2\Delta f_f$	$5f_{H_{max}} - 2\Delta f_f$	$5f_{H_{max}} - 2\Delta f_f$
22	$5f_{H_{max}} - \Delta f_f$ $7f_{H_{max}} - 2\Delta f_f$	$5f_{H_{max}} - \Delta f_f$	$5f_{H_{max}} - \Delta f_f$
23÷25	$f_{H_{sb}}$& $5f_{H_{max}} - \Delta f_f$	$5f_{H_{max}} - \Delta f_f$	$5f_{H_{max}} - \Delta f_f$
26÷30	$f_{H_{sb}}$& $5f_{H_{max}} - 2\Delta f_f$	$5f_{H_{max}} - 2\Delta f_f$	$5f_{H_{max}} - 2\Delta f_f$
31	$5f_{H_{max}} - 2\Delta f_f$ & $-5\Delta f_f$	$5f_{H_{max}} - 2\Delta f_f$;&	$5f_{H_{max}} - 2\Delta f_f$
32÷33	$f_{H_{sb}}$& $5f_{H_{max}} - 2\Delta f_f$	$5f_{H_{max}} - 2\Delta f_f$	$5f_{H_{max}} - 2\Delta f_f$
34	$f_{H_{sb}}$& $5f_{H_{max}} - 2\Delta f_f$	$5f_{H_{max}} - 2\Delta f_f$	$5f_{H_{max}^{new}} + 2\Delta f_f$
35	$f_{H_{sb}}$& $5f_{H_{max}^{new}} + 2\Delta f_f$	$5f_{H_{max}^{new}} + 2\Delta f_f$	$5f_{H_{max}^{new}} + 2\Delta f_f$
36	$f_{H_{sb}}$& $5f_{H_{max}^{new}} + 2\Delta f_f$	$5f_{H_{max}} - 2\Delta f_f$	$5f_{H_{max}^{new}} + 2\Delta f_f$
37	$f_{H_{sb}}$& $5f_{H_{max}} - 2\Delta f_f$	$5f_{H_{max}} - 2\Delta f_f$	$5f_{H_{max}} - 2\Delta f_f$
38÷45	$f_{H_{sb}}$& $5f_{H_{max}^{new}} + 2\Delta f_f$	$5f_{H_{max}^{new}} + 2\Delta f_f$	$5f_{H_{max}^{new}} + 2\Delta f_f$
46÷48	$f_{H_{sb}^{new}}$& $5f_{H_{max}^{new}} + \Delta f_f$	$5f_{H_{max}^{new}} + \Delta f_f$	$5f_{H_{max}^{new}} + \Delta f_f$
49÷50	$5f_{H_{max}^{new}} + \Delta f_f$	$5f_{H_{max}^{new}} + \Delta f_f$	$5f_{H_{max}^{new}} + \Delta f_f$

Table 4.3: Harmonics mapping table for Frequency track approach, after critical event at 33% RSE, $f_{H_{max}^{new}}$ take place on $f_{H_{max}}$ in all main maximum amplitude harmonics

RSE [%] Interval	I_{f_a} [Hz]	I_{f_b} [Hz]	I_{f_c} [Hz]
0÷5	$5f_{H_{max}} + \Delta f_f$	$5f_{H_{max}} + \Delta f_f$	$5f_{H_{max}} + \Delta f_f$
6	Only $f_{H_{max}}$	$5f_{H_{max}} + \Delta f_f$	$5f_{H_{max}} + \Delta f_f$
7÷9	$5f_{H_{max}} + \Delta f_f$	$5f_{H_{max}} + \Delta f_f$	$5f_{H_{max}} + \Delta f_f$
10	$5f_{H_{max}}$	$5f_{H_{max}}$	$5f_{H_{max}}$
11	Only $f_{H_{max}}$	Only $f_{H_{max}}$	$5f_{H_{max}} + \Delta f_f$
12	Only $f_{H_{max}}$	Only $f_{H_{max}}$	$5f_{H_{max}}$
13	Only $f_{H_{max}}$	Only $f_{H_{max}}$	$5f_{H_{max}} + \Delta f_f$
14÷19	Only $f_{H_{max}}$	Only $f_{H_{max}}$	$5f_{H_{max}}$
20	Only $f_{H_{max}}$	Only $f_{H_{max}}$	Only $f_{H_{max}}$
21÷22	Only $f_{H_{max}}$	Only $f_{H_{max}}$	$5f_{H_{max}}$
23÷50	Only $f_{H_{max}}$	Only $f_{H_{max}}$	Only $f_{H_{max}}$

Chapter 5

FDI Methodology Engine Order Track

5.1 The Main Engine Order Track Process

Rotating machinery analysis, is primarily concerned with time signals relating to the rotational speed and its harmonics, used as a reference to better understand physic phenomena analysing how their frequency responses change with RPM rotor speed velocity. In the previous section, many contributions, due to mechanical wear, like RSE rotor static eccentricity and RDE rotor dynamic eccentricity are analysed influencing Unbalance Magnetic Pull (UMP) and prognostic precursors harmonic firm under increasing failure evolution. The proposed harmonic analysis methodologies are performed by amplitude and frequency tracking approaches allowing to adapt STFT on non-stationary data, such as the boundary condition about run-up actuator run, giving two integrated approaches able to evaluate simulated system health state. On the other hand, for misalignment values sets are still present some ambiguity evaluation zones both for dynamic and static eccentricity, therefore a different harmonic approach called *"Engine Order Track"* could be used to improve presented FDI methodology. Basic order analysis analyses the relationship between frequency responses, and a reference rotation frequencies in rotating machinery, then Engine Orders (EOs) are essentially defined as the number of events evaluated in the frequency domain per revolution shaft. Engine order track is a suitable solution and approach it is able to follow the physical event amplitude evolution in rotational angle dominion θ avoiding calculating the shifting frequency due to run up or coast down of one reference rotating shaft. Considering EOs as harmonics of the rotational speed, they could be not integer harmonics of the rotating reference shaft, depending on vibration physical causes or in this study case on oscillation referred to prognostic precursors time signal. Indeed, Order Track processing is based on accurate velocity measurement at high sampling definition in the real case by phonic wheel or encoder, because it is very important to estimate with the minimum uncertainty the instantaneous speed and angular reference shaft position. In bibliography are present main three classes to approach order track techniques in post-processing applied both on the acquisition or simulated raw time signals:

1. Computed order tracking: based on synchronous sampling, where the time signal is subdivided in constant sampling $\Delta\theta$ as a function of rotational speed therefore, the signal sampling rate is proportional to reference shaft speed. The synchronous sampling extracts from time history, several samples at a fixed sample rate (i.e. uniform time spacing Δt) then in post-processing the data are re-sampled at constant angular increments, up to all time section contains the same samples calculated at the maximum shaft speed. This approach is extremely sensitive to the timing accuracy of the acquisition of key phasor pulses and using high order interpolation function [39].

2. Vold Kalmann filter: the Vold Kalman filters have been employed in commercial software since the early 90's very successfully, it can track accurately signals, knowing time structure among the noise and other signal components by extracting the time history of an order estimating amplitude phase. Based on Kalman filter was adapted on order track by [82] and [52]. These methods have some disadvantage, as the computational complexity and the experience to choose the weighting factor and correlation matrix to extract order with a minimal bandwidth while amplitude tracking in time as in [47].

3. Order tracking transforms: the raw input time signal is transformed by time frequency mathematical transforms which perform in a single step both the order tracking and the Fourier transform. This approach allows to directly assess the amplitude of one synchronous, sub-synchronous or super-synchronous shaft-locked harmonic, without an additional resampling step as in [45].

Among techniques adapted to proposed order tracking, in non-stationary operating conditions, the proposed method relies on FFT putting in evidence repetitive events on shaft revolutions, tied to the presence of a UMP unbalance magnetic field due to bearings wear and improving Coulombian friction coefficients indirectly related to cinematic transmission line wear and loss of lubrication efficiency. In previous proposed harmonic analysis, based on STFT in chapter 4, the simulated time history for prognostic precursors (the filtered supply phase currents) is partitioned in to slices called *time section* or Δs, but during order tracking the signal needs to be expressed as a function of the rotation angle $\Delta\theta$ referred to a reference rotating shaft, that in this case is represented by EMA rotor shaft. There are two most used techniques, in industrial sound and vibration order track evaluation, referring time section to transient rotating speed, transforming time signal into order spectrum (an FFT spectrum expressed as a function of engine order rather than frequency). The first technique consists to refer a single time section to a reference shaft speed supposed constant over the slice duration, the second technique provides to synchronous resampling of time sections by interpolating sampled values with polynomial function with high grade, imposing $\Delta\theta$ constant angle revolutions steps. The synchronous sampling generates time slices with different elapsed times as rotor shaft speed function, more speed is higher, shorter is the time section extracted on one single shaft revolution. After sectioning time slices at a fixed sample rate, each slice is resampled with $\Delta\theta$ constant increments, therefore each time slice has the same synchronous sampling taking as reference the number of samplings extracted at maximum shaft speed. Each above-mentioned technique presents drawbacks the first has a worsened frequency resolution, especially at low rpm, the second during resonance phenomena introducing response alteration.

Evaluating drawbacks and the simulation framework on which order tracking is performed, the choice on proposed order track method is focused on the first most used in industrial application referring each extracted time section to a reference rotational speed for the conversion from frequency dominion to orders dominion. In this methodology, each extracted time section from the time history at a fixed sample rate by defining constant *block size*, is transformed in the frequency spectrum by FFT after applying windowing function and time section overlap. The main transformation from frequency dominion to rotational angle dominion or orders dominion, is based on the local rotor mean speed ω_m evaluating instantaneous rotational speed at beginning ω_0 and ending ω_1 of each time section. In other words, considering the local mean rotational shaft speed, this reference *"mean speed"* ω_m is imposed constant over the time slice to perform dominion conversion. Since order track analysis transforms several events per time units (frequency dominion) in several events per revolutions, the same phenomena can be expressed as either a frequency or an EO as expressed in (5.1) representing the axis transformation from spectrum in Hz to order spectrum used in the proposed methodology.

$$f_{event}\,[Hz] = \frac{EO_x \cdot \omega\,[RPM]}{60} \tag{5.1}$$

The (5.1) represents the main relationship between EO and frequency known the rotor shaft speed in correspondence of spectrum calculation. Is evident that order track analysis is based to speed time function on which each spectrum is calculated and transformed in magnitude order spectrum. The EMA actuator is a simple rotating machine and to better understand order analysis a simple analogy could be introduced with a rotating fan with six blades. For example, a fan shaft rotates at fixed speed ω equal to 6000 RPM therefore the shaft frequency is 100Hz the blade pass frequency is 600Hz (six blades for each shaft revolution so 6*100Hz) the engine order for Blade Pass Frequency (BPF) is the 6th engine order. Therefore, if the shaft speed increased during run up the BPF growth based on linear relation (5.1) where the time signal could be acquired in a real case study by an accelerometer placed on the shaft bearing in the radial direction.

To overcome issues of massive calculation about all features related to Engine Order Track in all simulation operating conditions, we relied on a certified tool called *"NVT-Rotating Machinery"* form *Wintek s.r.l.*, based on National Instrument libraries to provide all engine order tracking calculations described in 5.2. The integration between Simulink high fidelity model, to approximate the EMA system behaviour in different progressive multi mode failures, and *NVT-Rotating Machinery*, provides to collect engine order tracking results aggregating by Matlab in 5.2 as prognostics method.

5.1.1 Digital Signal Processing parameters

Several FFT Fourier Transforms are performed at multiple time slices or instances in time, during transient rotating speed, generating Order Spectrum based on another DSP set of parameters reported in table 5.2 on which FFT intermediate calculations, for frequency spectrum, are performed. The table 5.2 shows different DSP parameters

Table 5.1: DSP digital signal parameters used to perform Engine Order Tracking

DSP Parameters	Value	Engineering units	Description
f_s	10^{-6}	[Hz]	Sample Rate
Δs	0.125	[s]	Time Section
Δf	8.00	[Hz]	Frequency Resolution
N	1250	[Sa]	Block Size
Sl	625	[bins]	Spectral Lines or Bins
bdw	4800	[Hz]	BandWidth
Windowing	Hanning	Na	Type Windows Function
Interpolation Bins	3	[#]	Spectral Bins for Peaks Interpolation
Overlap	90%	[#]	Overlap superposed Time sections

than the set used in 4.1 on page 82 referred to a harmonic analysis performed for static and dynamic eccentricity, because it is needed to improve spectral density, an increasing number of calculated spectra from time history, during a very high-slope speed imposed by reference simulation boundary conditions, therefore compromise arise with a worsened frequency resolution. Indeed, the frequency resolution used for harmonic analysis is changed from $\Delta f = 4\,[Hz]$ to $\Delta f = 8\,[Hz]$, by the (3.17) this change affects the time section with a smaller time interval $\Delta s = 0.125\,[s]$ extracted from the time history to perform windowing and FFT. A smaller time section implies with the same simulated time history and correspondent transient speed evolution in time, to calculate several spectra in frequency dominion to transform in engine order spectra. A major number of engine order spectra allows defining with improved accuracy the engine order tracking as a function of transient speed, as a compromise with a coarse frequency resolution. A coarse frequency resolution could be partially compensated by reducing the number of spectral bins on which calculate the engine order as quadratic interpolation based on 3 spectral bins from 5 bins previously used as indicated in figure 5.1.

Parseval theorem affirms that signal time energy distributed around a local reference bin should be the same considering the leakage due to time windowing. On equal terms, the same time signal an FFT distributes quite the same energy if we consider the

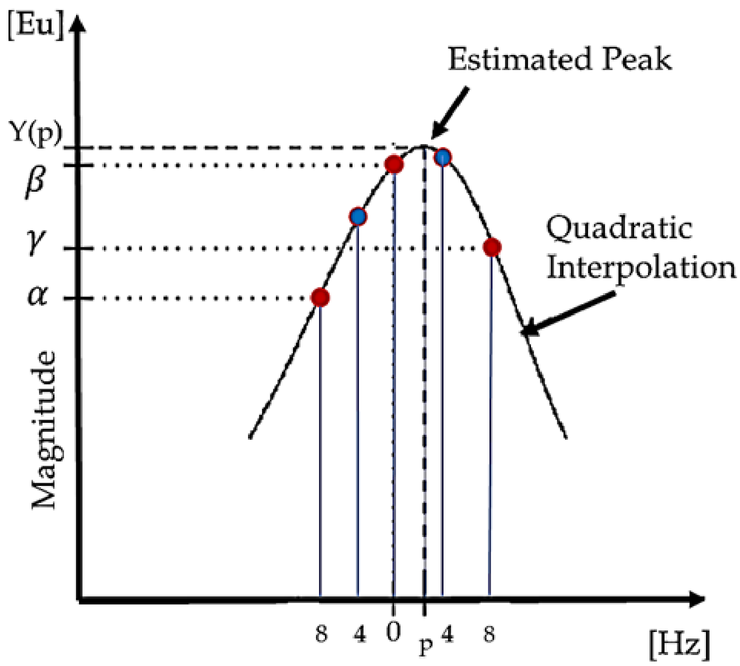

Figure 5.1: Qualitative quadratic interpolation to calculate frequency and magnitude for estimated peak based on 5 bins with $\Delta f = 8\,Hz$ red p.ts and $\Delta f = 4\,Hz$ in blue p.ts

interpolation based on 5 bins equally spaced of 4 Hz or based on 3 bins equally spaces of 8 Hz. This assumption is in first approximation valid with acceptable deviations, if the same windowing type is used to windowing the time sectioned signals. Order tracking is performed applying the above-mentioned process to time-dependent prognostic precursors simulated varying both RDE and RSE misalignment percentages, generating for each simulation one *engine order colourmap* represented as an example in fig.5.2. During the presented order track process another incipient failure is considered, by improving Coulombian static friction coefficient F_S from 0.2 in normal condition to 0.8 relating to the indirect evaluation of wear for the surfaces contact on transmission line from EMA to aerodynamic surfaces with reduction gearbox. An extended order track database is collected simulating EMA behaviour on improving unbalanced magnetic pull referred to static and dynamic condition with three different Coulombian friction health state referred to 0.2 (normal condition), 0.4 (warning condition) and 0.8 (critical condition) F_s static friction coefficients. The static friction coefficient is used as a reference parameter to estimate operating system friction because in first approximation EMA simulation numerical model approximate the dynamic friction constant F_d as the half value of F_s.

5.2 Engine Order Results

Engine order track results are calculated following a calculation matrix, fixing the same physical boundary conditions but varying UMP percentage with the increasing step of 1%, due to progressive misalignment both static and dynamic, integrating two different coulombian friction conditions: the normal condition with static friction coefficient F_s equal to 0.2 and the critical condition with F_s equal to 0.8 dimensionless constant. The warning condition referred to F_s equal to 0.4, is neglected in this results presentation, although calculated, to describe the entire friction coefficients range by extremes, with the related effects on prognostic precursors, improving evidence exposition. Results are calculated and organized in *"EO Database"*, and for each eccentricity percentage types in three different friction conditions under which mechanical transmission operates, the following engine order tracking results are calculated:

- *Engine Order colourmap*: autopower spectrum 3.4.6 collection in RMS amplitude format expressed in time [s], engine order [#], magnitude [A];
- *Peak Hold Order Diagrams*: diagrams collecting maximum magnitudes [A] for each order bin coming from engine order colourmaps, expressed in orders [#];
- *Slice Order identification*: form each peak hold diagram the five first 5 peaks with the best magnitudes are identified, to perform a slices order extraction;
- *Slices Order extraction*: from each calculated engine order colourmap the engine order identified by peak hold order best 5 peaks are extracted considering 3 order bins for calculating RMS value;
- *Slices Order Maximum extraction*: form each extracted slice order the maximum value is detected to correlate this maximum engine order value to the considered progressive failures grade;

Coming from *"EO Database"*, in figure 5.2 are illustrated engine order colormasp calculated for 0% and 50% RSE percentages, and in 5.3 for 0% and 50% RDE percentages both under normal friction condition, where is evident by comparison the progressive arise of some engine orders magnitudes with increasing UMP. Order colourmaps represents a collection of spectrum orders instead of frequency, to perform orders tracking approach, being more effective correlating some specific orders trends, related to concurrent failures types rather than evaluating only 3D order colourmaps that could give only qualitative high-level evaluations. What engine orders should be selected to perform a robust FDI fault quantitative failures detections and evaluations, are defined by *peak hold order* diagrams coming from order colourmaps calculated in different EMA simulated conditions. Reference engine order tracking results, in the proposed FDI methodology, are focused on the filtered phase current I_{fa} interested by minimum reluctance for static eccentricity and beginning with a minimum air gap from this phase for the rotor

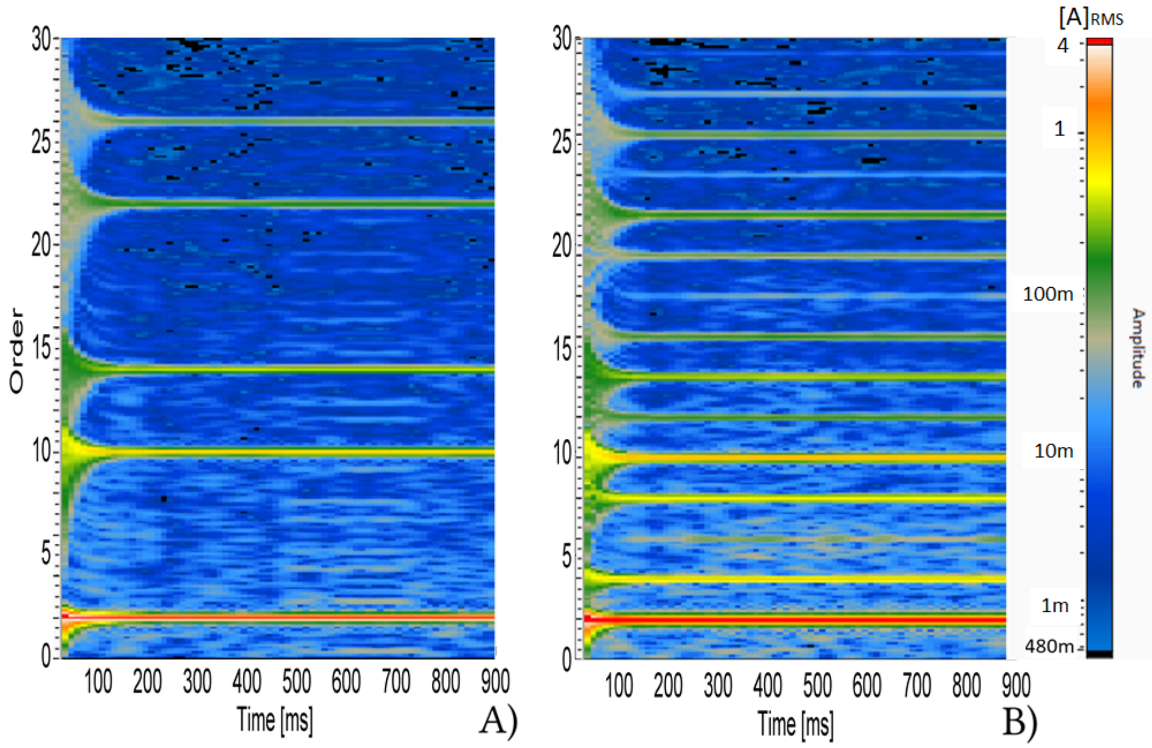

Figure 5.2: A) Engine Order colourmap 0% RSE ; B) Engine Order colourmap 50% RSE; both colourmap are calculated for I_{fa} at $F_s = 0.2$ under normal friction condition.

dynamic eccentricity. This choice is based on filtering the most significant order tracking results getting targets to define the EMA health state within the *EO database*, identifying with an acceptable accuracy rotor static and dynamic eccentricity integrated with the operating friction conditions. In 5.4, are compared as an example coming from *EO database*, two *peak hold order* diagrams calculated on engine order colourmap showed in 5.2, highlighting the five maximum first 5 engine order peaks.

During the evolution of air gap reduction both for RDE and RSE, the first 5 maximum amplitude peaks are calculated, related to peak hold order diagrams, they may present little changes form the lowest eccentricity value, especially up to the end of eccentricity range.

Despite this, it is possible to easily identify a set of four **main engine orders**, directly correlated with physical excitation events, during a single EMA revolution rotor shaft. After orders identification for FDI methodology, the correspondent orders slices are extracted from associated engine order colourmaps as quadratic interpolation. The number of spectral bins on which is based the extraction, is 3 spectral bins and for each slice, the maximum order slice value is calculated so it is possible in a reference simulation time to associate maximum order slice value to different failures path acting

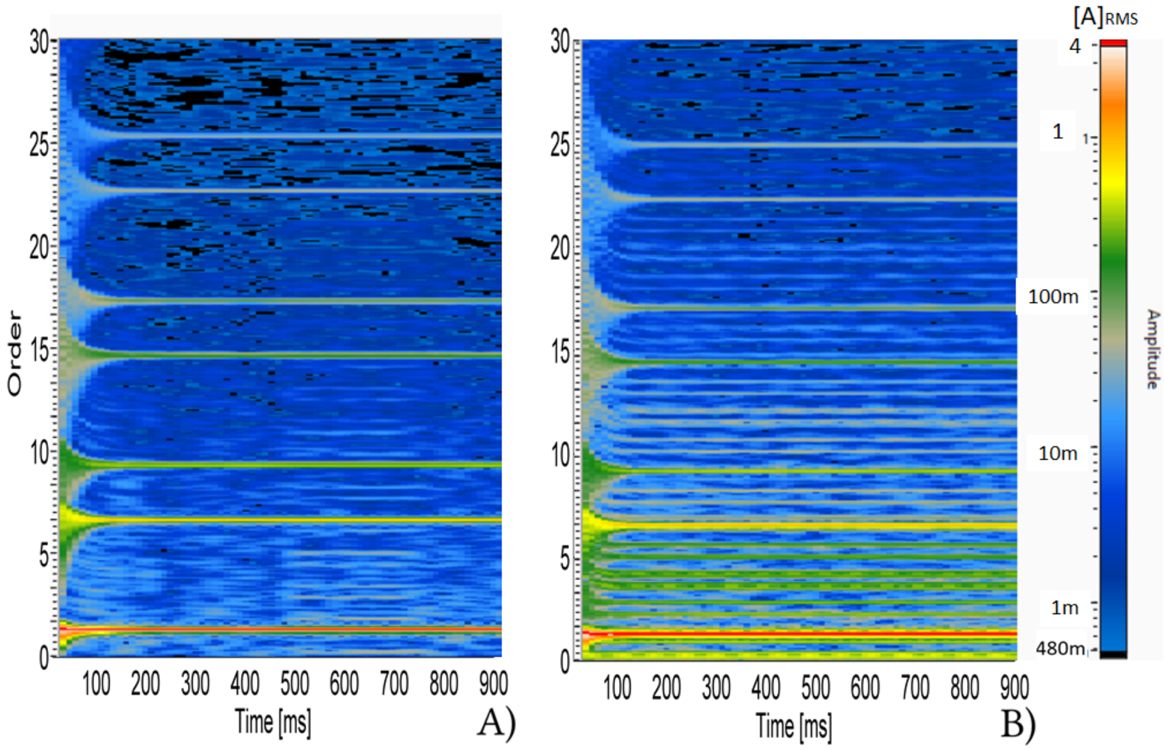

Figure 5.3: A) Engine Order colourmap 0% RDE ; B) Engine Order colourmap 50% RDE; both colourmap are calculated for I_{fa} at $F_s = 0.2$ under normal friction condition.

in concurrent mode to the same prognostic precursors. The *main engine orders* identified by *peak hold order*, are following described in correlation with the physical events taking place during EMA rotating shaft:

- **[EO 0.44X]**: this not integer engine order describes the excitation event due to the minimum air gap direction rotation speed detected by each prognostic precursor stator supply phase. Indeed, in the numerical model the precession speed during RDE rotor dynamic eccentricity is fixed to 44% of the rotor component speed around its mass centre, as first approximation correlated to the cage rotational speed of bearing gages. This approximation proceeded from cinematic evaluation on bearing geometry configuration as a function of the radial load as reported in [43] where this condition is verified as the mean between the proposed model and experimental validation. In figure 5.5, peak hold order reveals that this particular engine order appears only after a threshold air gap reduction limit. The peak hold order diagrams of *EO database* identify the 28% RDE the air gap reduction percentage from which EO 0.44X is selected by the first 5 magnitude peaks but since this engine order is related exclusively to rotor dynamic eccentricity it is a compendium for the main FDI methodology applied by comparison with RSE

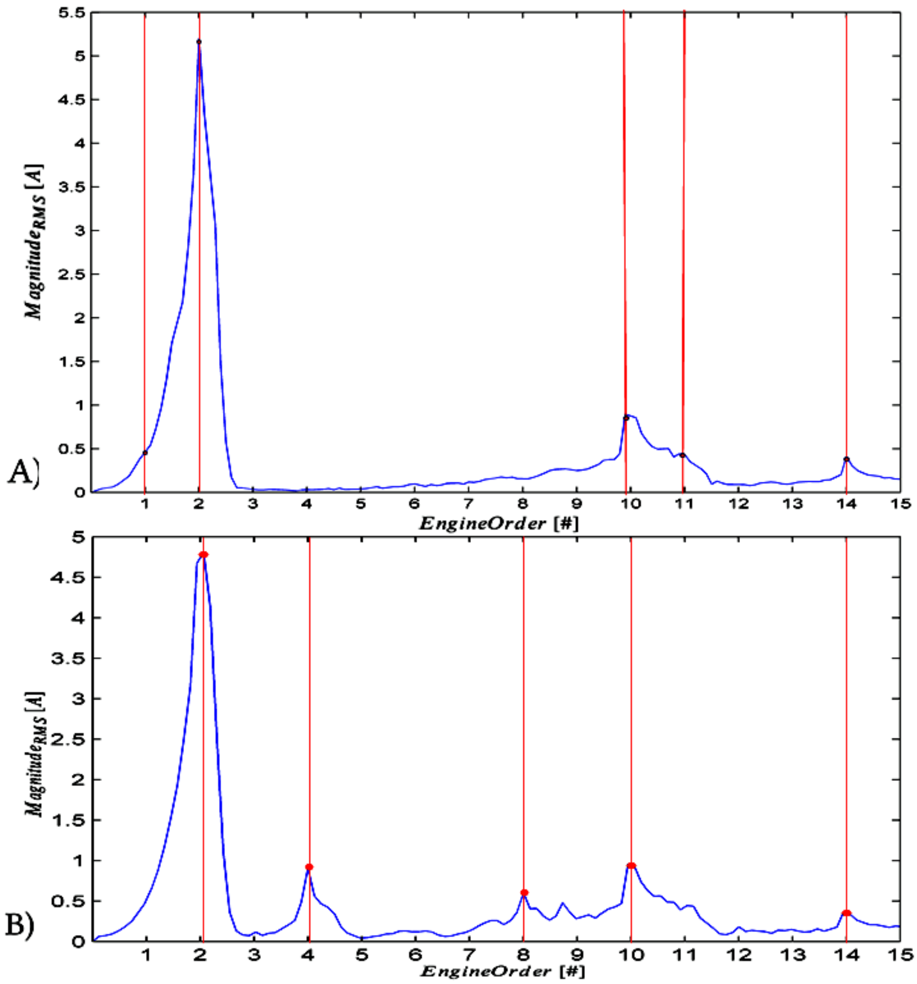

Figure 5.4: A) I_{fa} peak hold order 0% RSE; B) I_{fa} peak hold Order 50% RSE; both colourmaps are calculated under normal friction condition at $F_s = 0.2$, highlighting the first 5 peaks magnitudes by red vertical lines.

engine orders values under different friction condition. However, since the EO 0.44X appears as results of algorithm selecting from peak hold order diagrams at specific rotor dynamic eccentricity the 28% is chosen by the proposed order track approach as warning event integrating information coming from the magnitude and frequency tracking.

- **[EO 1X]**: the first engine order in rotor-dynamic vibrations is associated with unbalancing condition referred to the rotating shaft. In this case, the unbalance is a magnetic unbalance pull derived by magnetic flux space distribution that generates a radial force as the vectorial composition of F_x and F_y indicated in 4.2 from the simplified Maxwell radial stress tensor integration. The magnetic

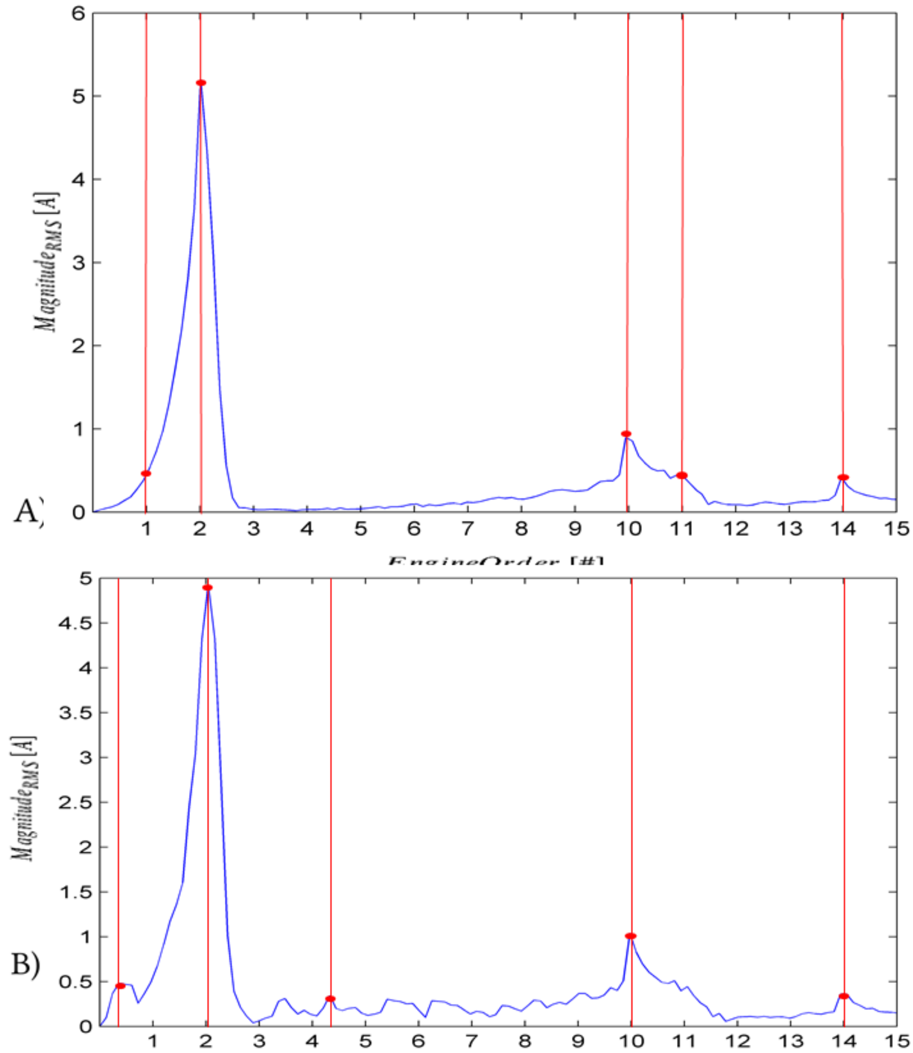

Figure 5.5: A) I_{fa} peak hold order 0% RDE; B) I_{fa} peak hold Order 50% RDE; both colourmap are calculated under normal friction condition at $F_s = 0.2$, highlighting the first 5 peaks magnitudes by red vertical lines.

unbalance must be added to structural unbalance that could affect a rotational shaft, in this work the reference EMA shaft is considered perfectly balanced so that only magnetic unbalanced pull is effective on EMA rotor shaft. In figure 5.6 the maximum EO 1X is plotted versus both rotor dynamic and static eccentricity per percentages considering the extremes friction static coefficient range. The EO 1X tracking can detect the eccentricity air gap percentages quite linear, and the EMA friction static coefficient condition. But is not the right engine order to consider to distinguishing the correct rotor eccentricity type due to RDE and RSE superposition.

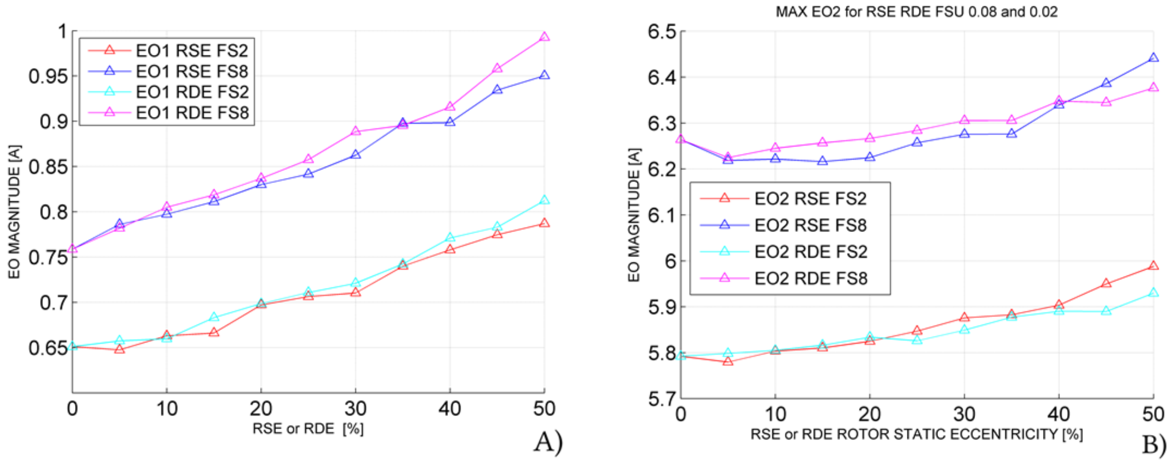

Figure 5.6: A) Engine Order 1X tracking; B) Engine Order 2X tracking; Both the Engine Order tracking are performed as a function of RSE and RDE percentages and two extremes static friction coefficients range, where $FS2 = 0.02$ and $FS8 = 0.08$.

- **[EO 2X]**: the second Engine Order is associated in rotor dynamic to *rotor misalignment*, defined as the displacement of the moving shaft position respect to the static rotation centre, with the equipment operating under normal operating conditions. In a rotating machine the *rotor misalignment* is a progressive fault, it could be eval-

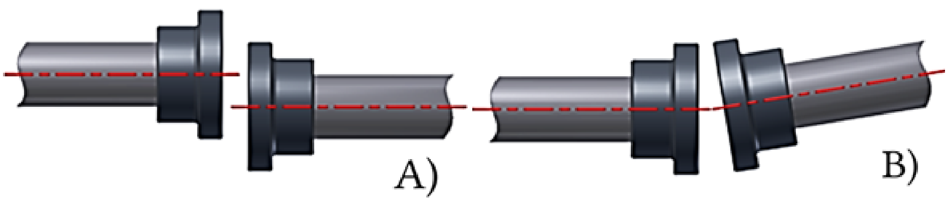

Figure 5.7: A) Rotor Misalignment in parallel axis gap ; B) Rotor Misalignment in angular incident axis gap;

uated by different mechanic symptoms since minimum parallel or angular gap as reported in 5.7, moreover it could cause radial vibrations, premature seals and bearing failure with excessive oil leaks and increasing bearing temperature. Therefore, it's important to correlate the EO 2x behaviour, associated with changing static friction coefficients, since they are integrated aspects for different failure types in concurrent mode on the same prognostic precursor. Coming from peak hold order diagrams, the EO 2X is the higher order slice magnitude than all the other engine orders, and similarly with the information taken from maximum slice EO 1X reported in 5.6, it is possible to evaluate by EO 2X with accuracy the eccentricity percentages and the static friction operating conditions. The limitation to consider for FDI algorithms only this engine order is represented by trends superpositions with some ambiguity points making hard to distinguish RDE from RSE.

- **[EO 4X]**: the fourth Engine Order is very important because it describes in one rotor shaft revolution 4 excitation events related to physical EMA configuration. Since each supply stator phase is composed of 4 poles and the rotor permanent magnets by 1 pair pole, for each revolution each stator pole is excited by 1 rotor pair pole from peak to peak of the magnetic excitation by opposite sign, generating the fourth Engine Order following the related shifting frequency as a function of rotor speed transient. The maximum EO 4X slice magnitudes allow tracking and distinguish very clearly the rotor eccentricity type and air gap reduction percentage development (static or dynamic) as reported in figure 5.8, on the other hand some superposition points make difficult to evaluate static friction operating condition.

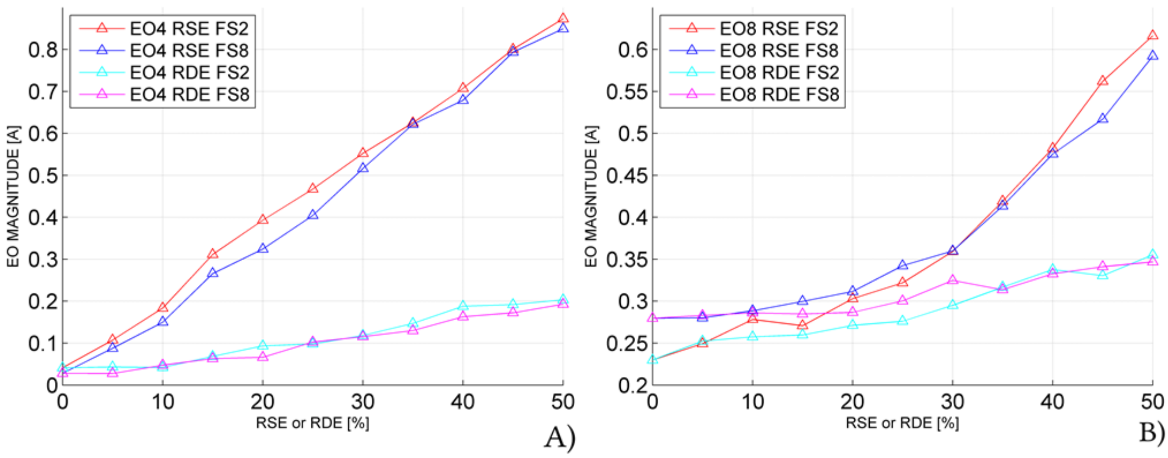

Figure 5.8: A) Engine Order 4X tracking; B) Engine Order 8X tracking; Both the Engine Order tracking are performed for I_{fa} as a function of RSE and RDE percentages and two extremes static friction coefficients range, where $FS2 = 0.02$ and $FS8 = 0.08$.

- **[EO 8X]**: the eighth Engine Order is closely related to the fourth, because representing the 8 excitation events during one rotor shaft revolution related to physical EMA configuration. Since each supply stator phase is composed of 4 poles that are excited by 2 rotating permanent magnetic poles, with opposite magnetic orientation, from 0 to peak. The maximum EO 8X slice magnitudes allow tracking and distinguish very clearly the rotor eccentricity type and air gap reduction percentage development (static or dynamic) as reported in figure 5.8. On the other hand some superposition points make difficult to evaluate static friction operating condition. Indeed, the RDE trend is quite linear due to the rotting air gap that smoothing the trend on improving eccentricity, if compared with divergent RSE trend at up to eccentricity end range related to a strongly nonlinear relationship between filtered supply currents and magnetic flux density as reducing air gap.

The peak hold diagrams identify further engine orders than the main orders above described in detail, as a linear combination based on the main ones. These orders linear combination present slices maximum magnitudes, as shown in 5.9 and 5.10, with less information useful to define eccentricity percentages, type of rotor eccentricity, and for static friction operating condition there are some ambiguity points by superpositions.

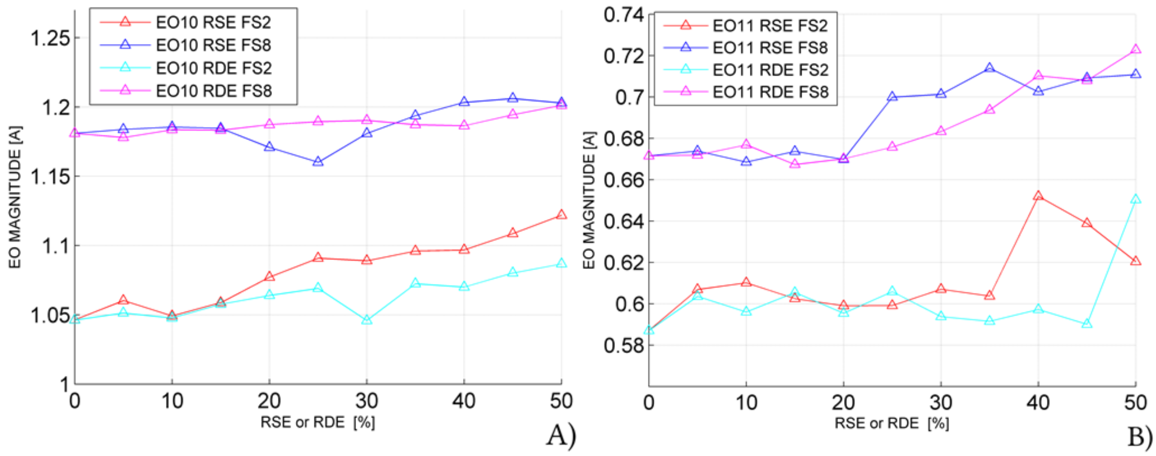

Figure 5.9: A) Engine Order 10X tracking; B) Engine Order 11X tracking; Both the Engine Order tracking is performed for I_{fa} as a function of RSE and RDE percentages and two extremes static friction coefficients range, where $FS2 = 0.02$ and $FS8 = 0.08$.

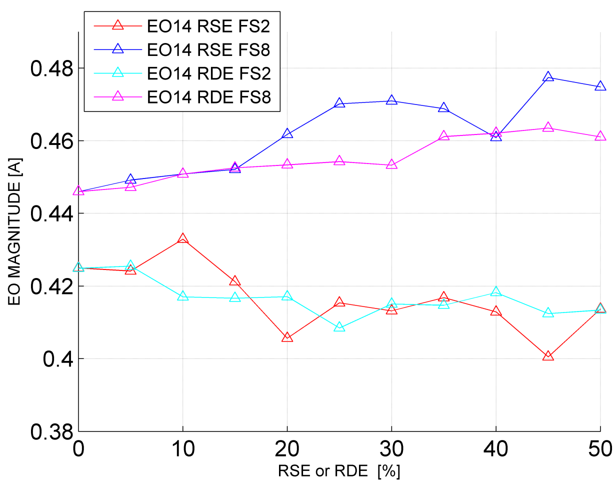

Figure 5.10: Engine Order 14X tracking; the Engine Order track are performed for I_{fa} as a function of RSE and RDE percentages and two extremes static friction coefficients range, where $FS2 = 0.02$ and $FS8 = 0.08$.

However, the linear combination engine orders track, improves the robustness FDI proposed methodology, based on order track processing, completing a more complex framework generating failure maps described above. This further information is to be integrated with more effective information from main engine orders, they could be used as a safety redundancy when comparing real-time acquisition on operating EMA and simulated failure maps database. In conclusion, there is evident that integrating magnitude, frequency, and engine order track approaches developed in chapter 5 and chapter 4, applied on prognostic precursors namely filtered supply phase currents, it is possible to achieve the following FDI goals evaluating with acceptable accuracy the EMA health state under different failure types:

1. Estimate UMP by estimating air gap reduction between rotor and stator starting from perfect alignment up to 50% eccentricity
2. Evaluation of the eccentricity type as static eccentricity, where the minimum air gap direction is fixed on a stator reference system, or dynamic eccentricity where minimum air gap direction rotates around stator geometry centre with precession speed constant in a perfectly circular orbit.
3. Evaluation of static friction coefficient as indirect precursors for mechanical power transmission affected by mechanical wear. The considered mechanical transmission starts from EMA rotor shaft up to ball screw jack connected to the aerodynamic surface of the aircraft primary control system through gearbox reducer.

5.3 Influence of Static Friction Coefficients on Harmonic Analysis Results

In section 5.2, another failure type is integrated with the UMP both static and dynamic eccentricity, the static friction coefficient variation as indirect prognostic coefficient of the wear and lubrication inefficiency referred to the transmission line, affecting the dynamic firm response of the filtered phase currents used of prognostic precursors for the proposed FDI methodology. A common factor for the above mentioned failure types is the mechanical wear of bearing and transmission elements as driven shafts, reducer gearbox, ball screw jack, hinges, and seals evolving both into air gap reduction between EMA rotor and stator and changing friction operating conditions. Therefore, the integration of these failure types, in concurrent mode on the same prognostic precursors, is high as evident from the engine order tracking process, where misalignment between driven and drive shafts could cause lubrication inefficiency. In general, the considered simulation boundary conditions, and the resulting pre-flight test requirements, provide a no-load activation of the primary flight aerodynamic surfaces. Hence the improving of friction coefficients as primary effects an increasing resistant torque applied on EMA rotor shaft starting from the static condition than during rotating one, since the dynamic friction coefficient is considered in first approximation equal to half of static one.

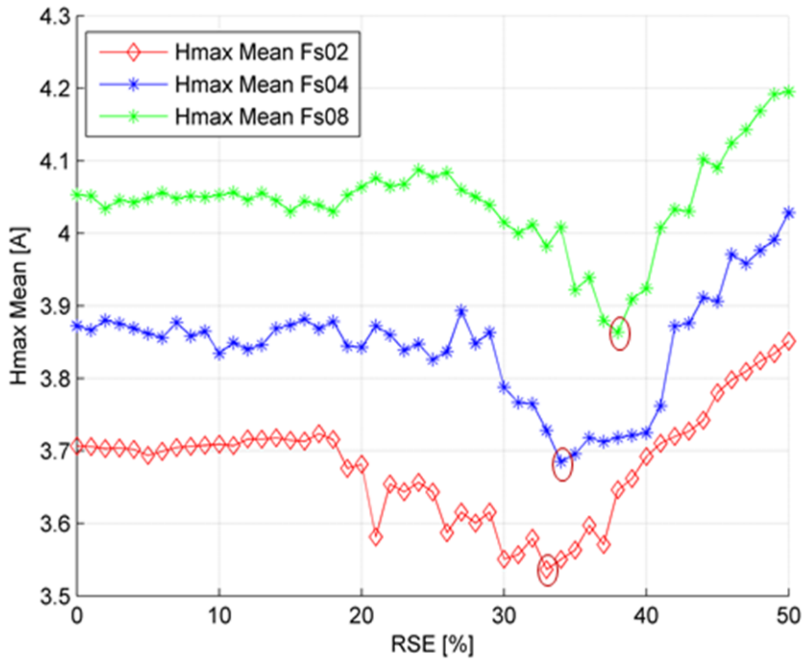

Figure 5.11: Envelope of maximum peak amplitude H_{max} for RSE failure at three different static friction operating conditions, as mean based on three filtered phase currents values. In purple circles the global minimum values representing the *critical event*.

The step command with high value forces the control system to reach the maximum rotating speed under no load condition on the aerodynamic surface to improve an indirect evaluation of the wear affecting the sliding surfaces for a multi-body transmission line. The sliding wear, acting between relative motion surfaces, is based on delamination theory as in [74] where a simplified analytical model explains the relationship between friction coefficients and wear constants on energy criterion of the delamination process. During the sliding wear, the metal surfaces in contact increase the roughness by subsurface crack nucleation and propagation as described in [75] and [7], if we consider both surfaces with different metallic material as in [32] or same borided steels surface as in [42]. The borided steels are surface treated steels by the boriding process to increase extremely hardness and wear resistant on metallic substrates with excellent mechanical operating performance in aerospace applications. Flight primary control system is a critical system to endure flight safety, therefore we could use the experimental results reported in [42] as reference work, defining a strong correlation between roughness increasing and friction coefficient increasing, even if the lubricant presence between surfaces reduce the rough improving due to sliding wear.

Summing up the sliding wear occur between relative motion surfaces in contact, by delamination theory and adhesion models, this surface sliding fatigue improve roughness and the correlated friction operating coefficients.

A first step to evaluate the improving static friction coefficient on dynamic responses in the presence of concurrent failures due to unbalance magnetic pull is evident in 5.2. If the presence of dynamic responses, affected by different friction constant grades, are evaluable in engine order track approach, this failure type affects other dynamic responses about the magnitude and frequency track previously exposed in 4. The magnitude track process to evaluate rotor static eccentricity is strongly influenced by different increasing static friction coefficients, not only with amplitude scaling but also for what concerning the global diagram minimum amplitude value, identifying the critical event eccentricity percentages. In figure 5.11, are compared three mean H_{max} maximum magnitude peaks envelope, as described in 4.2.3, strongly affected by improving static friction coefficients, not only for amplitude scaling but also for what concerning the global minimum diagram representing the eccentricity critical eccentricity. In the table 5.2, are

Table 5.2: Maximum amplitude H_{max} harmonic frequencies calculated before and after the *critical event* as a function of increasing static friction coefficients.

F_s [#]	$Freq._{H_{max}}$ Before Critical Event [Hz]	Critical Event H_{max} [Hz]	$Freq._{H_{max}}$ After Critical Event [Hz]	Δf_f [Hz]
0.02	33.568	33.00	32.805	0.763
0.04	32.805	34.00	32.402	0.763
0.08	32.042	38.00	31.279	0.763

indicated the frequency values for the maximum current peak harmonic as a function of the critical event percentages and static friction coefficients. It is evident that the frequency step, at fixed static friction coefficient, for the main magnitude harmonic calculated before and after the critical event is fixed to $\Delta f_f = 0.763\ Hz$ independent from the static friction coefficient variation. Other effects on dynamic response due by increasing static friction coefficients, is represented by the frequency step occurring as a function of friction coefficients at the same RSE operating conditions (before or after the global critical event). The increasing step from a beginning normal condition friction $F_s = 0.02$ and the following friction step are defined as $\Delta F_s = 0.02$, corresponding to $\Delta f_f = 0.763\ Hz$ referred to the difference among main harmonic frequency to the corresponding ones for each increasing friction step. Therefore, for fixed discrete variations of static friction coefficients are correlated fixed discrete steps for the main harmonic frequencies before and after the minimum global amplitude value as a function of friction operating conditions as in figure 5.11.

In equation (4.9) on page 85 is described as the quite linear trend for H_{sb} the *unbalance harmonic* equal to 2X H_{max} frequency, this significant harmonic is influenced by friction

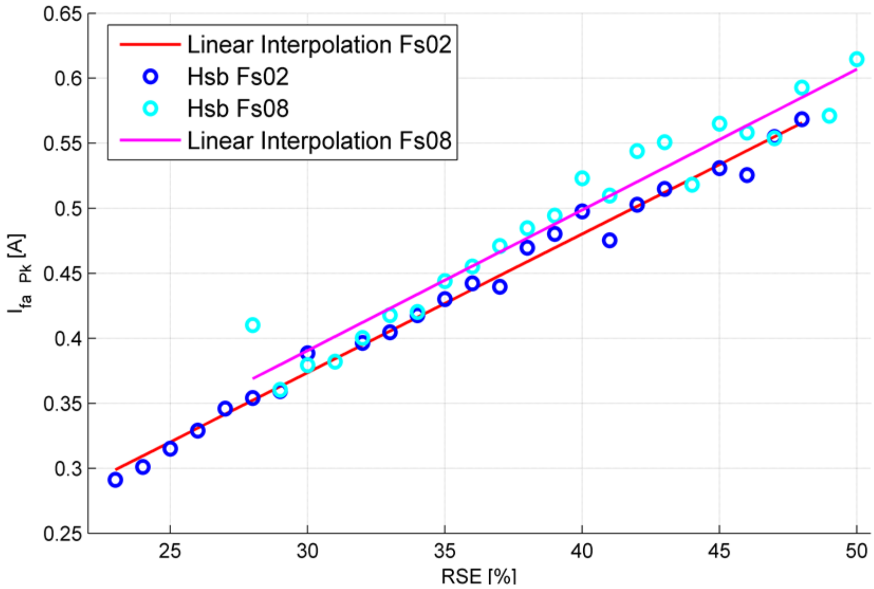

Figure 5.12: Linear interpolation for peak amplitudes H_{sb} dispersion for different static friction operating conditions, $FS02 = F_s = 0.02$ and $FS08 = F_s = 0.08$

coefficient variation as in fig. 5.12, where linear interpolation at least squares is increased by static friction coefficients increasing considering extremes variation range.

All results, from harmonic analysis about magnitude and frequency track approach, are affected by magnitude increment (in some case also by main frequency steps as H_{max} harmonic), associated with improved friction torque due to wear quantified indirectly by increasing static friction coefficients. Another evidence of this global effect on filtered phase currents, used as prognostic precursors to detect the EMA health state, is represented by the diagram in fig. 5.13, where globally trends shapes are increased as a function of static friction coefficients.

In conclusion the health state for transmission line wear considered from EMA rotor shaft to aerodynamic surfaces could be evaluated indirectly by increasing of static friction coefficients although are present in bibliography several wear models and experimental approach to evaluate the friction operating condition for different metal surfaces in contact. These results are reported as most significant to give evidence of how friction conditions changes could impact on harmonic analysis results. The comparison between model-based results and real time operating conditions are the key aspects performed on prognostic precursors used to detect and evaluate different failures type acting in concurrent mode. The collection of all friction coefficients effects, on the magnitude and frequency track approach results, described in previous sections are stored in *"Fsx database"* and organized for RDE and RSE rotor eccentricity, improving failure maps framework. Investigating the harmonic results of proposed FDI methodology, for failures correlated to mechanical wear, magnetic field interactions with mechanical geometry

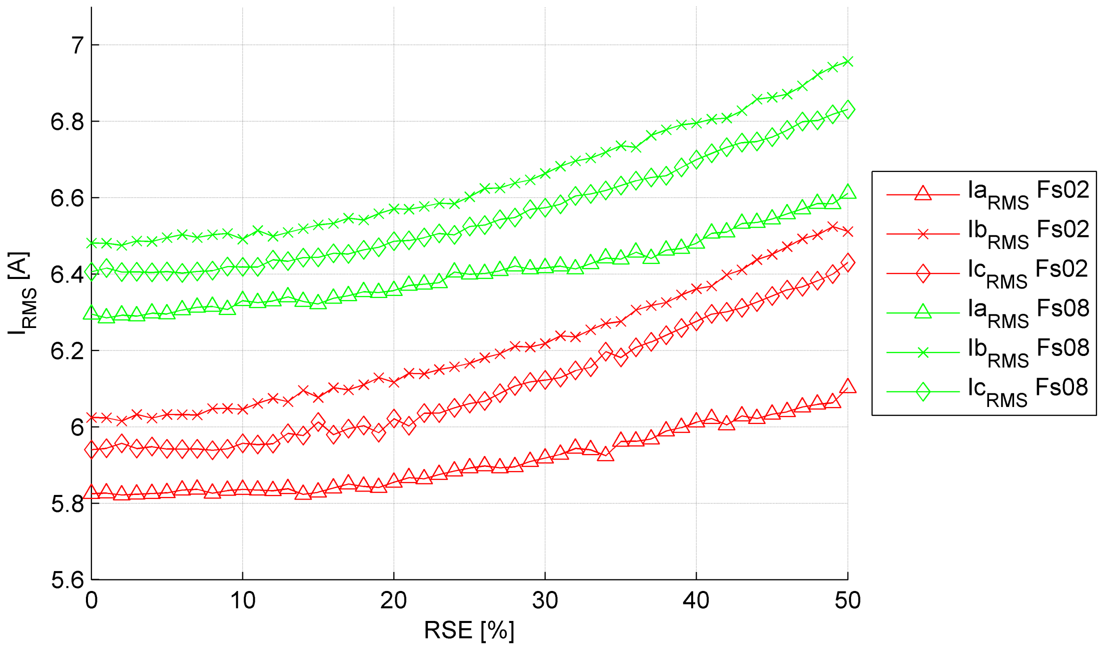

Figure 5.13: RMS evolution for three filtered phase currents as a function of eccentricity percentage and static friction coefficients.

variations highlight that different failure types on the same prognostic precursors could be analysed by model-based approach with different effects. The electromechanical actuator with evident limitations could be considered its self a sensor about primary flight system health state. ‘

Chapter 6

FDI Methodology For Short Circuits Turn To Turn

In previous sections are quickly described the short circuits faults among stator supply windings in 2.3.5 on 45, due to thermal and electrical stress on insulation coils. Although in 2.3.1 on 36, are reported the main results of the only two extensive induction motors failures investigations in [67], [68] and [79]. It is difficult an accurate evaluation of short circuits failure impacts on induction motor operations in particular for the BLDC motor class utilized for the primary flight control system. The supply coil is made by copper conductors wound through stator caves, separated by insulation material. The insulation winding design is different between windings used for low voltage and used ones in supplying above 1000V, used as a reference value to distinguish low voltage to high voltage induction motors as described by [73]. The EMA simulation model is referred to the low voltage category, with "random-wound" insulation type, and during short circuit turn to turn, the only short circuit type able to continue BLDC motor operating condition in failure presence. During the turn to turn failure, locally on the shorted turn, the current flow arises generating overheating phenomena self-generating even more thermal stress on near insulation zone. The evolution into progressive failure steps, is determined by short circuit type changes, from turn to turn in to phase to phase or phase to ground failure, up to protection electrical system turns off the power supply stopping operating induction motor. Therefore even if the statistical investigation doesn't define a quantitative impact for this failure type among the low voltage induction motor class, the EMA defines very hazardous impact for the failure of the short circuit to the flight safety. How long time is needed to develop undetected short circuit turn to turn in to phase to phase or phase to ground short with catastrophic consequences, it is a variable not to be defined. Many variables as aerodynamic load, load cycles, environmental operating conditions due to flight mission profiles, interact to define the evolution time, so the FDI target is the focused achievable target to early avoiding undetected short coil turn to turn failure. In scientific bibliography are present several papers indicating a different experimental data driven approach to identify in the frequency dominion the short circuit failure on an induction motor. Shortly it is possible classifying them into two monitoring approach the motor current signal based on current sensors acquisition as in [71] and axial stray flux leakages based on stray magnetic flux probes as in [59]. The results robustness is a function of many variables and test configuration characteristics as closed loop system i.e. DTC direct torque control system, where inherent asymmetries leading some reference frequency components growing without faults are present as in [23]. In [36]. The two integrated approaches are performed identifying reference harmonic components related to short circuit turn to turn insulation on an induction motor with a frequency input supply of 50 Hz and FFT time section of the 50s. There are several differences between the experimental and model-based approach to detect and evaluate short circuits faults, then within model-based approaches, it is possible to distinguish between within time domain simulation a finite element approach, and high-fidelity models as presented in this research to simulating EMA behaviour under specific boundary conditions. In this chapter, the short circuit fault is integrated with other failures types that could affect the EMA as previously described by analysing in the frequency domain the same prognostics precursor represented by supply filtered phase currents. The proposed harmonic analysis in the previous chapters has already produced sufficiently accurate results, for identification and quantification of the percentage of air gap reduction and of friction changes. In this section, we illustrate how the progressive short circuit turn to turn has impacts on the dynamic firm prognostic variables based on the effects of superposition philosophy. The fault variables to describe progressive short circuit on stator windings are N_a, N_b, N_c, referred respectively to the filtered phase currents I_{fa}, I_{fb}, I_{fc}, indicates the percentage of operative coils on the supply current poles. Then a N_i (where $i = a, b, c$ refers to the different stator phases of the three-phase BLDC motor) value of 1 indicates fully operative stator coils without electrical short circuits. In a first approximation, the tolerance limit about the number of shorted coils within a single phase is fixed equal to 25% equivalent to minimum allowable value equal to 75% for generic N_i, higher values are associated with very quick overheating and degeneration path for turn to turn failure evolving in to phase to phase or phase to ground short circuit failure.

6.1 Crossing Points Operating Maps

The Root Mean Square RMS of a given signal time history represents a measure of its overall energy and it is often used to extract signal features and trending data for FDI fault detection and identification processes as indicated by [14]. Operatively speaking, the results reported are calculated as a function of a progressive SC acting on the coil of the phase *”a”*, with N_a varying from 75% to 100% with a 1% increasing step. The progressive SC degradation of the single phase “a” induces an increasing of the three phases current RMS as a function of Na percentage.

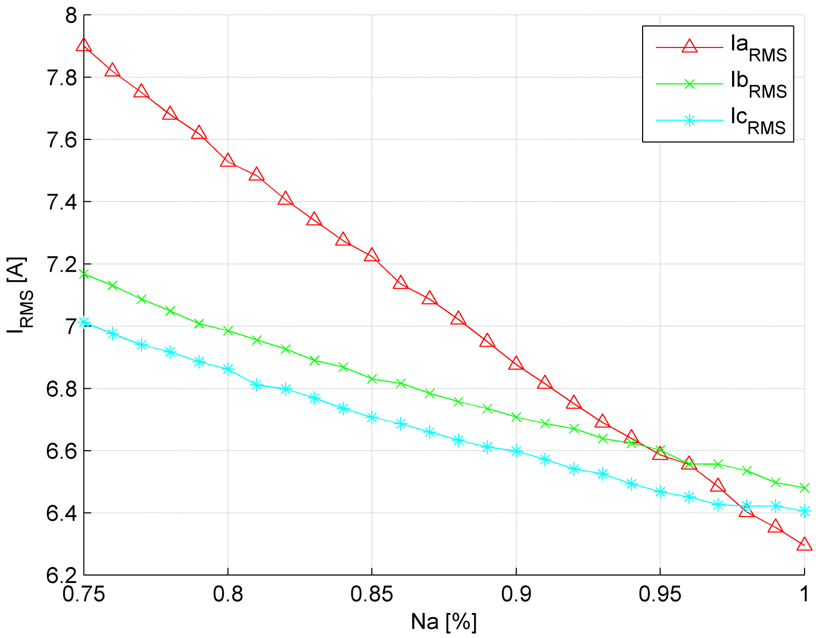

Figure 6.1: Evolution of the three RMS phase currents as a function of Na (working coils percentage) for RSE = 0% and static friction coefficient $F_S = 0.02$

Moreover, the stator phase damaged by progressive SC degradation puts in evidence a growing slope of its phase current, higher than the other ones, that increases proportionally with the said failure reported in fig. 6.1. In this diagram three signals called Ia_{RMS}, Ib_{RMS}, $and\, Ic_{RMS}$ are shown during their evolutions as a function of N_a in case of RSE equal to 0 in normal friction conditions associated with a static friction coefficient equal to 0.02 identifying two critical points called $CrossingPoints$(CPs). In CPs correspondence, the damaged RMS phase Ia_{RMS} crosses the other currents functions Ib_{RMS} and Ic_{RMS} starting from the initial conditions $N_a = 1$. Increasing Friction condition generates increasing friction torque affecting RMS as reported in fig. 5.13, but effects are quite homogeneous on all the three supply phases as RSE function. Instead the SC short circuit turn to turn induces a higher current gradient for the phase affected by the failures respect the other current gradients, following the progressive failure evolution. Analysing the magnitude track approach, used to a qualitative estimation in case of UMP unbalance magnetic pull both static and dynamic eccentricity, where RMS trend is a function of air gap reduction percentages. The current gradients, following progressive SC failure, are also dependent on air gap reduction percentages as in fig. 6.2. In these conditions(focusing on static eccentricity type and friction conditions) the current gradients change as the correlated CPs at RSE percentages equal to 50%.

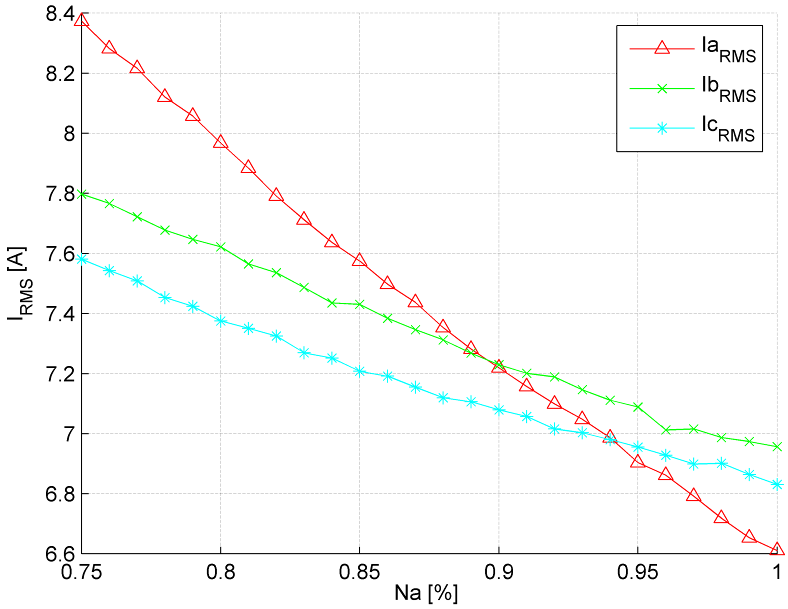

Figure 6.2: Evolution of the three RMS phase currents as Na function (working coils percentage) for RSE = 50% and static friction coefficient $F_S = 0.02$

Increasing UMP in static conditions, modifies the overall behaviour related to the proposed RMS failure map, in particular for the *crossing points* where the SC percentage of N_a associated with CPs coordinates results higher than RSE case equal to zero. Since SC degradation acts on the current phase "a" influencing the other stator electrical phases connected in balanced star phase connection, the air gap reduction is another variable to take account for a more accurate failures estimation. The system health state, as in fig 6.3, is defined by tracking crossing points between Ia_{RMS} and Ib_{RMS} evolution as a function of SC affecting the phase "a" on full RSE range.

Important information is given by the evaluation of the CPs failures maps related to short coil degradation percentage on evaluating filtered phase currents RMS, enlightening a reference cubic interpolation a least square fitting curves based on CPs scattering distribution. Around the reference cubic interpolation curve, an acceptability zone is designed by translating the reference interpolation cube to the maximum distance between scattering CPs data and reference function adding a 30% margin. This method on diagrams 6.3 and 6.4, based on CPs scattering collections allows defining 2D evaluation areas for both SC and RSE. It is evident that, the proposed diagram represents a more effective FDI tool than the other proposed failure map because identifies a well-defined RSE growing intervals avoiding areas superposition that reduces accuracy identification. The superposition evaluation areas exactly represent the main accuracy limit to distinguish degrading eccentricity percentages strongly influencing on RMS behaviours.

Indeed, both these two failure types cause different effects on the chosen prognostic precursor I_{fa} affected by the progressive short circuit and air gap eccentricity reduction in the described method. This simulation configuration is the worse case in all the possible faults combinations among the prognostic precursors, the minimum clearance between rotor and stator is associated to the minim magnetic resistance. On the contrary the progressive short circuits increase the intensity of the windings current, two opposite effects on the same prognostic precursors. It should be noted that these two failure types present evolution time scale very different on the same EMA operating conditions. In details RSE, due to mechanical wear, is correlated to a growth dynamic evolution much slower than the SC failures therefore electrical failure due to thermal wear, it is more hazardous for aircraft safety on long range flight profile. Proposed Cps failure maps technique gives an exhaustive description of the interaction between short coils degradation and rotor static eccentricity while considering the above-mentioned accuracy drawbacks due to eccentricity ranges superposition areas in the scattering diagrams.

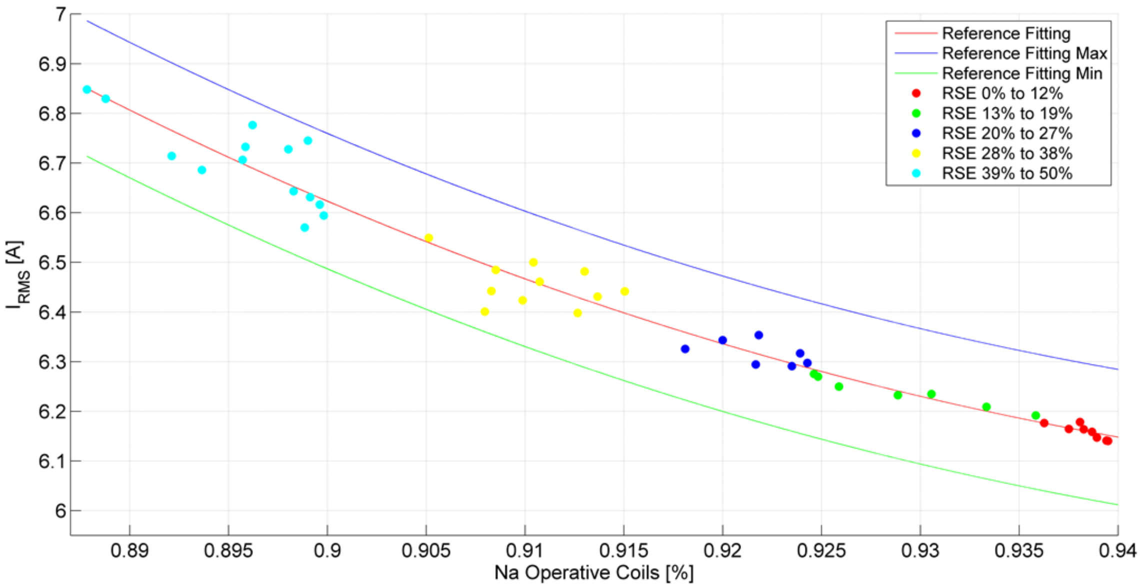

Figure 6.3: Evolution of Crossing Points between Ia_{RMS} and Ib_{RMS} as RSE full range function(0% to 50%) and progressive short coil degradation in normal friction operating conditions. The Crossing Points are classified as discrete rotor static eccentricity intervals

The above mentioned method, based on simulating all the possible SC fault combinations, may occur among all the three filtered phase currents starting from a reference SC healthy condition as in (6.1), referring to geometric rotor misalignment, where I_{fa} phase current is affected by the minimum air gap.

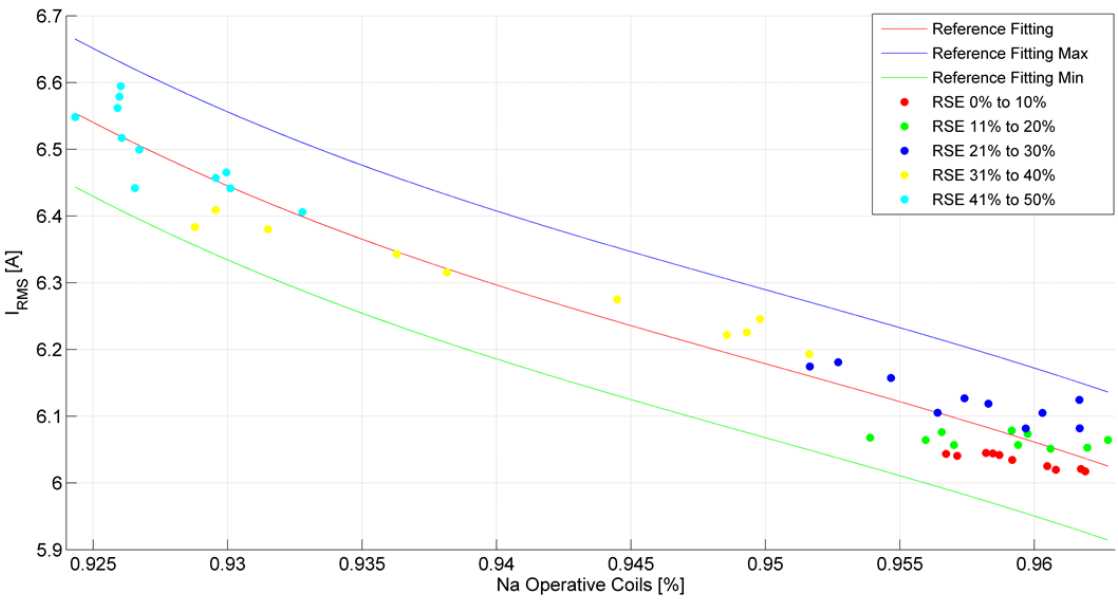

Figure 6.4: Evolution of Crossing Points between Ia_{RMS} and Ic_{RMS} as RSE full range function(0% to 50%) and progressive short coil degradation in normal friction operating conditions $F_S = 0.02$. The Crossing Points are classified as discrete RSE intervals.

It generates several failure maps collected into *SC Database* similar to the one reported in fig.6.3 for the main FDI process methodology considering also air gap reduction in RDE rotor dynamic eccentricity.

$$Ia_{RMS} < Ic_{RMS} < Ib_{RMS} \tag{6.1}$$

Other SC fault combinations are illustrated to complete an exhaustive results collection describing integration among RSE and SC failures, by focusing with the same phase I_{fa} affected by minimum rotor clearance and prognostic precursor I_{fc} with progressive thermal stress insulation damage consequential to SC incipient fault. Starting situation reported by (6.1) evolves with strong current intensity growth for I_{fc} with an increasing number of shorted windings coils, as in fig. 6.6 compared with other supply phases however involved by balancing connection to increasing current intensity, as N_c function. Unlike the previous study case the actual fault configuration identifies in 6.6 only one single CPs *crossing point* between Ic_{RMS} and Ib_{RMS} function trends. While the distance improving between Ic_{RMS} and Ia_{RMS} along SC fault improves up to 75% of operative coils. Applying the same CPs evolution among both improving rotor static eccentricity and SC degradation in fig.6.5 are showed scattering data with a wide superposition area defined on RSE ranges with interesting results where superpositions are organized with along improved magnitude current intensity for higher eccentricity range. Also, the mean distance shown in 6.6 is calculated for each N_c percentage among the punctual distance value between Ic_{RMS} and Ia_{RMS} varying RSE eccentricity percentage.

Correlation between Cps and distance failure maps, allows evaluating with some accuracy drawbacks the SC effects on three filtered phases expressed in RMS value, following the main boundary conditions varying the stator and rotor air gap reduction at fixed direction.

Consequentially changing the supply phase affected by SC in I_{fb}, fixing same boundary conditions, the RMS values start from initial healthy condition evolve with an even more divergence with a higher increasing magnitude slope, than other phases current functions. Based on evolution, respect improving rotor static eccentricity, for the study case described in fig. 6.7, the related failure maps don't describe CPs scattering data, but the mean distances between I_{fb} phase affected by SC degradation and respectively I_{fa} affected by improving RSE air gap reduction and I_{fc} phase in RMS magnitude. Due to practical constraints, this dissertation cannot provide a complete extensive reporting for all failure maps calculated by explained main FDI process, therefore in this section only RSE integration with SC progressive failure in normal friction condition is reported as the main description of the FDI model-based methodology.

The CPs and distance failure maps for improving SC short circuits, considering in normal friction operating conditions, are calculated with RDE rotor dynamic eccentricity are not presented in this dissertation, since they are similar to the results of the same FDI methodology with specific scattering data results, but they are collected within *Sc Short Coils Database* allowing a suitable evaluation for all considered failure types by comparison between real-time acquisition on aircraft ground test and the proposed model based failure maps.

6.1.1 Operating friction conditions affecting short circuit failure maps

The static friction coefficient is used as an indirect variable to evaluate transmission line wear connected to rotor driven shaft, the gearbox reducer and the aircraft surface, increasing the static friction coefficient is the same way to involve an increasing friction torque acting on EMA shaft. Considering an increasing friction torque, with the same simulation boundary conditions, it is evident that friction coefficients F_S and SC short circuit degradation affect the electromagnetic coupling in a BLDC motor with similar effects, increasing currents magnitude but with different ways as reported by harmonic results. Indeed considering the effects of static friction coefficient growing on RMS filtered phase currents in 5.13, the improving friction torque reveals a quite homogeneous RMS results improving on all three filtered phases as a function of UMP percentages both in static and dynamic eccentricity. On the contrary, as exposed in the previous section of this chapter, SC degradation, due to thermal insulation stress than mechanical wear, produces a very high slope increasing currents magnitude both for the phase affected by this electrical failure, and other phases. This physical behaviour is due by balancing supply circuit configuration as reported in fig. 6.1 as an example case. Since the physical causes are different also the effects are different, on RMS responses for the

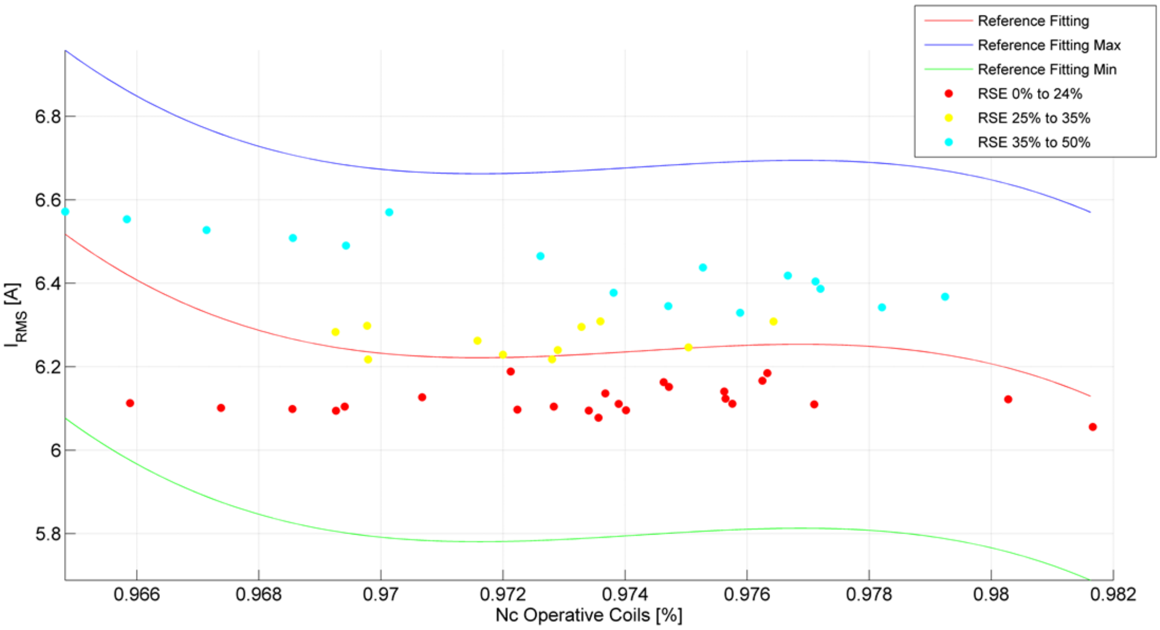

Figure 6.5: Evolution of Crossing Points between Ic_{RMS} and Ib_{RMS} as RSE full range function(0% to 50%) and progressive short coil degradation in normal friction operating conditions. The Crossing Points are classified as discrete rotor static eccentricity intervals

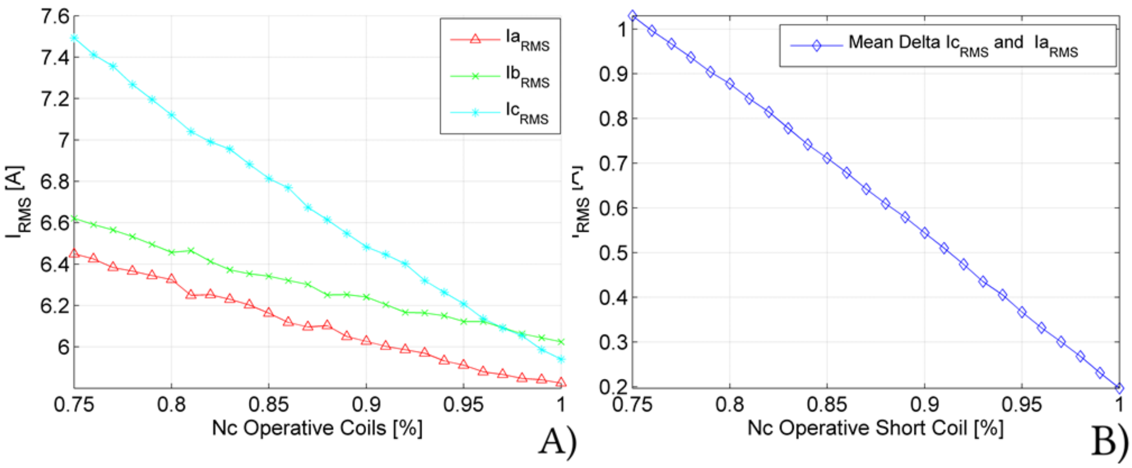

Figure 6.6: A) RMS phase currents evolution as Nc function at RSE=0% B)Main distances evolution among RSE (from 0% to50%) and SC full range function between Ic_{RMS} affected by SC degradation and the other phase currents in normal friction condition.

filtered phase currents in time dominion, the differences are described in the following reasonable approach on simulation findings:

1. SC Health Condition: where N_i operating code percentage is placed to 100%,

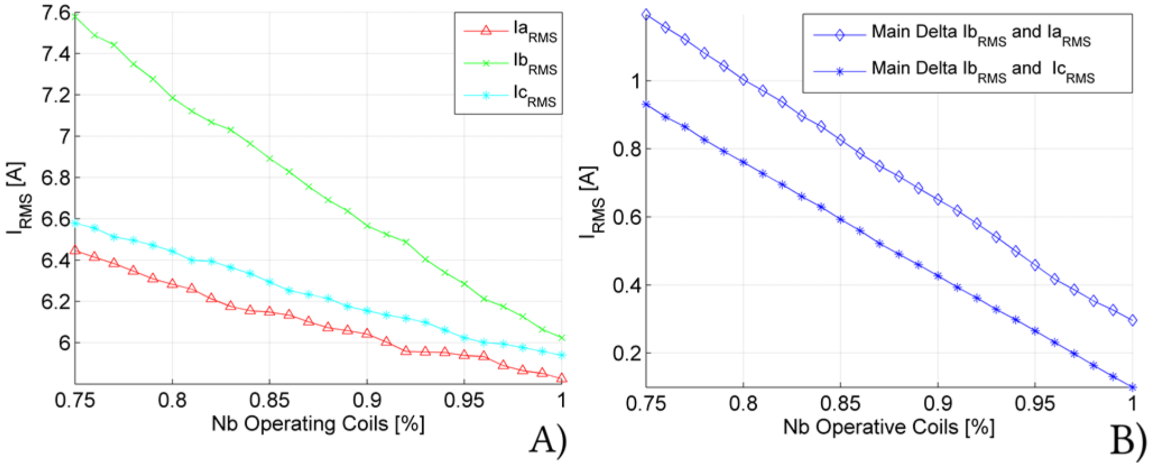

Figure 6.7: A) RMS phase currents evolution as Nb function at RSE=0% B)Main distances evolution among RSE (from 0% to50%) and SC full range function between Ib_{RMS} affected by SC degradation and the other phase currents in normal friction condition.

indicates that the phase current windings have not SC failure in progress. The initial SC healthy condition is strongly affected by F_S static friction coefficient as reported in fig. 6.8 where fixed RSE percentage the starting RMS value is the same reported in fig. 5.13 where the increasing of static friction coefficient is evaluated on RMS function of only RSE percentages.

2. Integration on RMS slope diagrams: the increasing current magnitude slopes as effects of both SC degradation and improving friction operating conditions are evident on fig. 6.8 at fixed rotor static eccentricity. Integrating the strong influence of the air gap reduction both in static and dynamic eccentricity, it should be noticed that the improved friction condition affects the RMS currents slopes not in linear mode, but with a commonly been assumed non-linear contributions. Although the linear superposition effects are still a valid approach to evaluate the integration in concurrent mode of different failures on the same prognostic precursors especially for model based approach.

3. Integration on RMS slope diagrams: the increasing current magnitude slopes as effects of both SC degradation and improving friction operating conditions are evident on fig. 6.8 at fixed rotor static eccentricity. Integrating the strong influence of the air gap reduction both in static and dynamic eccentricity, it should be noticed that the improved friction condition affects the RMS currents slopes not in linear mode, but with a commonly been assumed non-linear contributions. Although the linear superposition effects are still a valid approach to evaluate the integration in concurrent mode of different failures on the same prognostic precursors especially for model based approach.

4. Cps crossing points: the previous effects related to the introduction of improving static friction coefficients, involve the single RMS diagram where currents magnitudes are expressed as a function of SC degradation at fixed RSE percentage (the same approach is valid for RDE rotor dynamic eccentricity). The CPs failure maps, also in some SC fault combination showing the main differences about the single RMS SC diagrams, are main aggregations able to integrate SC degradation and RSE percentages. Therefore in fig. 6.9 is described as the CPS failure map with the same failure and simulation boundary conditions reported in fig. 6.4 with an exception of the static friction coefficient equal to $F_S = 0.08$. The scattering data reported in 6.4 and 6.9, are different in a number of aspects. First of all scattering data, organized in discrete RSE percentages ranges, present significant differences about each area extension. Therefore it is possible to associate a specific failure maps for each different static friction coefficients for the same simulation boundary conditions. Moreover as example, the acceptability band composed by reference interpolation curve and its upper and lower limit curves, presents extremes in correspondence of SC limits range, higher current magnitudes than the same extremes calculated for lower values of static friction coefficients.

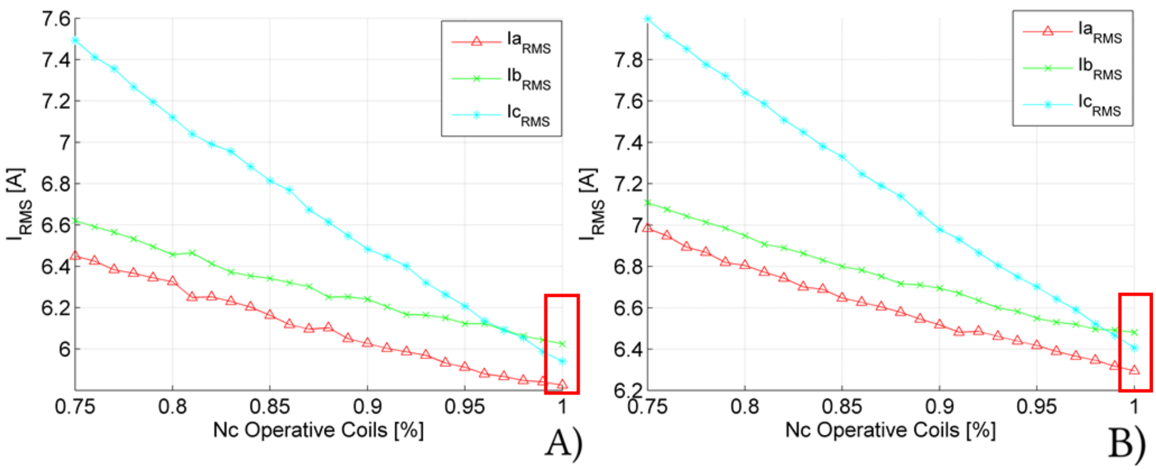

Figure 6.8: A) RMS phase currents evolution as Nc function at RSE=0% for $F_S = 0.02$ B) RMS phase currents evolution as Nc function at RSE=0% for $F_S = 0.08$. In red box are highlighted the SC healthy condition in different operating friction conditions

In conclusion, the above mentioned FDI methodology, based on RMS calculation for the prognostic precursors (the filtered phase currents) as an integrated function of SC degradation, RSE and RDE eccentricity percentage, under different friction operation conditions, allows the first evaluation about effects on prognostics failure maps. These failure maps consider all SC fault combination among all three phase supply phases, describing CPs *crossing points* scattering data or mean distances calculated among all

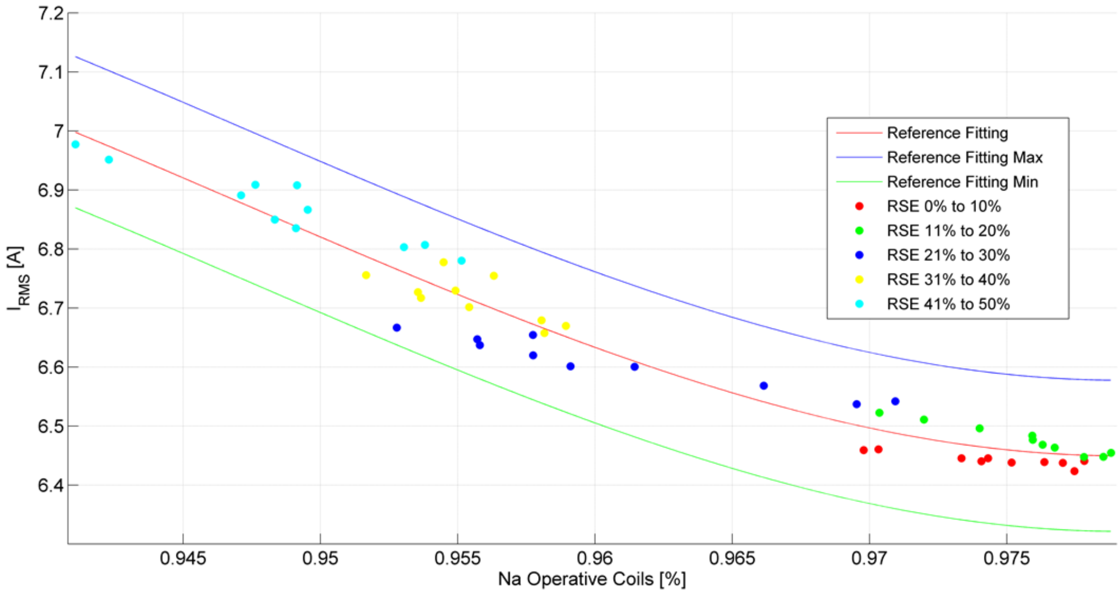

Figure 6.9: Evolution of Crossing Points between Ia_{RMS} and Ic_{RMS} as RSE full range function(0% to 50%) and progressive short coil degradation in hazardous friction operating conditions $F_S = 0.08$. The Crossing Points are classified as discrete RSE intervals.

eccentricity values at fixed SC degradation, in different friction conditions. The failure maps are stored within *SC FSx database*, as reference baseline to compare with real-time acquisition system on aircraft during on ground test described in 3.1 on page 53. The comparison between scattering data coming from model based approach, and real-time acquisition data may be affected by a small degree of uncertainty, due to aleatory or systematic approximations on acquisition system from one side, and unavoidable simplification about non linear physical behaviour performed by high fidelity simulation model even if very complex. For these reasons, a more effective approach should be developed where a small number of exceptions reducing accuracy lack it might exist, by analyzing the SC degradation impacts on harmonic analysis applied on prognostic precursors as the integration about the harmonic results achieved and described in previous section of the presented dissertation.

6.2 Short Coil degradation on Main Harmonic Amplitude

Impacts evaluation of SC degradation it must focus on what area of interest about previously developed harmonic analysis, allows achieving the most significant results for a better evaluation of how different considered failure types put together on the same prognostics variables in concurrent mode. For this target, extended simulations assessment is performed, and after analyzing harmonic results, the most significant area of interest is identified on H_{max} trend as a function of improving eccentricity percentage in different friction conditions. These harmonic results type, performed on all three supply phases, had a positive correlation to SC degradation with effects of the other failure types. How highlighted in chart 4.5 and 4.11, respectively for H_{max} trend for RSE and RDE eccentricity, in normal friction operating condition, the filtered phases amplitudes of main harmonic (referred to spectrum maximum peak amplitude) are included within a *reference band* equal to 0.06 A for RSE and 0.03 A for RDE during all eccentricity range. Taking in to account the operating friction impacts on these charts, is evident by fig.5.11, reference bands still remain constant in the first approximation. Therefore in SC healthy condition the reference bands for H_{max} amplitudes could be considered independent from improving the static friction coefficient.

In other words, the diagrams H_{max} as a function of RDE or RSE eccentricity, because a type of eccentricity excludes the other types, fixing friction operating condition, represents the SC degradation healthy condition at $N_i = 1$ corresponding to 100% operating coils, from which it begins its evolution as reported in fig 6.10 with a strong non-linear behaviour as a function of an increasing number of shorted windings.

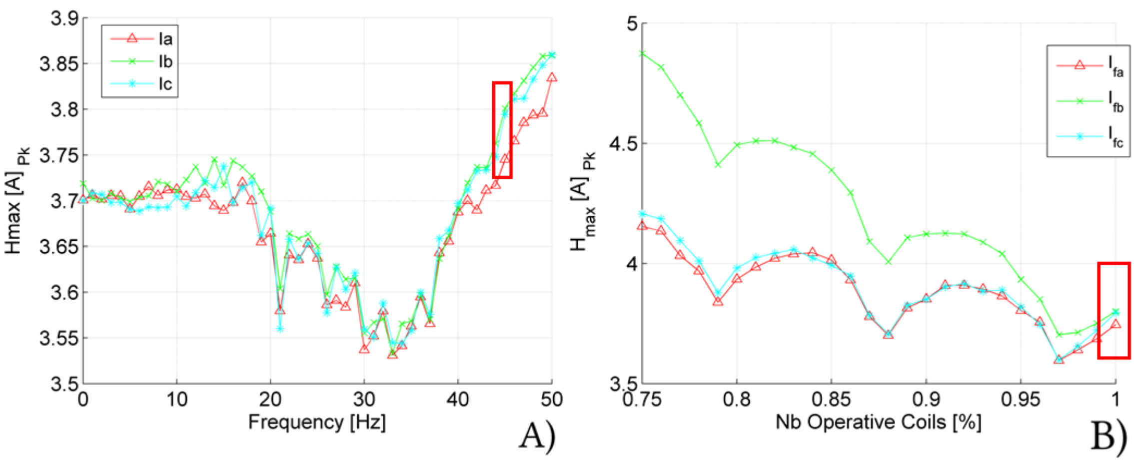

Figure 6.10: A) H_{max} evolution as SC function, in normal friction conditions $F_S = 0.02$ representing *SC Healthy Condition*at RSE full percentages range 0% to 50%). B) H_{max} evolution at RSE =45% starting from *SC Healthy Condition* highlighted in the red box.

Similarly to RMS diagrams in previous section, the filtered phase current affected by improving SC failure develops a greater magnitude trend, on equal terms of eccentricity percentage and static friction coefficient, than the other ones. All filtered phase currents increase their H_{max} with progressive SC degradation, this is due to balancing circuit in a *star* configuration with common ground. For these reason, damaged phase directly affected by SC, increased considerably their current value and electric balancing configuration distributes this increasing to the other phases. Nevertheless the air gap reduction, due to eccentricity, had a great influence on H_{max} diagrams as N_i operative coils percentage, as additional variable to consider for a more exhaustive physical behaviour description integrating of different failure types. On graph 6.11 is represented a cumulative H_{max} trends for all EMA filtered phases under increasing RDE rotor dynamic eccentricity percentage and normal friction condition, where the filtered phase current I_{fa} is affected by SC degradation. It is evident that the air gap progressive reduction increases H_{max} magnitude for both I_{fa} affected by SC degradation and the other filtered phase currents by balancing circuit configuration. Interestingly particular aspect emerges from graph 6.11 throughout this dissertation, the term *distances tracking* will be used to refer to the distances calculated at fixed SC percentage, from the phase affected by SC degradation and the other phases, tracking these values by varying the UMP unbalance magnetic pull. Completing failure integration scenario about H_{max} evolution, following the approach based on *distances tracking*, several simulations are performed varying not only SC degradation, rotor static and dynamic eccentricity , but also the static friction coefficients. The *distances tracking* on H_{max} is reported in 6.12 for normal and in 6.13 for hazardous friction conditions, with interesting findings about the quite linear behaviour of distances variable as a function of progressive SC degradation where the difference between the minimum 0% and maximum 50% air gap reduction could be considered minimal then negligible on whole eccentricity range, with a reference band equal to approximately from $0.07\,[A]$ to $0.1\,[A]$. A second interesting aspect, emerging from graph in 6.12 and 6.13, is represented by the relative weight of increasing friction operating condition, since simulation points referred to *distances tracking* are quite similar and considering graph extremes is possible to evaluate a negligible contribution.

Obviously, the reported results in this section are referred to I_{fa} affected by two progressive failures as SC degradation and rotor static and dynamic eccentricity, since the increasing friction coefficients are an indirect wear indicator affecting all the EMA system with all the three filtered phase currents. Result representation focused on this reference filtered current, allows to better evaluate how different type of failures, due to different root physical causes, integrate on the same prognostic precursors degrading primary flight control system performances. In conclusion, H_{max} difference tracking among three phase, is the principal failure maps for a robust and adequate FDI methodology able to give feedback on system health state as the integration of harmonic analysis results previously described in previous sections.

The principal approach for SC evaluation both in RMS and H_{max} behaviours, is based on evaluating the mutual trend compared with SC healthy conditions that should

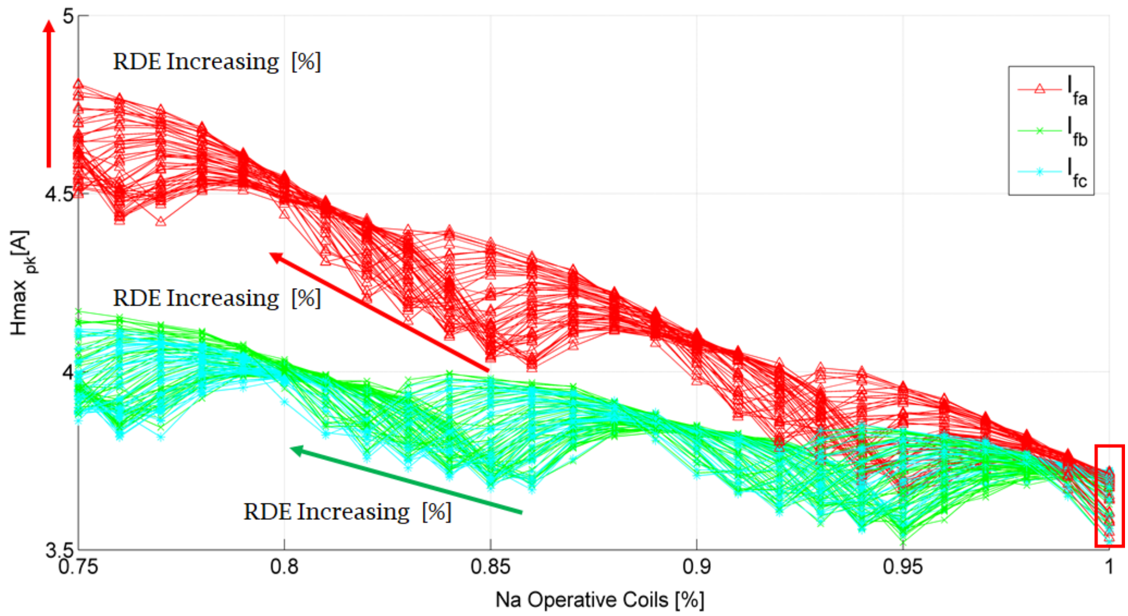

Figure 6.11: Cumulative H_{max} trends at increasing RDE dynamic eccentricity percentages (from 0% to 50%) under normal friction condition for progressive SC degradation affecting I_{fa} starting from *SC Healthy Condition* highlighted in red box .

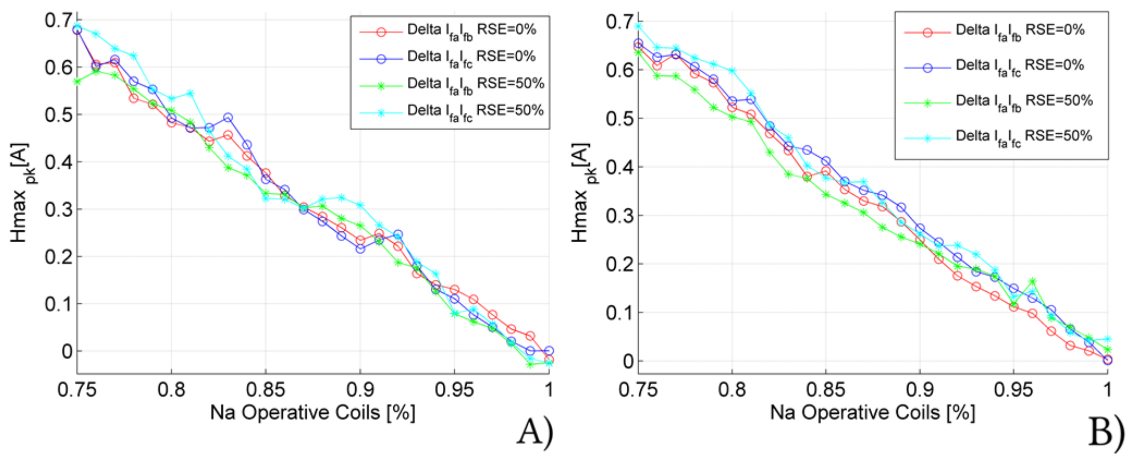

Figure 6.12: A) H_{max} distances evolution among three phase value as SC function, in normal friction conditions $F_S = 0.02$ for RSE extremes percentage range 0% and 50%. B) H_{max} distances evolution among three phase value as SC function, in hazardous friction conditions $F_S = 0.08$ for RSE extremes percentage range 0% and 50%.

be function of unbalance magnetic pull percentage (static or dynamic) under different friction conditions. Only the application of appropriate DSP parameters, to perform harmonic analysis, could highlight evidences on each failure contributing to the harmonic

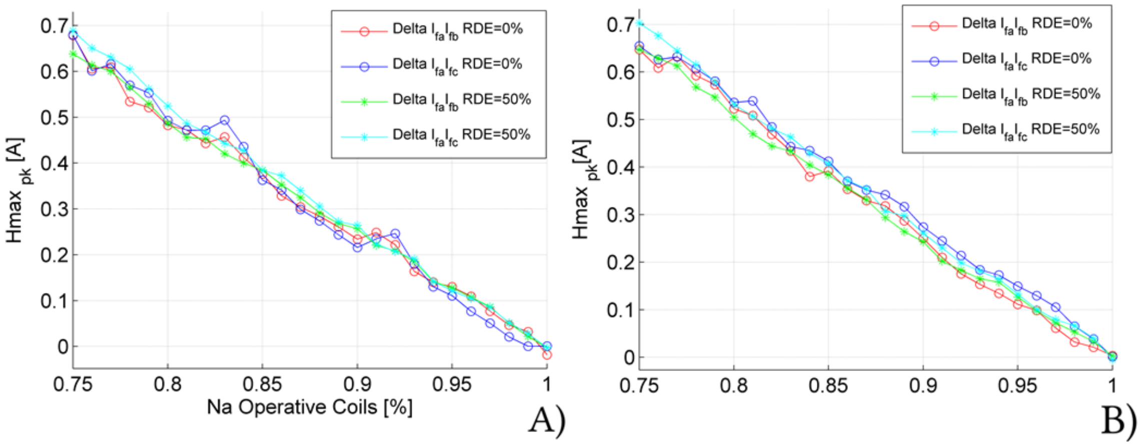

Figure 6.13: A) H_{max} distances evolution among three phase value as SC function, in normal friction conditions $F_S = 0.02$ for RDE extremes percentage range 0% and 50%. B) H_{max} distances evolution among three phase value as SC function, in hazardous friction conditions $F_S = 0.08$ for RDE extremes percentage range 0% and 50%.

responses and energetic evaluation for the proposed prognostic precursors considering that some simulated phenomena could generate opposite effects on prognostic trends.

Chapter 7

Conclusions and Future Developments

7.1 Significance of the conducted study

Despite the scientific bibliography presents numerous researches works related to different FDI approaches for synchronous and asynchronous induction motors studying a wide number of possible progressive failure modes it could be generally classified as follow suggested by [14]:

- Electronics system as ACE (Actuator and controls Electronics) with the related sensors for closed control loops like drift scaling and bias;
- The Electric system of supply stator windings as PWM system that could be affected by different short circuits faults;
- Mechanical wear and fatigue effects on backlashes, clearances in mechanical surfaces in contact as part of the mechanical transmission line;
- Structural failure on aircraft frame as aerodynamic surfaces or wing structural frame due often by dynamic vibration behaviour generating fatigue failures;

In these studies within the prognostic discipline, the primary flight control system being composed by integrated subsystem types, EMA could be degraded by different integrated failure modes. A general examination and classification about most common fault modes, could be found in [76] where a hybrid model based and data driven approach is proposed in a multi failure mode test case. One of the most important features, of the proposed model-based approach, is the multi failure modes acting in concurrent mode at the same time able to define, by offline elaborations, an extensive failure maps database to be airborne integrated into the avionic system as reference classifier to compare EMA real-time acquisition data. The multi failure modes acting in concurrent mode on the filtered phase currents coming from the integration of three physical fields (mechanical, electrical, magnetic), considered in the previous sections are the following:

- RDE Rotor Dynamic Eccentricity due to mechanical wear of EMA bearing and transmission line;
- RSE Rotor Static Eccentricity due to mechanical wear of EMA bearing and transmission line;
- SC Short circuit turn to turn due to coils insulation degradation by thermal stress;
- FSU friction static coefficient due indirectly to mechanical wear and inefficient lubrication for the transmission component;

The current findings add to a growing body of literature on harmonic analysis applications for better understanding of how different failure modes act on the same prognostic variable coming from all the primary flight control system components but focalizing on failure effects on electromagnetic interaction between rotor and Stator, overcoming multi-fault scenarios management issues. Indeed, the filtered phase currents, supplying the stator poles, are the most significant prognostic precursors from which by harmonic analysis is possible to distinguish and quantify the degradation path for each considered failure mode. This study suggests, based on results illustrated in the previous chapters, that with a proper application of RMS root mean square and FFT harmonic analysis on simulated EMA electrical supply signals, it is possible to manage with efficacy a reliable prediction of different failure modes considering both a "high-level" qualitative evaluation than a "low level" quantitative estimation of the degradation path. The simulation EMA *"high-fidelity"* model, considers different non-linearities, as described in 3.1, the dynamic system firm is strongly affected by them as demonstrated by friction model effects on all the other considered failure types. The "high-level" evaluations are based on the calculation of RMSvalue calculated during one simulation second under boundary conditions expressed in 7.1, giving a qualitative evaluation of EMA health state affected by some unavoidable ambiguity percentage but able to give a possible first warning state for health monitoring detection.

As indicated in fig. 3.1 the "high-level" evaluation is the following:

- RDE: RMS Magnitude track approach as a function of ζ equal to air gap percentage reduction and FSUx equal to different friction coefficient values;
- RSE: RMS Magnitude track approach as a function of ζ equal to air gap percentage reduction and FSUx equal to different friction coefficient values;
- SC: RMS Magnitude track approach as a function of ζ equal to air gap percentage reduction and FSUx equal to different friction coefficient values;

Qualitative estimations of the different degradation paths give a possible pre-warning alert to the FDI monitoring system, based on a comparison between the real-time acquisition system onboard and the prognostics databases results coming from simulation framework. After a pre-warning event derived from "high-level" evaluations, representing the first stage of health monitoring operations about fault detection and isolation, the proposed method implies a "low level" checks, defining fault severity evaluation, as [81], composed by following proposed approaches based on harmonic analysis:

- RSE Frequency Track approach with peak hold diagrams, H_{sb}, H_{max} as a function of ζ equal to air gap percentage reduction and FSx equal to different friction coefficients (FS is static friction coefficient and x could be referred to FS=0.02 or 0.04 or 0.08);
- RDE Frequency Track approach with peak hold diagrams, H_{max} as a function of ζ equal to air gap percentage reduction and FSx equal to different friction coefficients (FS is static friction coefficient and x could be referred to FS=0.02 or 0.04 or 0.08);
- RSE and RDE Engine Order Track approach as a function of ζ equal to air gap percentage reduction and FSx equal to different friction coefficients (FS is static friction coefficient and x could be referred to FS=0.02 or 0.04 or 0.08);
- SC frequency track approach by tracking H_{max} and related differences among all the three filtered phase currents, behaviour as a function of operative coils percentage and FSx equal to different friction coefficients (FS is static friction coefficient and x could be referred to FS=0.02 or 0.04 or 0.08);

All the FDI methodologies previously described generates from *Matlab Simulink* numerical model, a collection of harmonic results, organized into simulated databases, as reported in fig.7.1. During the pre-flight test the real-time spectrum analyser elaborates the EMA filtered phase currents, applying the same DSP parameters and RMS specification used for the boundary condition described in 3.1, comparing the real-time results with the simulated failure maps organized in onboard databases.

The combination of both "high-level" evaluation and "low-level" fault severity identification by comparison with the real-time spectrum analyser results, coming from the current probe on real EMA, give a robust response about the health state of the entire primary flight control system. An application of this study is designed for a pre-flight test as illustrated in 3.1, therefore an airborne implementation of real-time acquisition system with spectrum analyser with the DSP parameters indicated in this research. The comparison with the harmonic analysis results coming from a simulation framework, could improve a strong EMA health state evaluation increasing flight safety and reducing maintenance costs. The main algorithm for harmonic analysis is based on STFT calculated by FFT easily performed onboard by spectrum analyser hardware extensively used in the industrial and aeronautical application, as opposite to other time frequency transformations, like Wigner Ville or Wavelet transformation, requiring more complex algorithms and hardware resources. The modern avionic systems are affected by limited computational power, respect the IT hardware solutions in the customer market due to the heavy certification compliance requirements due by airworthiness regulatory. Another important contribution provided by an extensive sensitivity process, is based on different DSP parameters performing harmonic analysis on prognostic precursor give additional evidence performed on the same input time signal. The filtered phase currents simulated by EMA simulation model, are elaborated by FFT following specific DSP parameters set, only one set gives consistency findings with magnetic flux density modulation derived by air gap geometric model. In other cases, the harmonic results give less useful information about integer harmonics for the peak hold extraction, $Hmax$ main harmonic behaviour as a function RDE or RSE, and engine order tracking. Harmonic analysis is often used in rotodynamic diagnostic discipline in different declinations on vibrational characterization or Motor Current Signature Analysis (MCSA) as example in [60] [55] and [34].

With the exception of the previous bibliographic references, unfortunately some scientific studies based on FFT does not give clear information about DSP parameters set, in our opinion important information lack about how the findings are elaborated. A reasonable approach to track this issue could be to insert DSP parameter sets also to involve other elaboration path giving a more reliable contribution to the research in the prognostic field. For example in [60], analyse UMP frequency responses with a time section Δs equal to 1.64 s and frequency resolution Δf equal to 0.609 Hz.

These DSP parameters set is quite the reference value used for steam turbine generators, but there are absolutely not applicable to analyse harmonic content in MCSA elaboration during a very fast velocity changes as often happens during primary flight control surfaces activations. The choice of DSP parameters set in FFT, could be a convergence point balancing mainly frequency resolution and time section focalized on what harmonic results application and information are used for prognostics evaluations. The key problem, with this elaboration aspects, is that if the time section is too wide for the signal time evolution, the amplitude smoothing of the calculated spectrum could degenerate in losing important information about physical behaviours in frequency dominion.

Despite several similarities in the conducted study of [34] an important difference is highlighted on DSP parameters, with a frequency resolution Δf equal to 0.0381 Hz and consequently a time section Δs equal to 26.25 s introducing spectrum amplitude smoothing in case of time signal rapid changes and perhaps making necessary a stray flux measurement giving to detecting method a more reliable results. Further prognostics model-based approaches are implemented by FEM analysis integrated with statistical methodology, trying to compensate a poor experimental database for data driven approach as the hybrid approach used by [76]. The main drawbacks of using FEM model are referred to the extensive elaboration time needed to compute up to convergence to suitable fitness functions (e.g. L1-norm or L2-norm error) as proposed by [6].

The off-line simulation framework presented in this research work had a great added value to be a *high-fidelity* model overcoming lack of experimental data, with simulation time of more than one order less than required for finite element simulations. The finite element analysis is surely a more accurate approach for what concerning a specific physical simulation, indeed often is used as indirect validation for other less accurate numerical models. But in multibody or multi-disciplinary requirements approach requested to this study case satisfied by *high-fidelity* model, an extreme accuracy could be balanced by a more fast and flexible simulation model. If the *high-fidelity* approach is able to reproduce with acceptable accuracy the physical phenomena under different evolution parameters, like progressive multi failure modes, the faster and more flexible (as quick reconfiguration with different technical parameters) computational algorithm balances the accuracy loss achieving the main research target to deploy a smart and robust FDI procedure.

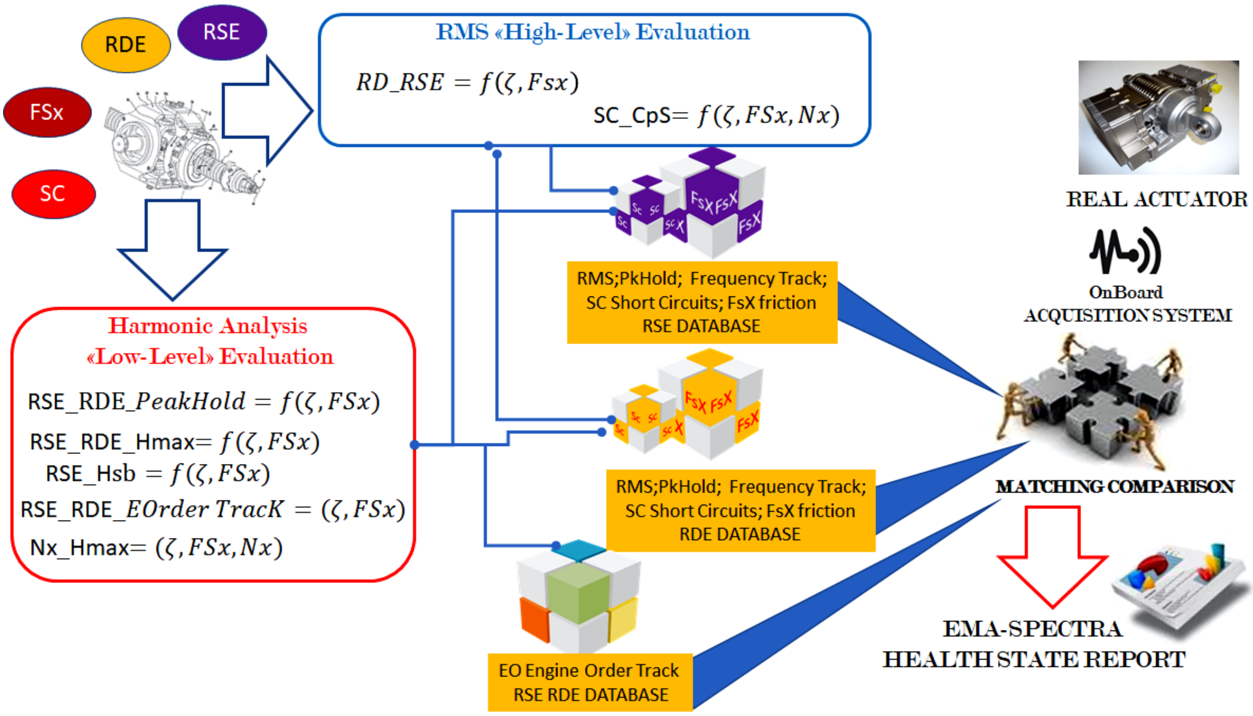

Figure 7.1: Main FDI process proposed in this research work with four failure modes acting on the same time in concurrent mode at the same prognostic variables.

7.2 Limitation of the Current Study

As previously described in this research work, the primary flight control system is slowly involved in EMA application, actually being confined to prototypes or UAVs [48] and secondary flight control system as illustrated by [66], with the consequence of very limited experimental data on flight acquisitions. Therefore, a strong need to develop a flexible (adaptable to wide EMA technical configuration) and robust model-based approach is rising, to identify detect and evaluate more than one failure mode in concurrent evolution on the same actuator, becoming the main target of this research trying to overcome safety issues. Since historical experimental data, about EMA operating condition on aircraft, are not suitable due to limited employment on civil and military aircraft fleets, also in the bibliography the scientific paper with experimental validation for prognostics algorithms on EMA are very limited and not ever useful for comparison analogies with the proposed study.

A multi failures EMA framework is presented in this research, it doesn't find a direct experimental validation, but some experimental findings in the literature about induction motor failures, could be useful even if similar multi failure in concurrent mode approach is not found. Indeed the bibliographic references on EMA could be organized by two failure types:

- **electrical failure** as example short circuits failure inducted in experimental laboratory by [36] and [34] where stray flux measures are combined with MCSA for detecting process;
- **mechanical wear failures**, related to RSE and RDE as indicated by [28] experimental campaigns on induction motor in different electric supply circuit configurations in cage induction motors and [55] for the synchronous machine;

The experimental investigation of [28] represents in this field a strong reference in the FDI discipline for induction motors affected by rotor eccentricity both static and dynamic evaluating the UMP in the laboratory for different supply windings stator circuits (parallel or series configuration), and a blank rotor. A more dumped UMP responses are measured in parallel than series windings connections, from different test bench configurations. All the experimental results in the bibliography, for eccentric rotor on induction actuator related to the asynchronous motor with squirrel cage rotor configuration, could not very significant as indirect validation reference for the model approach based on BLDC synchronous motor, therefore they are neglected.

On the other side the [36] and [34] experimental bench, uses improved experimental diagnostic instruments to detect stator coils faults based on both phase current analysis and stray axial flux. Also, in this approach [34] highlights that the stray flux analysis is affected by two main drawbacks: the first is the weakness of magnetic acquired signal sensible to external electromagnetic disturbances, the second is the presence of inherent asymmetries in low voltage motor associated with false fault identifications with high probability. A partial indirect validation could be possible, finding conducted in a similar way supported by direct experimental validation process, finding analogies with the main FDI approach based on simulated failure maps. Indeed also [35] and [61], encouraging to refer as indirect validation to [60], where a UMP model is validated experimentally for a gas turbine generator with long flexible rotor shaft, based on the same air gap geometric model used for this research. In the conducted experimental validation, the 2X and 1X engine orders are present as main indicators for increasing UMP due to air gap reduction reported as classical turbine dynamic responses in the eccentric rotor in [78] and in other rotordynamic scientific books. Engine order approach described, in chapter 5 on 95, is referred to EMA short shaft rotor configuration highlighting more significant engine orders extracted and tracked by harmonic analysis algorithm, during speed transient to maximum rotational speed taking into account another excitation causes due to EMA physical configuration. For what concerning the harmonic analysis results, presented for frequency track approaches to evaluate RSE and RDE, the uneven harmonic numbers extracted by peak hold filter could find a similar correspondence in [55], where the proposed model is supported by experimental validation. Also, this indirect validation was limited by motor speed range up to 1800 RPM less than the half speed range of EMA used by the simulation model for the primary flight control system. The findings in the proposed model-based approach are subject to at least two limitations, in the simulated EMA behaviour model:

- **dynamic behaviour in structural resonance**: the harmonic analysis proposed is based on EMA simulation conditions away from natural structural resonance conditions for primary flight system components and aircraft frame. In this specific condition, the main maximum frequency H_{max} for prognostic precursors could be influenced by structural resonances defining as output different frequencies and magnitudes respect to calculated ones coming from a model-based approach and collected in failure maps databases. Since some design structural requirements for integration between avionic systems and structural frames provides in all operating conditions to avoid working in resonance structural conditions this limitation is also mitigated by proposed boundary conditions of a pre-flight test designed for the FDI algorithms to compare experimental real-time spectrum with the simulated failure maps results.

- **temperature influence on filtered phase current**: the numerical simulation model doesn't consider the operating temperature influence on motor operating parameters as reported [44]. To overcome the temperature and other physical influencing factors like aerodynamic forces on aircraft control surfaces, inertial loads and system actuation characteristics (activations number, duration, actuation nature) a preflight procedure is identified as main operating condition as [24] limiting environmental uncertainties by imposing a reference temperature of 25℃.

Summarizing the proposed boundary conditions for preflight on ground test described in 3.1, defining a robust standard, in which FDI methodology used for calculating failure maps database could be effectively performed to compare model based results with experimental data driven evaluation logic defining EMA health state. The data drive evaluation logic based on main comparisons, between model-based findings and experimental real-time acquisitions, gives as output a Health state reports for each pre-flight test performed on the ground for each EMA installed to drive aerodynamic surfaces on aircraft. The collection of Health state reports is designed to build a historical experimental database very useful to perform on aircraft an assessment highlighting the degradation path for different fault modes presented in this research improving maintenance process requirements improving safety and reducing costs. In additional the historical experimental databases should be useful for the off-line prognostic evaluations used to calculate, by statistical methods as suggested by [8], the RUL interrelating flight data based on wide numerical evidence on entire aircraft fleets.

7.3 Recommendation for future research

The presented study is limited to deploy a robust FDI methodology by driving a model-based approach on a specific EMA test case defined by simulation technical parameters granted an acceptable accuracy and repetitiveness, further installation of a comparison avionic system connected to a real-time acquisition and elaboration framework needs to be developed in research next steps. These findings suggest several course actions for both improving simulation accuracy, based on time frequency transformations, and practical deployment application on real aircraft. The future research regarding improvements for EMA simulation high fidelity models, would be very interesting by adding for example operative environment temperature as an independent variable affecting some motor technical simulation parameters not included in this study.

Another interesting evolution for future research based on this study could extend the simulation numerical model and the proposed FDI methodology based on harmonic analysis to different type of PWM sinusoidal commutation control BLDC motor. This tread could give interesting results within difference analysis between the proposed trapezoidal commutation logic and the sinusoidal one eliminating the torque ripple and commutation spikes associated with trapezoidal commutation. The research findings in previous chapters represent the model-based approach on which a comparison data driven evaluation logic could be provided by a real-time acquisition system where an avionic elaboration component connected to EMA phase currents probes apply the same harmonic analysis logic used for the simulation framework. The data comparison with the failure maps stored in database onboard, gives an *EMA Health State Report*, which could be stored to improve the maintenance process and reducing costs by tracing historical data about different progressive failure modes.

The design of the real-time acquisition system, integrated with other avionic systems, represents unequivocally the final work to complete the prognostic field set developed in this study. But it's in our intention to point out the following insight for the final target: a direct experimental evaluation to tune the simulation results coming from harmonic analysis following a dedicated evaluation plan. Although the boundary conditions, proposed to set the FDI algorithms and related harmonic results organized off line databases, give valid mitigation for environment uncertainties evaluating the EMA health state, an experimental validation in the laboratory could well assets the simulation limits. On the contrary, in the presence of experimental noise or uncertainty, the proposed failure maps could be verified as frequency and order reference masks to filter the experimental harmonic results, validating the health state responses with controlled degradation path in the laboratory.

More information on the health state of the primary flight control system could be established by harmonic analysis on MCSA , by comparing in time and frequency dominion evaluating torsional vibration of the entire transmission line with an improving degradation wear path. This approach should be defined as *phase delay analysis* and based on the main philosophy to use EMA as a sensor of itself, analysing the phase displacement of the filtered phase currents with cinematic joints lability of cinematic line that could induce torsional vibrations.

In conclusion this research has thrown up many possibilities and open questions in need for further investigation but represent for many points of view a suitable demonstration that the interaction between mechanical, magnetic and electrical field in EMA could give a suitable FDI approach for early detection of four different failure modes. The importance of a robust assessment for DSP is a central activity to use with efficacy FFT for harmonic analysis on prognostic precursors used in this study, the filtered phase currents, demonstrating by findings an accurate methodology to evaluate correctly the simulated EMA health state.

Acronyms

FDI Fault Detection and Identification

EMA Electro Mechanical Actuator

EHA Electro Hydrostatic Actuator

AEA All Electric Aircraft

PHM Prognostics and Health Management

CBM Condition Based Maintenance

FTA Fault Tree Analysis

RUL Remaining Useful Life

HSA Hydraulic Servo Actuators

RAMS Reliability Availability Maintainability Safety

FEA Finite Element Analysis

BLDC Brushless Direct Current Electric Motor

FMECA Failure modes effects and critical analysis

BIST Built In Self-Test

Eu Engineering Unit

FBW Fly By Wire

MEA More Electric Aircraft

TRU Transformer Rectifier Unit

VSCF Variable Speed Constant Frequency

IDG Integrated Drive Generator

CSD Constant Speed Drive

HVDC High Voltage Direct Current

LVDT Linear Variable Displacement Transducer

PWM Pulse Width Modulation

ECM	Electronically Commutated Motors
EMF	Electro Motive Force
RVDT	Rotary Variable Differential Transformer
RE	rotary encoder.
FOC	Field Oriented Control
CEMF	Counter Electro Motive Force
RSE	Rotor Static Eccentricity
ADC	Analogical To Digital Conversion
FEM	Finite Element Methods
SC	Short Circuit
RDE	Rotor Dynamic Eccentricity
FSU	Friction Static User coefficient
ADREP	Aviation Data Reporting Program
IATA	International Air Transport Association
ICAO	International Civil Aviation Organization
BC	Boundary Conditions
FT	Fourier Transformation
STFT	Short Time Fourier Transformation
FS	Fourier Series
DFT	Discrete Fourier transformation
STDFT	Short Time Discrete Fourier Transformation
DFS	Discrete Fourier Series
FFT	Fast Fourier Transformation
DSP	Digital Signal Processing
RMS	Root Mean Squared

PSD Power Spectral Density

RPM Round Per Minutes

EO Engine Order

BPF Blade Pass Frequency

UMP Unbalance Magnetic Pull

CP Crossing Point

MCSA Motor Current Signature Analysis

ATRU Auto-Transformer Rectifier Unit

Appendix A

Electromechanical Actuator Technical Simulation Parameters

Brushless DC-Servomotors

2 Pole Technology

190 mNm
232 W

Series 4490 ... B

	Values at 22°C and nominal voltage	4490 H		024 B	036 B	048 B	
1	Nominal voltage	U_N		24	36	48	V
2	Terminal resistance, phase-phase	R		0,22	0,44	0,7	Ω
3	Efficiency, max.	$\eta_{max.}$		87	87	87	%
4	No-load speed	n_0		9 700	10 400	10 800	min^{-1}
5	No-load current, typ. (with shaft ø 6 mm)	I_0		0,527	0,397	0,317	A
6	Stall torque	M_H		2 635	2 760	2 978	mNm
7	Friction torque, static	C_0		4,96	4,96	4,96	mNm
8	Friction torque, dynamic	C_V		$7{,}72 \cdot 10^{-4}$	$7{,}72 \cdot 10^{-4}$	$7{,}72 \cdot 10^{-4}$	mNm/min^{-1}
9	Speed constant	k_n		395	283	220	min^{-1}/V
10	Back-EMF constant	k_E		2,53	3,54	4,56	mV/min^{-1}
11	Torque constant	k_M		24,2	33,8	43,5	mNm/A
12	Current constant	k_I		0,041	0,03	0,023	A/mNm
13	Slope of n-M curve	$\Delta n / \Delta M$		3,6	3,7	3,5	min^{-1}/mNm
14	Terminal inductance, phase-phase	L		73	142	235	µH
15	Mechanical time constant	τ_m		4,9	5	4,8	ms
16	Rotor inertia	J		130	130	130	gcm²
17	Angular acceleration	$\alpha_{max.}$		203	212	229	·10³rad/s²
18	Thermal resistance	R_{th1} / R_{th2}	0,96 / 3,9				K/W
19	Thermal time constant	τ_{w1} / τ_{w2}	23 / 1 222				s
20	Operating temperature range:						
	– motor		-30 ... +125				°C
	– winding, max. permissible		+125				°C
21	Shaft bearings		ball bearings, preloaded				
22	Shaft load max.:						
	– with shaft diameter		6				mm
	– radial at 3 000 min^{-1} (5 mm from mounting flange)		113				N
	– axial at 3 000 min^{-1} (push only)		45				N
	– axial at standstill (push only)		135				N
23	Shaft play:						
	– radial	≤	0,015				mm
	– axial	=	0				mm
24	Housing material		aluminium, black anodized				
25	Mass		742				g
26	Direction of rotation		electronically reversible				
27	Speed up to	$n_{max.}$	18 000				min^{-1}
28	Number of pole pairs		1				
29	Hall sensors		digital				
30	Magnet material		NdFeB				
	Rated values for continuous operation						
31	Rated torque	M_N		148	139	137	mNm
32	Rated current (thermal limit)	I_N		7,45	5,06	3,91	A
33	Rated speed	n_N		9 650	10 470	10 930	min^{-1}

Note: Rated values are calculated with nominal voltage and at a 22°C ambient temperature. The R_{th2} value has been reduced by 25%.

Note:

The diagram indicates the recommended speed in relation to the available torque at the output shaft for a given ambient temperature of 22°C.

The diagram shows the motor in a completely insulated as well as thermally coupled condition (R_{th2} 50% reduced).

The nominal voltage (U_N) curve shows the operating point at nominal voltage in the insulated and thermally coupled condition. Any points of operation above the curve at nominal voltage will require a higher operating voltage. Any points below the nominal voltage curve will require less voltage.

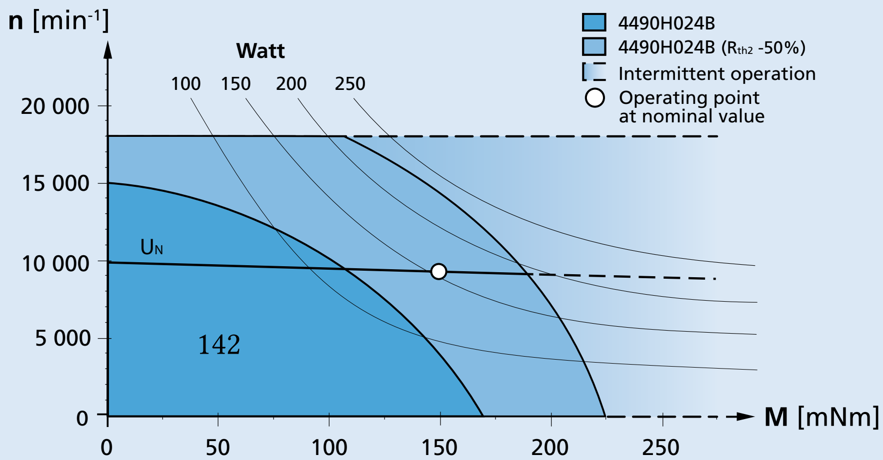

Recommended operation areas (example: nominal voltage 24 V)

Dimensional drawing

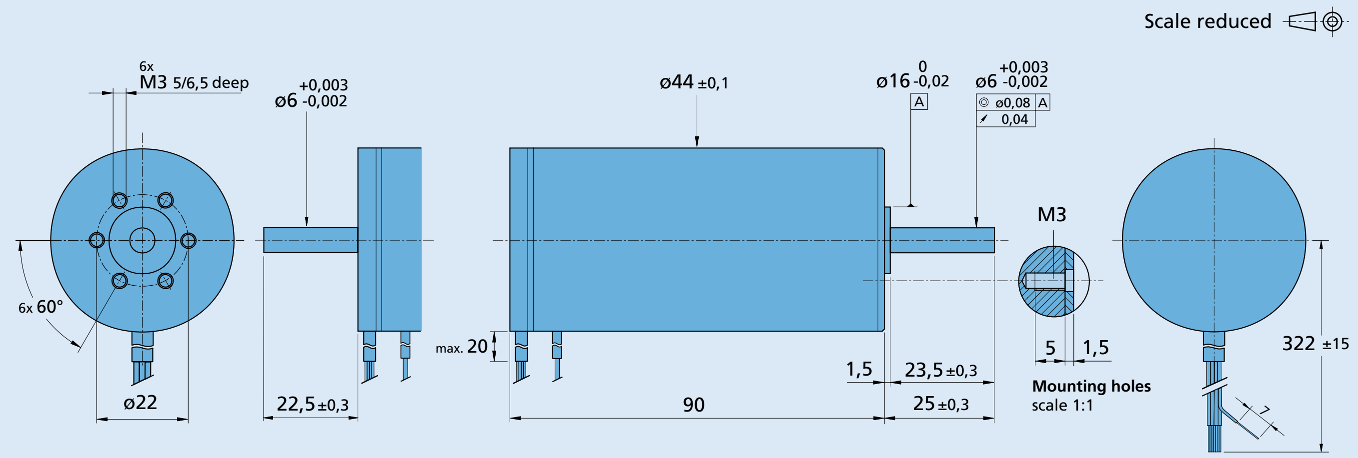

4490 H ... B - K312 **4490 H ... B**

Option, cable and connection information

Example product designation: **4490H024B-K1155**

Option	Type	Description
K1155	Controller combination	Analog Hall sensors for combination with Motion Controller MCBL
K1026	Sensorless	Motor without Hall sensors
K1838	Encoder combination	Motor with rear end shaft for combination with Encoder IE3
K312	Encoder combination	Motor with rear end shaft for combination with Encoder HEDS/HEDL/HEDM
K3051	Encoder combination	Motor with rear end shaft for combination with Encoder AES
K179	Bearing lubrication	For vacuum of 10^{-5} Pa @ 22°C

Connection

Function	Colour
Phase C	yellow
Phase B	orange
Phase A	brown
GND	black
U_{DD} (+5V)	red
Hall sensor C	grey
Hall sensor B	blue
Hall sensor A	green

Standard cable

Single wires, material PTFE
AWG 16: Phase A/B/C
AWG 26: Hall A/B/C, U_{DD}, GND

Product combination

Precision Gearheads / Lead Screws	Encoders	Drive Electronics	Cables / Accessories
38A 44/1	HEDS 5500 IE3-1024 IE3-1024 L HEDL 5540 AES-4096	SC 5004 P SC 5008 S MCBL 3006 S MC 5010 S	MBZ To view our large range of accessory parts, please refer to the “Accessories” chapter.

Table A.1: Technical Parameters used for Simulink EMA Model, integrating Faulhaber Series 4490 and [51]

Error proportional gain	G_{prop}	105	$-$
PID controller: proportional gain	GAP	0.05	$\frac{Nms}{rad}$
PID controller: integrative gain	GAI	0	$\frac{Nm}{rad}$
PID controller: derivative gain	GAD	0	$\frac{Nms^2}{rad}$
Maximum power supply voltage	V_{max}	48	V
Maximum current	I_max	22.5	A
Maximum motor torque	$T_{m,max}$	1.689	Nm
Torque constant	k_t	0.0752	$\frac{Nm}{A}$
Back-EMF constant	k_e	0.0752	$\frac{V_s}{rad}$
Phase-to-phase resistance	R_s	2.13	Ω
Phase-to-phase inductance	L_s	$7.2 \cdot 10^{-4}$	H
RL time constant of BLDC motor	$\tau_R Ls$	$\frac{R_s}{L_s}$	s
Polar expansions per phase	$2P$	4	$-$
Number of polepairs per phase	P	2	$-$
Current hysteresis band width	hb	0.5	A
Moment of inertia of the motor	J_m	$1.3 \cdot 10^{-5}$	$kg \cdot m^2$
Viscous damping coefficient of the motor	C_m	$\frac{30}{\pi} \cdot 10^{-6}$	Nms/rad
Moment of inertia of the user	J_u	$1.2 \cdot 10^{-5}$	$kg \cdot m^2$
Viscous damping coefficient of the user	C_u	$4.5 \cdot 10^{-7}$	$\frac{Nms}{rad}$
Static friction torque of the motor	f_{sm}	$0.06 \cdot T_(m, max)$	Nm
Dynamic friction torque of the motor	f_{dm}	$\frac{f_s m}{2}$	Nm
Static friction torque of the user	f_{su}	$0.04 \cdot T_(m, max)$	Nm
Dynamic friction torque of the user	f_{du}	$\frac{f_{su}}{2}$	Nm
Nominal backlash	BLK	$5 \cdot 10^{-3}$	rad

Bibliography

[1] *"Aircraft Electric Power Characteristics," MILSTD-704F, 12 March 2004.* Departement of Defence, Mar. 2014. URL: http://everyspec.com/MIL-STD/MIL-STD-0700-0799/MIL-STD-704F_1083/.

[2] *"FLIGHT CONTROL SYSTEMS - DESIGN, INSTALLATION AND TEST OF" MIL-DTL-9490E PILOTED AIRCRAFT, GENERAL SPECIFICATION FOR.* Departement of Defence, June 1975. URL: http://everyspec.com/MIL-SPECS/MIL-SPECS-MIL-DTL/MIL-DTL-9490E_10979/.

[3] R. Aalmoes et al. "Performance improvements for calculations of third party risk around airports". In: *Safety and Security Engineering V*. WIT Press, Sept. 2013. DOI: 10.2495/safe130401. URL: https://doi.org/10.2495%2Fsafe130401.

[4] Reyad Abdel-Fadil, Ahmad H. A. Eid, and Mazen Abdel-Salam. "ELECTRICAL DISTRIBUTION POWER SYSTEMS OF MODERN CIVIL AIRCRAFTS". In: 2013.

[5] Reyad Abdel-Fadil, Ahmad Eid, and Mazen Abdel-Salam. "Fuzzy logic control of modern aircraft electrical power system during transient and steady-state operating conditions". In: *2014 IEEE International Conference on Power Electronics, Drives and Energy Systems (PEDES)*. IEEE, Dec. 2014. DOI: 10.1109/pedes.2014.7042125. URL: https://doi.org/10.1109%2Fpedes.2014.7042125.

[6] Seghiour Abdellatif et al. "Multi-Class Classification Approach for the Diagnosis of Broken Rotor Bars based on Air-Gap Magnetic Flux Density". In: *Electrotehnică, Electronică, Automatică* 65 (Jan. 2017), pp. 31–39.

[7] EP Abrahamson et al. "Failure by delamination during wear". In: *Proc. Workshop on Failure Analysis and the SEM*. 1974, pp. 889–894.

[8] Vachtsevanos; Andrea De Martin; Giovanni Jacazio; George. "Windings fault detection and prognosis in electro-mechanical flight control actuators operating in active-active configuration". In: *INTERNATIONAL JOURNAL OF PROGNOSTICS AND HEALTH MANAGEMENT, vol. 8 n. 2.* 8.2 (2107). ISSN: ISSN 2153-2648. URL: http://porto.polito.it/2686857/.

[9] Ruben Dario Hernández Beleño et al. "Dynamic Modeling and PID Control of an Underwater Robot Based on the Hardware-in-the-Loop Method". In: *International Review of Mechanical Engineering (IREME)* 10.7 (Nov. 2016), p. 482. DOI: 10.15866/ireme.v10i7.9037. URL: https://doi.org/10.15866%2Fireme.v10i7.9037.

[10] Maggiore Paolo Belmonte Dario DAlla Vedova Matteo DAvide Lorenzo. "Onboard Electromechanical Actuators Affected by Motor Static Eccentricity: a New Prognostic Method based on Spectral Analysis Techniques". In: *New Developments in Pure and Applied Mathematics*. Ed. by WSEAS Press. WSEAS Press, Mar. 2015. URL: http://hdl.handle.net/11583/2604987.

[11] D. Belmonte et al. "Electromechanical actuators affected by multiple failures: Prognostic method based on spectral analysis techniques". In: Author(s), 2017. DOI: 10.1063/1.4981960. URL: https://doi.org/10.1063%2F1.4981960.

[12] D Belmonte, M Vedova, and P Maggiore. "Electromechanical servomechanisms affected by motor static eccentricity: Proposal of fault evaluation algorithm based on spectral analysis techniques". In: *Safety and Reliability of Complex Engineered Systems*. CRC Press, Sept. 2015, pp. 2365–2372. DOI: 10.1201/b19094-310. URL: https://doi.org/10.1201%2Fb19094-310.

[13] Dario Belmonte. "Modelli di Simulazione Innovativi con logiche di controllo e recupero asimmetria in presenza di avaria per comandi di volo secondari". MA thesis. Politecnico di Torino Dipartimento ingegneria Aerospaziale, Apr. 2011.

[14] Dario Belmonte, Matteo Davide Lorenzo Dalla Vedova, and Paolo Maggiore. "Prognostics of Onboard Electromechanical Actuators: a New Approach Based on Spectral Analysis Techniques". In: *International Review of Aerospace Engineering (IREASE)* 11.3 (June 2018), p. 96. DOI: 10.15866/irease.v11i3.13796. URL: https://doi.org/10.15866%2Firease.v11i3.13796.

[15] N. Bianchi et al. "Comparison of PM motor structures and sensorless control techniques for zero-speed rotor position detection". In: *37th IEEE Power Electronics Specialists Conference*. IEEE. DOI: 10.1109/pesc.2006.1712039. URL: https://doi.org/10.1109%2Fpesc.2006.1712039.

[16] L Borello and MDL Dalla Vedova. "A dry friction model and robust computational algorithm for reversible or irreversible motion transmission". In: *International Journal of Mechanics and Control (JoMaC)* 13.02 (2012), pp. 37–48.

[17] Lorenzo Borello, Giuseppe Villero, and Matteo DL Dalla Vedova. "Flap failure and aircraft controllability: Developments in asymmetry monitoring techniques". In: *Journal of Mechanical Science and Technology* 28.11 (2014), pp. 4593–4603.

[18] Lorenzo Borello, Giuseppe Villero, and Matteo Dalla Vedova. "New asymmetry monitoring techniques: Effects on attitude control". In: *Aerospace Science and Technology* 13.8 (Dec. 2009), pp. 475–487. DOI: 10.1016/j.ast.2009.07.006. URL: https://doi.org/10.1016%2Fj.ast.2009.07.006.

[19] L Borello et al. "A comparison between Dry Friction Discontinuous Computational Algorithms". In: *27th International Congress of the Aeronautical Sciences ICAS*. 2010.

[20] L. Cohen. "Time-frequency distributions-a review". In: *Proceedings of the IEEE* 77.7 (July 1989), pp. 941–981. DOI: 10.1109/5.30749. URL: https://doi.org/10.1109%2F5.30749.

[21] Leon Cohen. "Generalized Phase-Space Distribution Functions". In: *Journal of Mathematical Physics* 7.5 (May 1966), pp. 781–786. DOI: 10.1063/1.1931206. URL: https://doi.org/10.1063%2F1.1931206.

[22] James W. Cooley and John W. Tukey. "An Algorithm for the Machine Calculation of Complex Fourier Series". In: *Mathematics of Computation* 19.90 (Apr. 1965), p. 297. DOI: 10.2307/2003354. URL: https://doi.org/10.2307%2F2003354.

[23] S.M.A. Cruz and A.J.M. Cardoso. "Diagnosis of Stator Inter-Turn Short Circuits in DTC Induction Motor Drives". In: *IEEE Transactions on Industry Applications* 40.5 (Sept. 2004), pp. 1349–1360. DOI: 10.1109/tia.2004.834012. URL: https://doi.org/10.1109%2Ftia.2004.834012.

[24] Matteo Dalla Vedova et al. "Identification of precursors of servovalves failures for implementation of an effective prognostics". In: *Proceedings of the 4th International Conference on Recent Advances in Aerospace Actuation Systems and Components*. 2010, pp. 111–126.

[25] MDL Dalla Vedova et al. "Linear Electromechanical Actuators affected by Mechanical Backlash: a Fault Identification Method based on Simulated Annealing Algorithm." In: *WSEAS transactions on systems* (2015), pp. 268–276.

[26] J.R. Dormand and P.J. Prince. "A family of embedded Runge-Kutta formulae". In: *Journal of Computational and Applied Mathematics* 6.1 (Mar. 1980), pp. 19–26. DOI: 10.1016/0771-050x(80)90013-3. URL: https://doi.org/10.1016%2F0771-050x%2880%2990013-3.

[27] John R. Dormand. "Differential equations". In: *Numerical Methods for Differential Equations*. CRC Press, May 2018, pp. 1–14. DOI: 10.1201/9781351075107-1. URL: https://doi.org/10.1201%2F9781351075107-1.

[28] D.G. Dorrell and A.C. Smith. "Calculation and measurement of unbalanced magnetic pull in cage induction motors with eccentric rotors. Part 2: Experimental investigation". In: *IEE Proceedings - Electric Power Applications* 143.3 (1996), p. 202. DOI: 10.1049/ip-epa:19960284. URL: https://doi.org/10.1049%2Fip-epa%3A19960284.

[29] M. Fadel. "Position Control for Laws for Electromechanical Actuator". In: *2005 International Conference on Electrical Machines and Systems*. IEEE, 2005. DOI: 10.1109/icems.2005.202846. URL: https://doi.org/10.1109%2Ficems.2005.202846.

[30] Alessandro Falaschi. *Elementi di trasmissione dei segnali e sistemi di telecomunicazione*. Alessandro Falaschi, 2009.

[31] "Fast transforms: Algorithms, analyses, applications". In: *Signal Processing* 5.4 (July 1983), p. 387. DOI: 10.1016/0165-1684(83)90098-1. URL: https://doi.org/10.1016%2F0165-1684%2883%2990098-1.

[32] Eugene Finkin. "Surface roughness in wear". In: *Wear* 6.4 (1963), pp. 293–302. ISSN: 0043-1648. DOI: https://doi.org/10.1016/0043-1648(63)90161-3. URL: http://www.sciencedirect.com/science/article/pii/0043164863901613.

[33] M. Frigo and S.G. Johnson. "The Design and Implementation of FFTW3". In: *Proceedings of the IEEE* 93.2 (Feb. 2005), pp. 216–231. DOI: 10.1109/jproc.2004.840301. URL: https://doi.org/10.1109%2Fjproc.2004.840301.

[34] L Frosini, M Magnaghi, and A Albini. "An improved diagnostic system to detect inter-turns short circuits in low voltage stator windings". In: *2015 IEEE Workshop on Electrical Machines Design, Control and Diagnosis (WEMDCD)*. IEEE. 2015, pp. 220–225.

[35] Lucia Frosini, Paolo Pennacchi, and Carlo Maria Stoisser. "Analysis of Unbalanced Magnetic Pull Calculation in Generators With Two Pole Pairs". In: *Volume 1: 22nd Biennial Conference on Mechanical Vibration and Noise, Parts A and B*. ASME, 2009. DOI: 10.1115/detc2009-87194. URL: https://doi.org/10.1115%2Fdetc2009-87194.

[36] Lucia Frosini et al. "A novel approach to detect short circuits in low voltage induction motor by stray flux measurement". In: *2012 XXth International Conference on Electrical Machines*. IEEE, Sept. 2012. DOI: 10.1109/icelmach.2012.6350083. URL: https://doi.org/10.1109%2Ficelmach.2012.6350083.

[37] Jian Fu, Jean-Charles Maré, and Yongling Fu. "Modelling and simulation of flight control electromechanical actuators with special focus on model architecting, multidisciplinary effects and power flows". In: *Chinese Journal of Aeronautics* 30.1 (2017), pp. 47–65. ISSN: 1000-9361. DOI: https://doi.org/10.1016/j.cja.2016.07.006. URL: http://www.sciencedirect.com/science/article/pii/S1000936116301996.

[38] Jian Fu, Jean-Charles Maré, and Yongling Fu. "Modelling and simulation of flight control electromechanical actuators with special focus on model architecting, multidisciplinary effects and power flows". In: *Chinese Journal of Aeronautics* 30.1 (Feb. 2017), pp. 47–65. DOI: 10.1016/j.cja.2016.07.006. URL: https://doi.org/10.1016%2Fj.cja.2016.07.006.

[39] K.R. Fyfe and E.D.S. Munck. "ANALYSIS OF COMPUTED ORDER TRACKING". In: *Mechanical Systems and Signal Processing* 11.2 (Mar. 1997), pp. 187–205. DOI: 10.1006/mssp.1996.0056. URL: https://doi.org/10.1006%2Fmssp.1996.0056.

[40] Muhammad Sani Gaya et al. "Optimal PID Design Approaches for an Inverted Pendulum System". In: *International Review of Automatic Control (IREACO)* 9.3 (May 2016), p. 167. DOI: 10.15866/ireaco.v9i3.9160. URL: https://doi.org/10.15866%2Fireaco.v9i3.9160.

[41] I. Grattan-Guinness. "Joseph Fourier, Théorie analytique de la chaleur (1822)". In: *Landmark Writings in Western Mathematics 1640-1940*. Elsevier, 2005, pp. 354–365. DOI: 10.1016/b978-044450871-3/50107-8. URL: https://doi.org/10.1016%2Fb978-044450871-3%2F50107-8.

[42] I Gunes and A Dalar. "Effect of sliding speed on friction and wear behaviour of borided gear steels". In: *Journal of the Balkan Tribological Association* 19.3 (2013), pp. 325–339.

[43] Qinkai Han, Xinglin Li, and Fulei Chu. "Skidding behavior of cylindrical roller bearings under time-variable load conditions". In: *International Journal of Mechanical Sciences* 135 (Jan. 2018), pp. 203–214. DOI: 10.1016/j.ijmecsci.2017.11.013. URL: https://doi.org/10.1016%2Fj.ijmecsci.2017.11.013.

[44] D Hanselman. "Brushless Permanent Magnet Motor Design 2nd". In: *Magna Physics Pub., Lebanon* (2006).

[45] Michel Haritopoulos et al. "Application of Speed Transform to the diagnosis of a roller bearing in variable speed". In: *Surveillance 7*. 2012.

[46] F.J. Harris. "On the use of windows for harmonic analysis with the discrete Fourier transform". In: *Proceedings of the IEEE* 66.1 (1978), pp. 51–83. DOI: 10.1109/proc.1978.10837. URL: https://doi.org/10.1109%2Fproc.1978.10837.

[47] H. Herlufsen et al. "Characteristics of the Vold-Kalman order tracking filter". In: *2000 IEEE International Conference on Acoustics, Speech, and Signal Processing. Proceedings (Cat. No.00CH37100)*. IEEE. DOI: 10.1109/icassp.2000.860254. URL: https://doi.org/10.1109%2Ficassp.2000.860254.

[48] S.C. Jensen, G.D. Jenney, and D. Dawson. “Flight test experience with an electromechanical actuator on the F-18 Systems Research Aircraft”. In: *19th DASC. 19th Digital Avionics Systems Conference. Proceedings (Cat. No.00CH37126)*. IEEE. DOI: 10.1109/dasc.2000.886914. URL: https://doi.org/10.1109%2Fdasc.2000.886914.

[49] Dean Karnopp. “Computer Simulation of Stick-Slip Friction in Mechanical Dynamic Systems”. In: *Journal of Dynamic Systems, Measurement, and Control* 107.1 (1985), p. 100. DOI: 10.1115/1.3140698. URL: https://doi.org/10.1115%2F1.3140698.

[50] Tobias Kreitz and Frank Thielecke. “Virtual Integration of an All-Electric Flight Control System Architecture and the Aircraft Electrical Power Distribution Network”. In: *SAE Technical Paper Series*. SAE International, Sept. 2016. DOI: 10.42712016-01-2034. URL: httpsdoi.org10.4271%2F2016-01-2034.

[51] BYOUNG-KUK LEE and MEHRDAD EHSANI. “Advanced Simulation Model for Brushless DC Motor Drives”. In: *Electric Power Components and Systems* 31.9 (Sept. 2003), pp. 841–868. DOI: 10.1080/15325000390227191. URL: https://doi.org/10.1080%2F15325000390227191.

[52] Jan Leuridan et al. “High Resolution Order Tracking Using Kalman Tracking Filters - Theory and Applications”. In: *SAE Technical Paper Series*. SAE International, May 1995. DOI: 10.4271/951332. URL: https://doi.org/10.4271%2F951332.

[53] Ian Moir and Allan Seabridge. *Aircraft Systems: Mechanical, Electrical, and Avionics Subsystems Integration, Third Edition*. American Institute of Aeronautics and Astronautics, Inc., June 2008. DOI: 10.2514/4.479526. URL: https://doi.org/10.2514%2F4.479526.

[54] James F. Needham. *Failsafe/Safe-Life Interface Criteria*. Tech. rep. Jan. 1975. DOI: 10.21236/ada006131. URL: https://doi.org/10.21236%2Fada006131.

[55] N.A. Al-Nuaim and H. Toliyat. “A novel method for modeling dynamic air-gap eccentricity in synchronous machines based on modified winding function theory”. In: *IEEE Transactions on Energy Conversion* 13.2 (June 1998), pp. 156–162. DOI: 10.1109/60.678979. URL: https://doi.org/10.1109%2F60.678979.

[56] Alan V Oppenheim and Ronald W Schafer. *Discrete-time signal processing*. Pearson Education, 2014.

[57] Alphonsa Roslin Paul and Mary George. “Brushless DC motor control using digital PWM techniques”. In: *2011 International Conference on Signal Processing, Communication, Computing and Networking Technologies*. IEEE, July 2011. DOI: 10.1109/icsccn.2011.6024647. URL: https://doi.org/10.1109%2Ficsccn.2011.6024647.

[58] Pierre Pellerey, Vincent Lanfranchi, and Guy Friedrich. "Numerical simulations of rotor dynamic eccentricity effects on synchronous machine vibrations for full run up". In: *2012 XXth International Conference on Electrical Machines*. IEEE, Sept. 2012. DOI: 10.1109/icelmach.2012.6350316. URL: https://doi.org/10.1109%2Ficelmach.2012.6350316.

[59] J. Penman et al. "Detection and location of interturn short circuits in the stator windings of operating motors". In: *IEEE Transactions on Energy Conversion* 9.4 (1994), pp. 652–658. DOI: 10.1109/60.368345. URL: https://doi.org/10.1109%2F60.368345.

[60] Paolo Pennacchi. "Computational model for calculating the dynamical behaviour of generators caused by unbalanced magnetic pull and experimental validation". In: *Journal of Sound and Vibration* 312.1-2 (Apr. 2008), pp. 332–353. DOI: 10.1016/j.jsv.2007.10.052. URL: https://doi.org/10.1016%2Fj.jsv.2007.10.052.

[61] Paolo Pennacchi and Lucia Frosini. "Dynamic behaviour of a four-poles turbo generator with rotor eccentricity". In: *12th IFToMM World Congress* (June 2007).

[62] Josip Polak et al. "METHODS FOR INTER-COIL SHORT CIRCUIT DETECTION IN EXCITATION WINDING COILS OF TURBO GENERATOR IN OPERATION AND IN STANDSTILL CONDITION". In: *10. savjetovanje HRO CIGRÉ, Cavtat, 6.–10. studenoga 2011*. 2011.

[63] "Prediction of Remaining Useful Life". In: *Machinery Prognostics and Prognosis Oriented Maintenance Management*. John Wiley & Sons Singapore Pte. Ltd, Dec. 2014, pp. 153–182. DOI: 10.1002/9781118638743.ch5. URL: https://doi.org/10.1002%2F9781118638743.ch5.

[64] *Prognostics: The Science of Making Predictions 1st Edition*. 1th Edition. CreateSpace Independent Publishing Platform, Apr. 2017. ISBN: ISBN-10: 1539074838 ISBN-13: 978-1539074830.

[65] D. Dane Quinn. "A New Regularization of Coulomb Friction". In: *Journal of Vibration and Acoustics* 126.3 (2004), p. 391. DOI: 10.1115/1.1760564. URL: https://doi.org/10.1115%2F1.1760564.

[66] M Recksieck. "Advanced high lift system architecture with distributed electrical flap". In: *Proceedings of the 2nd International Workshop on Aircraft System Technologies*. 2012, pp. 26–27.

[67] "Report of Large Motor Reliability Survey of Industrial and Commercial Installations, Part I". In: *IEEE Transactions on Industry Applications* IA-21.4 (1985), pp. 853–864. DOI: 10.1109/tia.1985.349532. URL: https://doi.org/10.1109%2Ftia.1985.349532.

[68] "Report of Large Motor Reliability Survey of Industrial and Commercial Installations, Part II". In: *IEEE Transactions on Industry Applications* IA-21.4 (1985), pp. 865–872. DOI: 10.1109/tia.1985.349533. URL: https://doi.org/10.1109%2Ftia.1985.349533.

[69] Curtis A. Rideout and Scott J. Ritchie. "Life Remaining Prognostics for Airframe Structural Components". In: *2007 IEEE Aerospace Conference*. IEEE, 2007. DOI: 10.1109/aero.2007.352910. URL: https://doi.org/10.1109%2Faero.2007.352910.

[70] T. Sreenuch et al. "Probabilistic Monte-Carlo Method for Modelling and Prediction of Electronics Component Life". In: *International Journal of Advanced Computer Science and Applications* 5.1 (2014). DOI: 10.14569/ijacsa.2014.050113. URL: https://doi.org/10.14569%2Fijacsa.2014.050113.

[71] A. Stavrou, H.G. Sedding, and J. Penman. "Current monitoring for detecting inter-turn short circuits in induction motors". In: 16.1 (Mar. 2001), pp. 32–37. DOI: 10.1109/60.911400. URL: https://doi.org/10.1109%2F60.911400.

[72] Corey Stephens et al. "Standardizing international taxonomies". In: *ISASI Forum*. Vol. 8. 2008, p. 13.

[73] Greg C. Stone et al. *Electrical Insulation for Rotating Machines*. John Wiley & Sons, Inc., July 2014. DOI: 10.1002/9781118886663. URL: https://doi.org/10.1002%2F9781118886663.

[74] N.P. Suh and P. Sridharan. "Relationship between the coefficient of friction and the wear rate of metals". In: *Wear* 34.3 (1975), pp. 291–299. ISSN: 0043-1648. DOI: https://doi.org/10.1016/0043-1648(75)90097-6. URL: http://www.sciencedirect.com/science/article/pii/0043164875900976.

[75] Nam P. Suh et al. *The Delamination Theory of Wear*. Tech. rep. Sept. 1974. DOI: 10.21236/ada003583. URL: https://doi.org/10.21236%2Fada003583.

[76] Laixue Sun and Sian Shi. "A Hybrid Fault Diagnosis Method of Electromechanical Actuator Combining Model-Based and Data-Driven". In: *CSAA/IET International Conference on Aircraft Utility Systems (AUS 2018)*. Institution of Engineering and Technology, 2018. DOI: 10.1049/cp.2018.0324. URL: https://doi.org/10.1049%2Fcp.2018.0324.

[77] Thamo Sutharssan et al. "Prognostic and health management for engineering systems: a review of the data-driven approach and algorithms". In: *The Journal of Engineering* 2015.7 (July 2015), pp. 215–222. DOI: 10.1049/joe.2014.0303. URL: https://doi.org/10.1049%2Fjoe.2014.0303.

[78] J.I. Taylor. *The Vibration Analysis Handbook: A Practical Guide for Solving Rotating Machinery Problems*. VCI, 2003. ISBN: 9780964051720. URL: https://books.google.it/books?id=V4GxAAAACAAJ.

[79] O.V. Thorsen and M. Dalva. "A survey of faults on induction motors in offshore oil industry, petrochemical industry, gas terminals and oil refineries". In: *Proceedings of IEEE Petroleum and Chemical Industry Technical Conference (PCIC '94)*. IEEE. DOI: 10.1109/pcicon.1994.347637. URL: https://doi.org/10.1109%2Fpcicon.1994.347637.

[80] Ivana Todic, Marko Milos, and Mirko Pavisic. "Position and speed control of electromechanical actuator for aerospace applications". In: *Tehnicki Vjesnik* 20 (Oct. 2013), pp. 853–860.

[81] George Vachtsevanos et al. *Intelligent Fault Diagnosis and Prognosis for Engineering Systems*. John Wiley & Sons, Inc., Sept. 2006. DOI: 10.1002/9780470117842. URL: https://doi.org/10.1002%2F9780470117842.

[82] Håvard Vold and Jan Leuridan. "High Resolution Order Tracking at Extreme Slew Rates, Using Kalman Tracking Filters". In: *SAE Technical Paper Series*. SAE International, May 1993. DOI: 10.4271/931288. URL: https://doi.org/10.4271%2F931288.

[83] J. R. Younkin. "Open Loop Flight Control System". In: *SAE Technical Paper Series*. SAE International, Apr. 1968. DOI: 10.4271/680207. URL: https://doi.org/10.4271%2F680207.

This Ph.D. thesis has been typeset by means of the TeX-system facilities. The typesetting engine was LuaLaTeX. The document class was `toptesi`, by Claudio Beccari, with option `tipotesi=scudo`. This class is available in every up-to-date and complete TeX-system installation.